Probing the Molecular Basis of Photochemistry and Photophysics with Vibrational Coherence Spectroscopy

Christoph Schnedermann

St Hilda's College

University of Oxford

A thesis submitted for the degree of

Doctor of Philosophy in Theoretical and Physical Chemistry

30th September, 2015

Acknowledgements

Over the last couple of years, I was fortunate to be supported by a number of outstanding people, both academically and socially. First and foremost, I would like to thank my family, in particular my mum, for their continuous encouragement, understanding and ability to make me feel 'at home' despite the involved geographical distance. I am also grateful to have friends who, despite the long periods of my absence, never ceased to be true friends regardless the situation. In particular the joint singing sessions as well as the late-evening online-sport activities lead to a well-balanced and enjoyable time.

For the eternal stream of new and crazy ideas and experiments, I would like to express my thanks to my supervisor *Philipp Kukura*, who always created a goal-oriented and yet relaxed working environment with a fantastic group of people. The Kukura group has become part of my life both at and after work. In the femto section, I thoroughly enjoyed working together with my predecessor, *Matz Liebel*, who managed, despite all obstacles, to bring out the experimentalist in me which led to many insightful projects. Amongst the post-docs, I would especially like to thank *Torsten Wende* for joining me in the quest of 2D Raman as well as his general support throughout. Towards the end of my degree I also had the pleasure to be working with *Jong Min Lim* and *Alex Duarte* which led to exciting new projects which I am sure will come to fruitful conclusions. Amongst the iSCAT section, *Joanna Andrecka*, *Jaime Ortega-Arroyo* and *Aleksander Sebasta* deserve special thanks for keeping the group and lab alive even after normal working hours.

Last but not least, I would like to thank *Giovanni Bassolino* for endless supply of retinals, my collaborators (*Akshay Rao*, *Andrew Musser*, *Joachim Heberle*, *Vera Muders*, *Katelyn Spillane*) for their excellent work, my students for many amusing moments and everybody who reads part of this thesis.

Statement of Originality

The research described in this thesis was carried out by the author between October 2012 and September 2015 and includes nothing which is the outcome of work done in collaboration, except where specifically indicated in the text. The use of the first person plural is strictly a matter of style in keeping with standard scientific convention.

List of Publications

The work carried out by the author between October 2012 and September 2015 led to the following publications:

1. T. Sovdat, G. Bassolino, M. Liebel, **C. Schnedermann**, S. P. Fletcher and P. Kukura, *J. Am. Chem. Soc.*, 2012, **134**, 8318-20.

2. G. Bassolino, T. Sovdat, M. Liebel, **C. Schnedermann**, B. Odell, T. D. W. Claridge, P. Kukura and S. P. Fletcher, *J. Am. Chem. Soc.*, 2014, **136**, 2650-8.

3. M. Liebel, **C. Schnedermann** and P. Kukura, *Phys. Rev. Lett.*, 2014, **112**, 198302.

4. M. Liebel, **C. Schnedermann**, G. Bassolino, G. Taylor, A. Watts and P. Kukura, *Phys. Rev. Lett.*, 2014, **112**, 238301.

5. M. Liebel, **C. Schnedermann** and P. Kukura, *Opt. Lett.*, 2014, **39**, 4112-5.

6. T. Wende, M. Liebel, **C. Schnedermann**, R. J. Pethick and P. Kukura, *J. Phys. Chem. A*, 2014, **118**, 9976-84.

7. **C. Schnedermann**, M. Liebel and P. Kukura, *J. Am. Chem. Soc.*, 2015, **137**, 2886-91.

8. A. J. Musser, M. Liebel, **C. Schnedermann**, T. Wende, T.B. Kehoe, A. Rao and P.Kukura, *Nat. Phys.*, 2015, **11**, 3527.

9. M. Liebel, **C. Schnedermann**, T. Wende and P. Kukura, *J. Phys. Chem. A*, 2015, **119**, 9506-17.

10. G. Bassolino, T. Sovdat, A. S. Duarte, J. M. Lim, **C. Schnedermann**, M. Liebel, B. Odell, T. D. W. Claridge, S. P. Fletcher and P. Kukura, *J. Am. Chem. Soc.*, 2015, **137**, 12434-7.

Abstract

We present a time-domain impulsive vibrational spectroscopy (IVS) setup capable of recording background- and baseline-free Raman spectra of excited electronic states in condensed-phase molecular systems. The setup records vibrational Raman spectra from 50-3000 cm^{-1} and is readily extended to follow spectral evolutions with a time resolution of <20 fs, opening up the possibility for multi-dimensional Raman spectroscopy. Based on the setup, we explore a wide range of photochemical reactions aimed at gaining fundamental insights in the chemistry of excited electronic states.

In rhodopsin, we investigate the consequences of vibrational wavepacket motion through a conical intersection. We identify the C_{11}-H hydrogen out-of-plane mode as a coupling mode and devise a general model of how vibrational coherences can be used to obtain otherwise inaccessible structural information. In a second experiment, we determine the photoproduct distribution and dynamics upon isotopic substitution of selected hydrogen atoms along the retinal backbone. The results suggest a re-definition of the traditional Jablonski diagram for ultrafast photoreactions, which proceed faster than vibrational relaxation.

In channelrhodopsin-1, we structurally characterise the primary photoproduct in the photocycle to be of 13-*cis* character. The study highlights the capabilities of IVS to obtain structural information for short-lived intermediate structures which are otherwise challenging to obtain.

For the green fluorescent protein and all-*trans* retinal protonated Schiff base, we identify key excited-state (intermediate) structures and complement the studies with multi-dimensional Raman spectroscopy. The results provide a first picture of the structural origin of energy flow directly after photoexcitation.

This thesis emphasises the capabilities of IVS beyond a proof-of-principle experiment and outlines the high potential of time-domain vibrational spectroscopy to reveal detailed structural information on ultrafast processes with high temporal resolution and sensitivity.

Contents

List of Figures

List of Abbreviations

AOI	Angle of incidence
APP	Actinic-pump-probe
BBO	β-barium-borate
BK7	Borosilicate glass
BP	Band-pass
bR	Bacteriorhodopsin
BS	Beamsplitter
CA	Coherent artefact
CARS	Coherent anti-Stokes Raman spectroscopy
$CHCl_3$	Chloroform
ChR1/2	Channelrhodopsin-1/2
CI	Conical intersection
DC	Direct current
DFG	Difference-frequency generation
DPO	Diphenyl-octatetraene
DTT	Differential normalised transmittance
EMG	Exponentially-modified Gaussian
ESA	Excited-state absorption
ESPT	Excited-state proton transfer
FC	Franck-Condon
FFT	Fast Fourier transform
FROG	Frequency-resolved optical gating
FS	Fused silica
FSRS	Femtosecond stimulated Raman spectroscopy
FT-IR	Fourier transform infrared
FWHM	Full-width-half-maximum
GSB	Ground-state bleach
GT	Glenn-Taylor

GVD	Group-velocity dispersion
HOOP	Hydrogen out-of-plane
HS	Harmonic separator
IR	Infrared
ISRS	Impulsive stimulated Raman scattering
IVS	Impulsive vibrational spectroscopy
LP	Long-pass
MeOH	Methanol
nBu-RPSB	n-butyl retinal protonated Schiff base
ND	Neutral-density
NOPA	Non-collinear optical parametric amplifier
OD	Optical density
OR	Optical rectification
PC-IVS	Population-controlled IVS
PDP	Pump-dump-probe
PIA	Photoinduced absorption
QY	Quantum yield
RPSB	Retinal protonated Schiff base
RR	Resonance Raman
RWA	Rotating-wave approximation
SE	Stimulated emission
SFG	Sum-frequency generation
SHG	Second-harmonic generation
SNR	Signal-to-noise ratio
SWFT	Sliding-window Fourier transform
TA	Transient absorption
THG	Third-harmonic generation
TL	Transform limit
TOD	Third-order dispersion
TR^3	Time-resolved resonance Raman
TRIR	Time-resolved infrared
UV	Ultraviolet
VC	Vibrational coherence
VIS	Visible
VR	Vibrational relaxation
WL	Whitelight

WMEL	Wave-mixing energy ladder
wt-GFP	Wild-type green fluorescent protein
Yb:KGW	Potassium gadolinium tungstate doped with ytterbium ions
*Ca*ChR	Channelrhodopsin derived from *chlamydomonas augustae*
*Cr*ChR	Channelrhodopsin derived from *chlamydomonas reinhardtii*

Chapter 1

Introduction

The interaction of light with matter is at the core of some of the most important reactions occurring in everyday life. Amongst the most important are light harvesting and photosynthesis,[1–6] the process of vision[7–12] and more recently optogenetic[13,14] and nanoplasmonic applications.[15–17] In particular biologically relevant processes operate in a rather complex sequence of steps. For example, the process of dim light vision in the human eye starts by illumination of the retina, composed of millions of rod cells which each contain numerous photoreceptive pigments, called rhodopsin.[18] Embedded in rhodopsin is the chromophore 11-*cis* retinal, which absorbs the incident light and undergoes a structural change to all-*trans* retinal.[7] This in turn triggers a larger conformational change of rhodopsin causing a cascade of biochemical steps which are coupled to synaptic excitation.[18] Despite its complexity, the fundamental primary step in vision involves the absorption of a photon by the molecular chromophore 11-*cis* retinal. To understand such processes, it is imperative to be able to observe the corresponding molecular changes in real time after exposing the molecules to light, ideally by 'recording a molecular movie'.[19–23] The size dimensions of typical molecules of interest, however, rarely exceed a couple of nanometers while the time scale of molecular changes is on the order of tens to hundreds of femtoseconds, preventing the use of conventional imaging techniques.[24–26] Instead, indirect highly time-resolved spectroscopic methods with pulsed laser sources have to be employed to deduce the structural properties of the molecules in action.

The most widely used techniques to date involve measuring transient electronic absorption spectra as a function of time after photoexcitation by a short pulse.[10,27,28] The dynamic processes involving multiple excited electronic states can be resolved with typical effective time resolutions of $\sim$20 fs, greatly aiding

the understanding of photochemical reactions. In addition, multi-dimensional implementations to investigate the coupling between electronic states have recently emerged.[29–31]

A structurally sensitive analogue to transient absorption (TA) spectroscopy forms transient time-resolved infrared (TRIR) spectroscopy.[32–34] Here, a short pulse excites the system and an IR absorption spectrum is recorded as a function of time. The technique provides mode-specific dynamics with temporal resolutions typically down to ∼100 fs and requires IR-allowed transitions making it insensitive to the low-frequency vibrational spectrum (<500 cm^{-1}). Recently, TRIR spectroscopy has been further developed into multi-dimensional techniques (2D- and 3D-IR) with sub-picosecond time-resolution, which provide an enormous amount of information about the chemical dynamics of a system by resolving vibrational mode couplings and anharmonicities.[35–39]

Spectral information in the low-frequency region, or more generally beyond IR accessible modes over the full vibrational manifold (50-3500 cm^{-1}) can be obtained using Raman spectroscopy, which is based on detecting frequency-shifted photons scattered by the sample after irradiation. The corresponding cross sections are, however, much smaller compared to IR or TA spectroscopy, making it necessary to employ stimulated or resonantly enhanced conditions.[40] Typical excited-state Raman spectroscopy implementations like time-resolved resonance Raman (TR^3),[40,41] coherent anti-Stokes Raman (CARS)[42,43] or more recently femtosecond stimulated Raman (FSRS)[44–46] detect the signal in the frequency-domain and achieve time resolutions in the signal generating step down to ∼20 fs. Similar information can, in theory, be achieved with time-domain techniques like impulsive stimulated Raman scattering (ISRS) or impulsive vibrational spectroscopy (IVS), in which the full vibrational response of the system induced by a short pump pulse is recorded in real time.[47,48] The spectral information is then obtained after Fourier transformation of the time-domain signal. Despite numerous advantages, technical difficulties mainly associated with the generation of sufficiently short pulses and sensitivity levels have frequently limited the use of IVS for complex molecular systems in the condensed phase.[49,50]

In this work, we demonstrate the key principles in designing an ultrafast IVS setup capable of producing time-resolved excited-state Raman spectra over the full vibrational manifold (50-3000 cm^{-1}). In addition, we present for the

first time a two-dimensional extension of excited-state Raman spectroscopy based on IVS. The work is outlined as follows:

In *chapter 2*, we briefly discuss the fundamentals of linear and nonlinear optics required for different pulse generation schemes forming the basis of the experimental implementations. In addition, we provide a short overview of the theoretical description of linear and nonlinear spectroscopy in the form of the density matrix formalism to account for different signals encountered in the experimental data.

Chapter 3 elaborates on the experimental realisation of a highly time-resolved (<10 fs) and sensitive ($\sim\mu$OD) IVS setup. To this end we explain in detail the pulse generation schemes and highlight important design aspects. The second part of the chapter describes the experimental techniques employed in this work and illustrates the basic concepts with a suitable example.

In *chapter 4* we apply IVS to the primary step in vision, the 11-*cis* to all-*trans* photoisomerisation in the protein rhodopsin. By using resonant and off-resonant IVS, we characterise the behaviour of different vibrational modes during the isomerisation reaction and reveal for the first time experimentally the identity of a coupling mode of a conical intersection.

We continue to explore rhodopsin in *chapter 5* by isotopically labelling specific hydrogen sites around the isomerising 11-*cis* bond. Combining high time-resolution TA spectroscopy with independent quantum yield measurements shows that ultrafast reactions shorter than the vibrational relaxation time are phase-space dependent.

Chapter 6 studies the photodynamics of channelrhodopsin-1, a protein frequently used in optogenetic applications. We provide an extended TA map from 500-900 nm and characterise the coherence transfer to the first intermediate in the photocycle. The results are complemented by low-temperature resonance Raman spectroscopy and IVS, providing the first structural evidence for a sub-picosecond photoisomerisation from all-*trans* to 13-*cis* retinal.

In *chapter 7*, we investigate the ultrafast dynamics of the green fluorescent protein, wt-GFP. We provide time-resolved IVS Raman spectra illustrating the appearance of the fluorescent state and structurally characterise the initial and fluorescent states. In addition, we show for the first time highly time-resolved Raman spectra (<20 fs) over the first picosecond and derive a 2D excited-state Raman map. A preliminary discussion of 2D Raman is presented and potential implications for the system are discussed.

Chapter 8 investigates all-*trans* retinal protonated Schiff base in methanol solution. We fully characterise the excited-state dynamics over the full excited-state lifetime using IVS, including a brief discussion of the corresponding 2D excited-state Raman map. Mechanistic effects are discussed and their implications for the chromophore in bacteriorhodopsin are highlighted.

The final *chapter 9* provides a short summary over the contents of this thesis and concludes with an outlook.

Chapter 2

Theoretical Background

At this point we introduce the basic concepts of nonlinear optics and nonlinear spectroscopy. This chapter is intended as a very brief summary of the most important equations and their origins but does not aim to be complete. For a more detailed description on nonlinear optics we refer to the books by Weiner,[51] Boyd[52] and Rullière,[53] while the topic of nonlinear spectroscopy is covered in depth by Mukamel[54] and Hamm.[35,55]

2.1 Nonlinear Optics

2.1.1 Pulsed Electric Fields

Light can be described according to Maxwell's equations as an oscillating electric field at frequency ω_0

$$E(t) = \Re\left(E_0 \mathrm{e}^{i(\omega_0 t)}\right). \tag{2.1}$$

In the limit of pulsed electromagnetic radiation this equation becomes

$$E(t) = \Re\left(E_0 \mathrm{e}^{-\Gamma t^2} \mathrm{e}^{i(\omega_0 t)}\right) \tag{2.2}$$

$$= \Re\left(E_0(t) \mathrm{e}^{i(\omega_0 t)}\right), \tag{2.3}$$

with the pulse-width parameter Γ. For a Gaussian pulse, the corresponding spectrum is obtained by Fourier transformation

$$E(\omega) \propto \mathrm{e}^{\frac{-(\omega-\omega_0)^2}{4\Gamma}}. \tag{2.4}$$

Pulses that can be represented by equation 2.3 are called transform-limited (TL) since all frequency components are in-phase. We account for possible

deviations in this behaviour by adding an additional temporal phase parameter, $\phi(t)$. The pulse in the time domain is then described as

$$E(t) = \Re\left(E_0(t)\mathrm{e}^{i(\omega_0 t+\phi(t))}\right), \tag{2.5}$$

with a corresponding spectrum in the frequency domain given as

$$E(\omega) \propto \mathrm{e}^{\frac{-(\omega-\omega_0)^2}{4\Gamma}}\mathrm{e}^{i\phi(\omega-\omega_0)}. \tag{2.6}$$

A pulse travelling in a medium will accumulate a frequency-dependent phase term since different frequencies of the pulse travel at different velocities

$$v(\omega) = \frac{c}{n(\omega)}, \tag{2.7}$$

with the refractive index n. The spectral phase $\phi(\omega)$ is in this case commonly written as a Taylor expansion around ω_0

$$\begin{aligned}\phi(\omega) = \phi(\omega_0) + (\omega-\omega_0)\left(\frac{\partial\phi}{\partial\omega}\right)_{\omega=\omega_0} + \frac{1}{2}(\omega-\omega_0)^2\left(\frac{\partial^2\phi}{\partial\omega^2}\right)_{\omega=\omega_0} \\ + \frac{1}{6}(\omega-\omega_0)^3\left(\frac{\partial^3\phi}{\partial\omega^3}\right)_{\omega=\omega_0} + \cdots \qquad (2.8)\\ = \phi_0 + (\omega-\omega_0)\phi_1 + \frac{1}{2}(\omega-\omega_0)^2\phi_2 + \frac{1}{6}(\omega-\omega_0)^3\phi_3 + \cdots . \qquad (2.9)\end{aligned}$$

To understand the physical implications of the terms, it is useful to re-write the phase as

$$\phi(\omega) = -\beta(\omega)L, \tag{2.10}$$

where $\beta(\omega) = \frac{\omega n(\omega)}{c}$ is the propagation constant in the medium of length L. We can express the propagation constant also in terms of a Taylor expansion

$$\begin{aligned}\beta(\omega) = \beta(\omega_0) + (\omega-\omega_0)\left(\frac{\partial\beta}{\partial\omega}\right)_{\omega=\omega_0} + \frac{1}{2}(\omega-\omega_0)^2\left(\frac{\partial^2\beta}{\partial\omega^2}\right)_{\omega=\omega_0} \\ + \frac{1}{6}(\omega-\omega_0)^3\left(\frac{\partial^3\beta}{\partial\omega^3}\right)_{\omega=\omega_0} + \cdots \qquad (2.11)\\ = \beta_0 + (\omega-\omega_0)\beta_1 + \frac{1}{2}(\omega-\omega_0)^2\beta_2 + \frac{1}{6}(\omega-\omega_0)^3\beta_3 + \cdots . \qquad (2.12)\end{aligned}$$

The pulse after the medium can then be expressed as

$$E_{\mathrm{out}}(t) = \Re\left(\mathrm{e}^{i(\omega_0 t-\beta_0 L)}A_{\mathrm{out}}(t)\right). \tag{2.13}$$

with the output amplitude, A, given by an inverse Fourier transformation as

$$A_{\text{out}}(t) = \frac{1}{2\pi}\int d\tilde{\omega} A(\tilde{\omega}) \mathrm{e}^{i[\tilde{\omega}t - L(\beta_1\tilde{\omega} + \frac{\beta_2}{2}\tilde{\omega}^2 + \frac{\beta_3}{6}\tilde{\omega}^3 + \cdots)]}, \tag{2.14}$$

where we set $\tilde{\omega} = (\omega - \omega_0)$. The electric field is a product of a main carrier term dependent on β_0 and a pulse-envelope function $A_{\text{out}}(t)$. The amplitude is thus not affected by a constant phase offset, ϕ_0.

Adding a linear phase of the form $\beta = \beta_0 + \beta_1\tilde{\omega}$ yields

$$A_{\text{out}}(t) = \frac{1}{2\pi}\int d\tilde{\omega} A(\tilde{\omega}) \mathrm{e}^{i\tilde{\omega}(t - L\beta_1)} \tag{2.15}$$

$$= A_{\text{in}}(t - \beta_1 L). \tag{2.16}$$

The second term in equation 2.9 therefore also does not affect the shape of the pulse but leads instead to an overall delay of the pulse at the so-called group-velocity, v_g, defined as

$$v_g = \beta_1^{-1} = \left(\frac{\partial\beta}{\partial\omega}\right)^{-1}_{\omega=\omega_0}. \tag{2.17}$$

The third and fourth terms in equation 2.9, on the other hand, affect the temporal shape of the pulse and are referred to as group-velocity dispersion (GVD) and third-order dispersion (TOD). GVD arises from a quadratic spectral phase leading to a linear variation in time as a function of frequency, while TOD leads to a quadratic variation in time with frequency. Together with the refractive index variation of the spectral phase given as

$$\phi(\omega) = -\beta(\omega)L = -\frac{\omega n(\omega) L}{c}, \tag{2.18}$$

where c denotes the speed of light, it can be shown that GVD and TOD can be expressed as

$$\phi_2(\omega) = -\beta_2 L = -\frac{L}{c}\left[2\frac{dn}{d\omega} + \omega\frac{d^2n}{d\omega^2}\right] \tag{2.19}$$

$$\phi_3(\omega) = -\beta_3 L = -\frac{L}{c}\left[3\frac{d^2n}{d\omega^2} + \omega\frac{d^3n}{d\omega^3}\right], \tag{2.20}$$

It is essential to be aware of and appropriately compensate for such phase effects at least up to third order to obtain <10 fs, near-TL pulses.

We note that the propagation constant, β, intrinsically accounts for the spatial directionality of the electric field. In this context, it is often also referred

to as wave vector, $\mathbf{k}$. Within this convention, a pulse travelling along the vector $\mathbf{r}$ is expressed as

$$E(t) = \Re\left(E_0(t)\mathrm{e}^{i(\omega_0 t - \mathbf{kr}}\right). \tag{2.21}$$

The wave vector is related to the momentum vector, $\mathbf{p}$, via de Broglie's relation $\mathbf{p} = \hbar\mathbf{k}$. In nonlinear processes involving more than one electric field interaction, the wave vector thus ensures momentum conservation and defines the direction of the generated (nonlinear) signal.

2.1.2 Nonlinear Effects in a Medium

Macroscopic Polarisation

After introducing the theoretical description of a pulse, we now turn to interactions of pulses with a medium giving rise to nonlinear signals. If an electric field interacts with a medium, it will induce a macroscopic polarisation, $P(t)$, given as

$$P(t) = \epsilon_0 \chi^{(1)} E(t), \tag{2.22}$$

where ϵ_0 is the vacuum permittivity and $\chi^{(1)}$ the linear susceptibility of the medium. For pulsed electric fields, the incident field strengths can become so high that the polarisation has to be expanded as a power series to accommodate nonlinear effects

$$\begin{aligned} P(t) &= \epsilon_0(\chi^{(1)}E(t) + \chi^{(2)}E(t)E(t) + \chi^{(3)}E(t)E(t)E(t) + \cdots) && (2.23)\\ &= \epsilon_0 \sum_n \chi^{(n)} E^n(t) && (2.24)\\ &= \sum_n P^{(n)}(t), && (2.25) \end{aligned}$$

with the n^{th}-order susceptibility $\chi^{(n)}$.

Second-Order Nonlinear Effects

Second-order nonlinear effects are, by symmetry, only observed in non-centrosymmetric media. Possible pathways can be obtained by expressing the interaction of two pulsed electric fields of frequency ω_0 and ω_1 in a medium as the

second-order polarisation

$$P^{(2)}(t) = \epsilon_0\chi^{(2)}\left(E_0 e^{i(\omega_0 t - \mathbf{k_0 r_0})} + E_1 e^{i(\omega_1 t - \mathbf{k_1 r_1})}\right)^2 \tag{2.26}$$

$$\begin{aligned} &= \epsilon_0\chi^{(2)}\left(E_0^2 e^{i(2\omega_0 t - 2k_0 r)} + E_1^2 e^{i(2\omega_1 t - 2k_1 r)}\right) \\ &+ \epsilon_0\chi^{(2)}\left(2E_0 E_1 e^{i((\omega_0+\omega_1)t - (k_0+k_1)r)}\right) \\ &+ \epsilon_0\chi^{(2)}\left(2E_0 E_1^* e^{i((\omega_0-\omega_1)t - (k_0-k_1)r)}\right) \\ &+ \epsilon_0\chi^{(2)}\left(E_0 E_0^* + E_1 E_1^*\right), \end{aligned} \tag{2.27}$$

where we have restricted ourselves to TL pulses with $\phi = 0$ and a collinear arrangement such that $\mathbf{r_0} = \mathbf{r_1} = r$ and $\mathbf{k_i} = k_i$, for clarity.

The last term in equation 2.27 is the only frequency-independent contribution and refers to optical rectification (OR) generating a direct current (DC) polarisation in the sample.[56] Among the remaining three frequency-dependent contributions (Figure 2.1), the first term occurs at twice the initial frequency ($2\omega_0$ and $2\omega_1$), corresponding to second-harmonic generation (SHG) of the individual electric fields.[57,58] The wave vector of the second harmonic yields $k_0 + k_0 = 2k_0 = k_s$, requiring two photons from the fundamental to be destroyed to generate one second-harmonic photon (Figure 2.1, left). The second term corresponds to a signal at the sum of the initial frequencies ($\omega_0 + \omega_1$), termed sum-frequency generation (SFG).[59] The SFG wave vector states $k_0 + k_1 = k_s$, requiring the destruction of one photon from each pulse (Figure 2.1, middle). The third term describes a signal at the difference of the fundamental frequencies ($\omega_0 - \omega_1$), referred to as difference-frequency generation (DFG). The wave vector of $k_0 - k_1 = k_s$ requires the destruction of the higher frequency photon (ω_0) and the generation of the lower frequency photon (ω_1) to generate the signal (Figure 2.1, right). The lower frequency field is said to be parametrically amplified, a concept which is extensively employed in the design of non-collinear optical parametric amplifiers (NOPA).[60]

Efficient signal conversion is only possible, if the generated signals at every point within the medium are in-phase, leading to constructive interference (Figure 2.2). This property is referred to as phase-matching. The correct phase-matching settings distinguish between competing signal pathways, depend on the medium used to generate the signal, and are frequency dependent.

To illustrate the above concepts, we will focus on the process of SHG. An

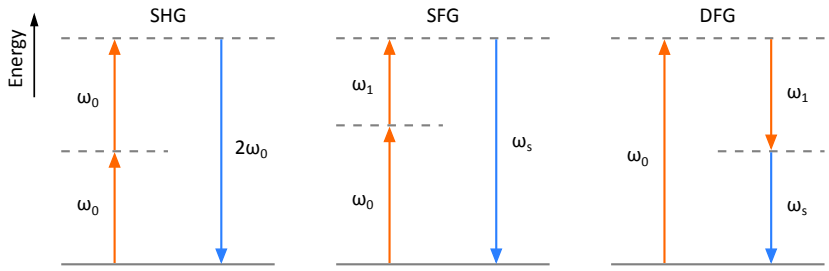

Figure 2.1: Overview of frequency-dependent second-order nonlinear effects. Left: Second-harmonic generation (SHG), Centre: Sum-frequency generation (SFG), Right: Difference-frequency generation (DFG). Vertical arrows denote electric field interactions at their respective frequencies (ω). Orange - incident field, blue - signal field.

evaluation of the wave vector mismatch, Δk, for SHG

$$\Delta k = 2k_0 - k_s \tag{2.28}$$

$$= \frac{2\omega n(\omega)}{c} - \frac{2\omega n(2\omega)}{c}, \tag{2.29}$$

can never reach zero for typical isotropic media which have one refractive index, since the refractive index is a monotonically increasing function with frequency, rendering the result of equation 2.29 always negative. Instead, birefringent crystals, like β-barium-borate (BBO), which possess two distinct crystal axis with different refractive indices need to be employed for efficient SHG and other nonlinear effects. Phase-matching is achieved by selecting an appropriate crystal angle resulting in identical velocities within the medium for input and signal fields. Depending on the polarisation of the two electric fields one distinguishes type I phase-matching requiring two photons of the same polarisation to generate one photon of opposite polarisation from type II phase-matching, where the initial photons are orthogonally polarised. In case of collinear SHG, a type I phase-matched crystal is therefore required.

It can be shown that the SHG intensity depends on the wave vector mismatch according to

$$I_{\mathrm{SHG}} \propto \left(\frac{\sin(\Delta k L/2)}{\Delta k L/2} \right)^2. \tag{2.30}$$

SHG for broadband pulses hence requires a negligible wave vector mismatch and a thin medium to accommodate the full bandwidth (acceptance bandwidth). For example, to frequency-double the full bandwidth of <15 fs pulses a crystal thickness of $\leq$25 μm should be chosen.

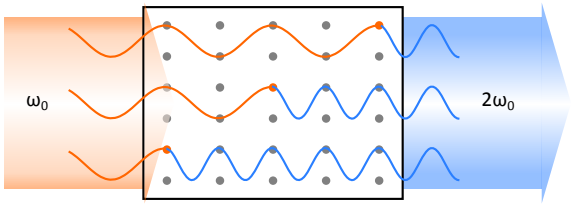

Figure 2.2: Principle of phase-matching in SHG. An incident electric field drives a polarisation in each atom (lattice point) within the crystal, leading to emission of a signal field at twice the frequency. If the medium is birefringent, both fields can travel at the same velocity leading to constructive interference between the signal fields and thus efficient conversion.

Third-Order Effects

Third-order polarisations defined as

$$P^{(3)}(t) = \chi^{(3)} E^3(t), \tag{2.31}$$

occur in a wide range of materials and require three interactions of the medium with the incident electric field. As a consequence, 44 possible signals can emerge at various frequencies depending on the corresponding input fields. To simplify this expression, we assume a monochromatic electric field given as

$$E(t) = E_0 \cos(\omega t), \tag{2.32}$$

which gives rise to a third-order polarisation of the form

$$P^{(3)}(t) = \frac{1}{4}\epsilon_0 \chi^{(3)} \left(E_0^3 \cos(3\omega t) + 3E_0^3 \cos(\omega t) \right). \tag{2.33}$$

The first term in this equation represents a polarisation at thrice the fundamental frequency called third-harmonic generation (THG), while the second term represents an intensity dependent refractive index. The latter can be derived expressing the total macroscopic polarisation as

$$P(t) = \epsilon_0 \chi^{(1)} E_0 \cos(\omega t) + \frac{3}{4}\epsilon_0 \chi^{(3)} E_0^3 \cos(\omega t) \tag{2.34}$$

$$= \epsilon_0 E_0 \cos(\omega t) \left(\chi^{(1)} + \frac{3}{4}\chi^{(3)} E_0^2 \right) \tag{2.35}$$

$$= \epsilon_0 E_0 \cos(\omega t) \chi, \tag{2.36}$$

and combining the expression with the susceptibility dependence of the refrac-

tive index

$$n = (1+\chi)^{\frac{1}{2}} \tag{2.37}$$

$$= \left(1 + \chi^{(1)} + \frac{3}{4}\chi^{(3)}E_0^2\right)^{\frac{1}{2}} \tag{2.38}$$

$$= n_0 \left(1 + \frac{3I}{4n_0^2}\chi^{(3)}\right)^{\frac{1}{2}} \tag{2.39}$$

$$\approx n_0 \left(1 + \frac{1}{2}\frac{3I}{4n_0^2}\chi^{(3)}\right) \tag{2.40}$$

$$= n_0 + n_2 I, \tag{2.41}$$

where we used $n_0 << \chi^{(3)}$ and $I = E_0^2$. A non-centrosymmetric medium can therefore act as a lens (optical Kerr effect) under the influence of an intense electric field leading to self-focussing of the input beam, an important first step for continuum generation. Equation 2.41 also gives rise to self-phase modulation

$$\omega(t) = \frac{\partial}{\partial t}(\omega_0 t - kr) \tag{2.42}$$

$$= \omega_0 - \frac{\omega_0 r}{c}\frac{\partial n(t)}{\partial t}, \tag{2.43}$$

providing new frequencies at

$$\delta\omega = \omega(t) - \omega_0 = -\frac{\omega_0 n_2 r}{c}\frac{\partial I(t)}{\partial t}. \tag{2.44}$$

In addition, another effect called self-steepening can also be traced back to equation 2.41. The propagation of a pulse through a medium leads to a distorted intensity profile as a consequence of the intensity-dependent velocity of the pulse ($v \propto n \propto I$). This results in a steep concentration gradient at one end of the temporal profile and is believed to lead together with self-phase modulation to the generation of very broad continua.[61–63]

2.2 Nonlinear Spectroscopy

Nonlinear spectroscopy aims to understand the interaction of electric fields with a system. This is quantified by the nonlinear response function, $R(t)$, which contains all information of the temporal evolution of the system under the action of an electric field. So far, we only considered crystalline systems without resonant electric field transitions. In the following section, we introduce the density matrix formalism to understand the ensemble properties arising in the condensed phase. Subsequently, we discuss linear spectroscopy and higher-order techniques used in this work.

2.2.1 Density Matrix Formalism

General Definitions

We define the density operator, ρ, of a pure quantum state described by the wavefunction, $|\psi\rangle$, according to

$$\rho \equiv |\psi\rangle \langle\psi| \,. \tag{2.45}$$

The time evolution of the density operator can be derived from the time-dependent Schrödinger equation (TDSE)

$$\frac{d}{dt} |\psi\rangle = -\frac{i}{\hbar} H |\psi\rangle \,, \tag{2.46}$$

and is given by the Liouville von Neumann equation as

$$\frac{d}{dt}\rho = -\frac{i}{\hbar} [H, \rho] \,, \tag{2.47}$$

where $[H, \rho]$ indicates the commutator of the Hamiltonian and the density operator. It is important to note that equation 2.47 contains the same information as the TDSE for a pure quantum state. However, the density operator is a more general treatment allowing for the description of a statistical average, i.e. an ensemble, which is commonly investigated in spectroscopy. In this case, the density operator is modified to

$$\rho = \sum_i P_i |\psi_i\rangle \langle\psi_i| \,, \tag{2.48}$$

with P_i being the probability of finding a system in a pure quantum state i.

An additional generalisation is often made by recasting the time dependence of the density operator in the Liouville representation:

$$\frac{d}{dt}\rho = -\frac{i}{\hbar}L\rho. \tag{2.49}$$

The operator L (also called superoperator) is an n^2-dimensional matrix for an n-dimensional system connecting each element of ρ with every other element. The representation generally allows for a much more compact description compared to the Liouville von Neumann equation.

Two-Dimensional System in the Density Matrix Formalism

To illustrate the introduced notation, we consider a two-level system in the eigenstate basis of the Hamiltonian

$$H = \begin{pmatrix} \epsilon_1 & 0 \\ 0 & \epsilon_2 \end{pmatrix}. \tag{2.50}$$

The time dependence of the density matrix is written as

$$\frac{d}{dt}\rho = -\frac{i}{\hbar}\left[H, \rho\right] \tag{2.51}$$

$$\frac{d}{dt}\begin{pmatrix} \rho_{11} & \rho_{12} \\ \rho_{21} & \rho_{22} \end{pmatrix} = -\frac{i}{\hbar}\begin{pmatrix} 0 & (\epsilon_1 - \epsilon_2)\rho_{12} \\ (\epsilon_2 - \epsilon_1)\rho_{21} & 0 \end{pmatrix}, \tag{2.52}$$

which leads to the solutions for the diagonal terms

$$\begin{aligned} \frac{d}{dt}\rho_{11} = 0 \quad &\rightarrow \quad \rho_{11}(t) = \rho_{11}(0) \\ \frac{d}{dt}\rho_{22} = 0 \quad &\rightarrow \quad \rho_{22}(t) = \rho_{22}(0), \end{aligned} \tag{2.53}$$

and for the off-diagonal terms

$$\begin{aligned} \frac{d}{dt}\rho_{12} = -i\frac{\epsilon_1 - \epsilon_2}{\hbar}\rho_{12} \quad &\rightarrow \quad \rho_{12}(t) = \rho_{12}(0)\mathrm{e}^{-i\frac{\epsilon_1 - \epsilon_2}{\hbar}t} \\ \frac{d}{dt}\rho_{21} = -i\frac{\epsilon_2 - \epsilon_1}{\hbar}\rho_{21} \quad &\rightarrow \quad \rho_{21}(t) = \rho_{21}(0)\mathrm{e}^{-i\frac{\epsilon_2 - \epsilon_1}{\hbar}t}, \end{aligned} \tag{2.54}$$

showing that the off-diagonal elements are oscillating at a difference frequency of the energy levels. The problem can be re-written in the Liouville representation as

$$\frac{d}{dt}\rho = -\frac{i}{\hbar}L\rho \tag{2.55}$$

$$\frac{d}{dt}\begin{pmatrix} \rho_{12} \\ \rho_{21} \\ \rho_{11} \\ \rho_{22} \end{pmatrix} = -\frac{i}{\hbar}\begin{pmatrix} \epsilon_1 - \epsilon_2 & & & \\ & \epsilon_2 - \epsilon_1 & & \\ & & 0 & \\ & & & 0 \end{pmatrix}\begin{pmatrix} \rho_{12} \\ \rho_{21} \\ \rho_{11} \\ \rho_{22} \end{pmatrix}. \tag{2.56}$$

Time-Evolution Operator

To propagate a system which is described by the wavefunction $|\psi\rangle$ and a time-independent Hamiltonian from $t_0 \to t$, we introduce the time-evolution operator, $U(t, t_0)$, such that

$$|\psi(t)\rangle \equiv U(t, t_0) \, |\psi(t_0)\rangle \, . \tag{2.57}$$

The TDSE is then modified to give

$$\frac{d}{dt} U(t, t_0) = -\frac{i}{\hbar} H U(t, t_0) \tag{2.58}$$

$$U(t, t_0) = \mathrm{e}^{-\frac{i}{\hbar} H (t - t_0)}. \tag{2.59}$$

If we now introduce a time-dependent perturbation to the Hamiltonian in the form of an applied electric field, we can express the Hamiltonian as

$$H(t) = H_0 + H'(t). \tag{2.60}$$

The time-evolution operator of the unperturbed system (H_0) is then given as

$$U_0(t, t_0) = \mathrm{e}^{-\frac{i}{\hbar} H_0 (t - t_0)}, \tag{2.61}$$

and we define a wavefunction in the interaction picture (subscript I) as

$$|\psi(t)\rangle \equiv U(t, t_0) \, |\psi_I(t)\rangle \, . \tag{2.62}$$

In this formalism, $|\psi_I(t)\rangle$ describes the time evolution due to the perturbation $H'(t)$ only, and $U(t, t_0)$ provides the time evolution with respect to H_0. Inserting equation 2.62 into the TDSE then yields

$$-\frac{i}{\hbar} H \, |\psi(t)\rangle = \frac{d}{dt} \, |\psi(t)\rangle \tag{2.63}$$

$$-\frac{i}{\hbar} H(t) U_0(t, t_0) \, |\psi_I(t)\rangle = \frac{d}{dt} U_0(t, t_0) \, |\psi_I(t)\rangle \tag{2.64}$$

$$= -\frac{i}{\hbar} H_0 U_0(t, t_0) \, |\psi_I(t)\rangle + U_0(t, t_0) \left(\frac{d}{dt} \, |\psi_I(t)\rangle \right), \tag{2.65}$$

which can be simplified using equation 2.60

$$-\frac{i}{\hbar} U_0^\dagger(t, t_0) H'(t) U_0(t, t_0) \, |\psi_I(t)\rangle = \frac{d}{dt} \, |\psi_I(t)\rangle \tag{2.66}$$

$$-\frac{i}{\hbar} H'_I(t) \, |\psi_I(t)\rangle = \frac{d}{dt} \, |\psi_I(t)\rangle \, , \tag{2.67}$$

with the (weak) perturbation Hamiltonian, $H'_I(t)$, in the interaction picture. This equation can be solved iteratively for each time interval, τ_i, to yield

$$|\psi_I(t)\rangle = |\psi_I(t_0)\rangle + \sum_{n=1}^{\infty} \left(-\frac{i}{\hbar}\right)^n \int_{t_0}^{t} d\tau_n \int_{t_0}^{\tau_n} d\tau_{n-1} \cdots \int_{t_0}^{\tau_2} d\tau_1 \\ H'_I(\tau_n) H'_I(\tau_{n-1}) \cdots H'_I(\tau_1) |\psi_I(t)\rangle . \tag{2.68}$$

If we convert the above equation to the Schrödinger picture and insert the interaction Hamiltonian, we obtain the time evolution of the wavefunction as

$$|\psi(t)\rangle = |\psi(t_0)\rangle + \sum_{n=1}^{\infty} \left(-\frac{i}{\hbar}\right)^n \int_{t_0}^{t} d\tau_n \int_{t_0}^{\tau_n} d\tau_{n-1} \cdots \int_{t_0}^{\tau_2} d\tau_1 \\ U_0(t,\tau_n) H'(\tau_n) U_0(\tau_n,\tau_{n-1}) H'(\tau_{n-1}) \cdots U_0(\tau_2,\tau_1) H'(\tau_1) U_0(\tau_1,t_0) |\psi(t)\rangle . \tag{2.69}$$

Despite the complicated form, this equation offers an appealing interpretation: The system evolves freely according to $U_0(\tau_1, t_0)$. At τ_1 the perturbation $H'(\tau_1)$ interacts with the system followed by free propagation until the next perturbation arises. This can be diagrammatically represented in single-time-line Feynman diagrams.

A similar expression is obtained in the density matrix formalism and gives in the Schrödinger picture

$$\rho(t) = \rho^{(0)}(t) + \sum_{n=1}^{\infty} \left(-\frac{i}{\hbar}\right)^n \int_{t_0}^{t} d\tau_n \int_{t_0}^{\tau_n} d\tau_{n-1} \cdots \int_{t_0}^{\tau_2} d\tau_1 \\ U_0(t,\tau_n)[H'_I(\tau_n), [H'_I(\tau_{n-1}), \cdots [H'_I(\tau_1), \rho(t_0)] \cdots]] U_0^{\dagger}(t,t_0). \tag{2.70}$$

In contrast to equation 2.69, the density operator is defined in terms of both bra and ket of the wavefunction. The equation therefore suggests that a perturbation can interact on either side of system leading to the concept of double-sided Feynman diagrams and wave-mixing energy ladder (WMEL) diagrams.

We continue to specify the perturbation to be a time-dependent electric field, $E(t)$, interacting with the dipole moment, μ, of the system

$$H'(t) = \mu E(t). \tag{2.71}$$

Under the assumption that $\rho(t_0)$ is an equilibrium density matrix, we can further set $t_0 \to -\infty$ and obtain a simplified expression

$$\rho(t) = \rho^{(0)}(-\infty) + \sum_{n=1}^{\infty} \rho^{(n)}(t), \tag{2.72}$$

with the n^{th}-order density matrix being

$$\rho^{(n)}(t) = \left(-\frac{i}{\hbar}\right)^n \int_{-\infty}^{t} d\tau_n \int_{-\infty}^{\tau_n} d\tau_{n-1} \cdots \int_{-\infty}^{\tau_2} d\tau_1 E(\tau_n)E(\tau_{n-1})\cdots E(\tau_1) \\ U_0(t,\tau_n)[\mu_I(\tau_n),[\mu_I(\tau_{n-1}),\cdots[\mu_I(\tau_1),\rho(-\infty)]\cdots]]U_0^\dagger(t,t_0), \tag{2.73}$$

and the dipole operator in the interaction picture given as

$$\mu_I(t) = U_0^\dagger(t,t_0)\mu U_0(t,t_0). \tag{2.74}$$

We are now able to express the full density matrix evolution for an unlimited number of weak electric field interactions at various time delays with the system. Since we are interested in the macroscopic polarisation, P, induced by the electric field, μ, we require a connection between the density matrix and an observable, which is given in this case as

$$\langle P\rangle = \mathrm{Tr}(\mu\rho(t)) \equiv \langle\mu\rho(t)\rangle\,, \tag{2.75}$$

where $\langle\cdots\rangle$ denotes the expectation value and $\mathrm{Tr}(\cdots)$ indicates the trace of the matrix. The n^{th}-order polarisation thus given as

$$P^{(n)}(t) = \left(-\frac{i}{\hbar}\right)^n \int_{-\infty}^{t} d\tau_n \int_{-\infty}^{\tau_n} d\tau_{n-1} \cdots \int_{-\infty}^{\tau_2} d\tau_1 E(\tau_n)E(\tau_{n-1})\cdots E(\tau_1) \\ \langle\mu(t)[\mu(\tau_n),[\mu(\tau_{n-1}),\cdots[\mu(\tau_1),\rho(-\infty)]\cdots]]\rangle\,. \tag{2.76}$$

In spectroscopy, this is usually expressed in time intervals between field interactions, rather then absolute time points. Using the definition $\tau_1 = 0$, $t_1 = \tau_2 - \tau_1$, $t_2 = \tau_3 - \tau_2$, etc. we obtain

$$P^{(n)}(t) = \int_0^\infty dt_n \int_0^\infty dt_{n-1} \cdots \int_0^\infty dt_1 \\ E(t-t_n)E(t-t_n-t_{n-1})\cdots E(t-t_n-\cdots-t_1)R^{(n)}(t_n,t_{n-1},\cdots,t_1). \tag{2.77}$$

where the nonlinear response function, $R^{(n)}(\cdots)$, is defined as

$$R^{(n)}(t_n,t_{n-1},\cdots,t_1) = \left(-\frac{i}{\hbar}\right)^n \langle\mu(t_n+\cdots+t_1)[\mu(t_{n-1}+\cdots+t_1),\cdots \\ [\mu(0),\rho(-\infty)]\cdots]]\rangle\,. \tag{2.78}$$

We point out that the last interaction $\mu(t_n+\cdots+t_1)$ corresponds to the emission of a signal from the system to generate overall an equilibrium density matrix, while the other interactions (within the commutator) can generate a non-equilibrium density matrix. This equation forms the basis for frequently employed diagrammatic guides to understand possible signal pathways in multi-pulse experiments, like double-sided Feynman and WMEL diagrams.

2.2.2 First-Order Linear Spectroscopy

Linear Macroscopic Polarisation of a Two-Level System

After formally introducing the density matrix formalism and its connection to the macroscopic polarisation under an electric field perturbation, we are now able to apply this knowledge to obtain information about the system from experimental results, or *vice versa*. We start by considering linear spectroscopy on the previously introduced two-level system. The full Hamiltonian describing the interaction with an electric field reads

$$H(t) = H_0 + H'(t) \tag{2.79}$$
$$= H_0 - E(t)\mu \tag{2.80}$$
$$= \begin{pmatrix} \epsilon_1 & 0 \\ 0 & \epsilon_2 \end{pmatrix} - E(t) \begin{pmatrix} 0 & \mu_{12} \\ \mu_{21} & 0 \end{pmatrix}, \tag{2.81}$$

where $\mu_{21} = \mu_{12}^*$ represents the transition dipole moment coupling the two states. The first-order polarisation is defined according to equation 2.77 as

$$P^{(1)}(t) = \int_0^\infty dt_1 E(t - t_1) R^{(1)}(t_1). \tag{2.82}$$

In linear absorption only one field interaction (either on the bra or ket side) is present, leading to two terms contributing to $R^{(1)}(t_1)$. The response function can be written as

$$R^{(1)}(t_1) = -\frac{i}{\hbar} \langle \mu(t_1), [\mu(0), \rho(-\infty)] \rangle \tag{2.83}$$
$$= -\frac{i}{\hbar} \left(\langle \mu(t_1)\mu(0)\rho(-\infty) \rangle - \langle \mu(t_1)\mu(0)\rho(-\infty) \rangle^* \right), \tag{2.84}$$

where we have assumed that all operators are Hermitian and that the expectation value is invariant under cyclic permutation. The commutator is best examined step by step starting from the right. Before $t = 0$ the system remains unchanged and is described by $\rho(-\infty)$. Interaction with the electric field at $t = 0$ ($\mu(0)$) will generate a time-dependent density matrix $\rho(t)$ according to

$$\rho(t) = \mu(0)\rho(-\infty) \tag{2.85}$$
$$= \begin{pmatrix} 0 & \mu_{12} \\ \mu_{21} & 0 \end{pmatrix} \begin{pmatrix} \rho_{11}(-\infty) & \rho_{12}(-\infty) \\ \rho_{21}(-\infty) & \rho_{22}(-\infty) \end{pmatrix} \tag{2.86}$$
$$= \begin{pmatrix} \mu_{12}\rho_{21}(-\infty) & \mu_{12}\rho_{22}(-\infty) \\ \mu_{21}\rho_{11}(-\infty) & \mu_{21}\rho_{12}(-\infty) \end{pmatrix} \tag{2.87}$$
$$\equiv \begin{pmatrix} \tilde{\rho_{11}}(t) & \tilde{\rho_{12}}(t) \\ \tilde{\rho_{21}}(t) & \tilde{\rho_{22}}(t) \end{pmatrix}. \tag{2.88}$$

The system is now no longer in an eigenstate and will oscillate in time as shown in equation 2.54 between the two states with a frequency $\omega_{21} = \frac{\epsilon_2 - \epsilon_1}{\hbar}$ propagated by $U_0(t, t_0)$. The generated oscillations are also known as Rabi oscillations and follow

$$\begin{aligned} \tilde{\rho_{12}}(t) &= \tilde{\rho_{12}}(-\infty)\mathrm{e}^{+i\omega_{21}t} \\ \tilde{\rho_{21}}(t) &= \tilde{\rho_{21}}(-\infty)\mathrm{e}^{-i\omega_{21}t}, \end{aligned} \tag{2.89}$$

while the terms $\tilde{\rho_{11}}(t)$ and $\tilde{\rho_{22}}(t)$ remain constant. At t_1, the system emits the signal ($\mu(t_1)$) which results in

$$\rho(t_1) = \mu(t_1)\rho(t) \tag{2.90}$$

$$= \begin{pmatrix} 0 & \mu_{12} \\ \mu_{21} & 0 \end{pmatrix} \begin{pmatrix} \tilde{\rho_{11}}(t) & \tilde{\rho_{12}}(t) \\ \tilde{\rho_{21}}(t) & \tilde{\rho_{22}}(t) \end{pmatrix} \tag{2.91}$$

$$= |\mu_{21}|^2 \begin{pmatrix} \rho_{11}(-\infty)\mathrm{e}^{-i\omega_{21}t} & \rho_{12}(-\infty) \\ \rho_{21}(-\infty) & \rho_{22}(-\infty)\mathrm{e}^{i\omega_{21}t} \end{pmatrix}. \tag{2.92}$$

The response function can now be calculated from equation 2.84 in combination with equation 2.75

$$R^{(1)}(t_1) = -\frac{i}{\hbar}\left(\langle\mu(t_1)\mu(0)\rho(-\infty)\rangle - \langle\mu(t_1)\mu(0)\rho(-\infty)\rangle^*\right) \tag{2.93}$$

$$= -\frac{i}{\hbar}|\mu_{21}|^2 \left(\rho_{11}(-\infty)\mathrm{e}^{-i\omega_{21}t_1} + \rho_{22}(-\infty)\mathrm{e}^{i\omega_{21}t_1} - \rho_{11}(-\infty)\mathrm{e}^{+i\omega_{21}t_1} - \rho_{22}(-\infty)\mathrm{e}^{-i\omega_{21}t_1}\right) \tag{2.94}$$

$$= -\frac{i}{\hbar}|\mu_{21}|^2(\rho_{11}(-\infty) - \rho_{22}(-\infty))\left(\mathrm{e}^{-i\omega_{21}t_1} - \mathrm{e}^{i\omega_{21}t_1}\right), \tag{2.95}$$

and leads to the total first-order polarisation

$$P^{(1)}(t) = -\frac{i}{\hbar}|\mu_{21}|^2\Delta_\rho \int_0^\infty dt_1 E(t - t_1)\left(\mathrm{e}^{-i\omega_{21}t_1} - \mathrm{e}^{i\omega_{21}t_1}\right), \tag{2.96}$$

where $\Delta_\rho \equiv \rho_{11}(-\infty) - \rho_{22}(-\infty)$. The polarisation is composed of two pathways describing the interaction of the electric field with the bra or the ket side of the density matrix. Both are in principle identical and conventionally only the bra interaction is considered. If we assume no initial population in the second level, i.e. $\rho_{22}(-\infty) = 0$ and set without loss of generality the initial population in the first level equal to one, we obtain the first-order polarisation as:

$$P^{(1)}(t) = -\frac{i}{\hbar}|\mu_{21}|^2 \int_0^\infty dt_1 E(t - t_1)\mathrm{e}^{-i\omega_{21}t_1}. \tag{2.97}$$

Employing an electric field

$$E(t) = E_0(t) \cdot \left(\mathrm{e}^{-i\omega_{21}t} + \mathrm{e}^{i\omega_{21}t}\right), \tag{2.98}$$

provides us with two terms in the first-order polarisation

$$\begin{aligned} P^{(1)}(t) = &- \frac{i}{\hbar}|\mu_{21}|^2 \mathrm{e}^{-i\omega_{21}t} \int_0^\infty dt_1 E_0(t-t_1) \\ &- \frac{i}{\hbar}|\mu_{21}|^2 \mathrm{e}^{-i\omega_{21}t} \int_0^\infty dt_1 E_0(t-t_1) \mathrm{e}^{-i2\omega_{21}t_1}. \end{aligned} \tag{2.99}$$

The second term can be ignored since it is quickly oscillating and averages out. This is known as the rotating-wave approximation (RWA). If we proceed by assuming a short resonant pulse, we can make use of the semi-impulsive limit and represent the electric field as

$$E_0(t) = E_0 \mathrm{e}^{-i\omega t}\delta(t), \tag{2.100}$$

where $\delta(t)$ denotes the delta function. The polarisation becomes

$$P^{(1)}(t) = -\frac{i}{\hbar}|\mu_{21}|^2 E_0 \mathrm{e}^{-i\omega_{21}t}, \tag{2.101}$$

showing that the macroscopic polarisation induced by the sample oscillates at ω_{21} and is strongly dependent on the transition dipole moment connecting the two states. This equation is easily modified to account for different initial populations, as well as dephasing, Γ, of the electronic coherence

$$P^{(1)}(t) = -\frac{i}{\hbar}|\mu_{21}|^2 \Delta_\rho E_0 \mathrm{e}^{-i\omega_{21}t} \mathrm{e}^{-\Gamma t}, \tag{2.102}$$

which is experimentally found to occur on the femtosecond time scale.

Detection of the First-Order Polarisation

Up to now we only calculated the response of the sample to an electric field, but have not yet computed the resulting absorption spectrum. It is important to realise that the emitted signal field, $E^{(1)}$, is necessarily collinear with the incident electric field. The signal in this case is said to be heterodyne detected. Additionally, available detectors measure the intensity rather than the electric field and are typically slow compared to electronic dephasing times. If the

signal was measured without spectral dispersion, the recorded intensity would correspond to

$$I = \int_0^\infty dt \left| E_0(t) + E^{(1)}(t) \right|^2 \tag{2.103}$$

$$= \int_0^\infty dt \left| E_0(t) \right|^2 + \left| E^{(1)}(t) \right|^2 + 2\Re \left(E_0(t) E^{(1)}(t) \right). \tag{2.104}$$

In the case of a spectral dispersion element prior to detection, the electric fields are Fourier transformed to give

$$I(\omega) = \left| E_0(\omega) \right|^2 + \left| E^{(1)}(\omega) \right|^2 + 2\Re \left(E_0(\omega) E^{(1)}(\omega) \right), \tag{2.105}$$

where the second term due to the weak perturbation is small and can be neglected. The absorption spectrum is then defined as

$$\frac{I}{I_0} = \frac{\left| E_0(\omega) + E^{(1)}(\omega) \right|^2}{\left| E_0(\omega) \right|^2} \tag{2.106}$$

$$\Rightarrow -\log_{10}\left(\frac{I}{I_0}\right) \approx -2\Re \left(E^{(1)}(\omega) \right), \tag{2.107}$$

if a δ-pulse is employed. The emitted signal field can be shown to have a phase lag of $\pi/2$ with respect to the induced polarisation, such that

$$E^{(1)}(\omega) \propto -iP^{(1)}(\omega), \tag{2.108}$$

giving a general expression for the absorption spectrum, which leads to the familiar Lorentzian lineshape often encountered in absorption spectra, expressed as optical density (absorbance)

$$\mathrm{OD} = -\log_{10}\left(\frac{I}{I_0}\right) \tag{2.109}$$

$$\propto 2\Im \left(P^{(1)}(\omega) \right) \tag{2.110}$$

$$= \frac{2}{\hbar} |\mu_{21}|^2 \Delta_\rho E_0 \Re \left(\int_0^\infty dt \; \mathrm{e}^{i(\omega-\omega_0)t} \mathrm{e}^{-\Gamma t} \right) \tag{2.111}$$

$$\propto \frac{|\mu_{21}|^2 \Gamma}{(\omega-\omega_0)^2 + \Gamma^2}, \tag{2.112}$$

where we assumed a δ-pulse with constant frequency ω_0. Note that the factor Δ_ρ accounts for the ensemble average and is typically modelled by a Boltzmann distribution. The linear electronic absorption spectrum can therefore be predicted if the electronic transition dipole moments are known.

2.2.3 Third-Order Pump-Probe Spectroscopy

We consider now a three-level system with states $|1\rangle$, $|2\rangle$, $|3\rangle$ and $\mathrm{E}_1<\mathrm{E}_2<\mathrm{E}_3$, initially in the ground state. Pump-probe spectroscopy leads to three electric field interactions (two pump, one probe) to generate a signal field. The third-order polarisation can be written as

$$P^{(3)}(t) = \int_0^\infty dt_3 \int_0^\infty dt_2 \int_0^\infty dt_1 E(t-t_3)E(t-t_3-t_2) \\ E(t-t_3-t_2-t_1)R^{(3)}(t_3,t_2,t_1). \tag{2.113}$$

$R^{(3)}(t_3,t_2,t_1)$ consists of $2^3 = 8$ pathways which are pairwise conjugated. We therefore need to consider only 4 distinct third-order response functions. If we assume the three sinusoidal electric fields to be centred around $t = 0$ we have to express each field in equation 2.113 as the sum of three pulses with frequency $\pm\omega$, leading to 6 terms. This results in a total of $6^3 \cdot 4 = 884$ integrals to be calculated. A fraction of these pathways lead to the coherent artefact observed in this type of spectroscopy. Fortunately, the number can be considerably reduced if we impose strict time ordering between the pump and the probe fields and choose a geometry in which we heterodyne the signal with the probe field to obtain 8 remaining terms. An additional two can be removed by the rotating-wave approximation, giving a total of 6 signal pathways. If the experiment is additionally carried out with a short pump pulse compared to the system dynamics, we find that overall three distinct signals known as ground-state bleach (GSB), photoinduced absorption (PIA) and stimulated emission (SE) appear in a standard pump-probe experiment. The corresponding nonlinear responses can be obtained in the same way as previously or alternatively from the rules of double-sided Feynman diagrams or WMEL diagrams (Figure 2.3)

$$R^{(3)}_{\mathrm{SE}}(t_3,t_2,t_1) \propto \frac{i}{\hbar^3}\mu_{21}^4 \mathrm{e}^{-i\omega_{21}t_3}\mathrm{e}^{-\Gamma t_3} \tag{2.114}$$

$$R^{(3)}_{\mathrm{GSB}}(t_3,t_2,t_1) \propto \frac{i}{\hbar^3}\mu_{21}^4 \mathrm{e}^{-i\omega_{21}t_3}\mathrm{e}^{-\Gamma t_3} \tag{2.115}$$

$$R^{(3)}_{\mathrm{PIA}}(t_3,t_2,t_1) \propto -\frac{i}{\hbar^3}\mu_{21}^2\mu_{32}^2 \mathrm{e}^{-i\omega_{32}t_3}\mathrm{e}^{-\Gamma t_3}, \tag{2.116}$$

where we assumed no evolution on $|2\rangle$ and equal dephasing rates.

The total nonlinear polarisation in the semi-impulsive limit then becomes

$$P^{(3)}(t) = \frac{i}{\hbar^3}\left(4\mu_{21}^4 \mathrm{e}^{-i\omega_{21}t_3}\mathrm{e}^{-\Gamma t_3} - 2\mu_{21}^2\mu_{32}^2 \mathrm{e}^{-i\omega_{32}t_3}\mathrm{e}^{-\Gamma t_3}\right). \tag{2.117}$$

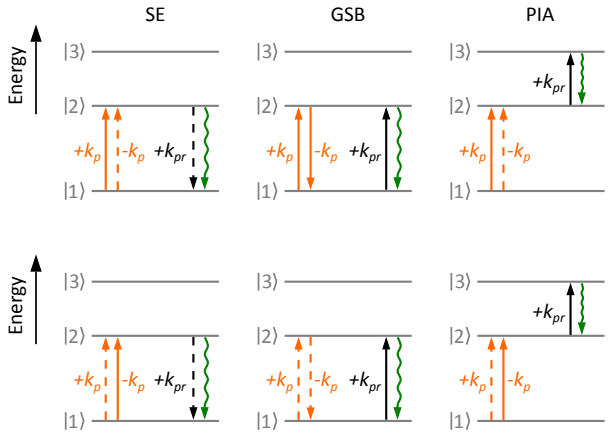

Figure 2.3: Wave-mixing energy ladder diagrams in pump-probe spectroscopy showing possible signal pathways and corresponding wave vectors observed in a heterodyned pump-probe experiment. The pump pulse is assumed to be short and temporally separated from the probe pulse. Vertical solid and dashed lines represent an electric field interaction on the bra or the ket of the density matrix. Orange - pump (p), black - probe (pr), green - signal.

Subsequently, the spectrally resolved signals in a pump-probe experiment measured normalised to the probe can be calculated

$$\Delta\mathrm{OD} \propto -2\Im\left(P^{(3)}(\omega)\right) \tag{2.118}$$

$$= -\frac{8\mu_{21}^4\Gamma}{(\omega_{21}-\omega_0)^2+\Gamma^2} + \frac{4\mu_{21}^2\mu_{32}^2\Gamma}{(\omega_{32}-\omega_0)^2+\Gamma^2}. \tag{2.119}$$

The typical Lorentzian shape as observed for linear absorption is retained. While SE and GSB have the same negative signal ($\propto \mu_{21}^4$), PIA shows a positive sign ($\propto \mu_{21}^2\mu_{32}^2$), allowing us to identify excited-state pathways in pump-probe spectroscopy based on the observed sign.

In this derivation we assumed no evolution during t_2 and neglected vibrational energy levels. The above treatment can be generalised to account for the generation of vibrational coherence during the first two pump interaction, which will be discussed more qualitatively in the next chapter.

Chapter 3

Experimental Methods

The following chapter describes the experimental setups used in this work. We start by discussing the generation of various pulses, their characterisation via second-harmonic generation frequency-resolved optical gating (SHG-FROG) and conclude with experimental techniques. Parts of this chapter are adapted with permission from the following publications:

- M. Liebel, C. Schnedermann and P. Kukura, *Opt. Lett.*, 2014, **39**, 4112-5.[64] This paper was published in Optics Letters and is made available as an electronic reprint with the permission of OSA. The paper can be found at the following URL on the OSA website: `http://dx.doi.org/10.1364/OL.39.004112`. Systematic or multiple reproduction or distribution to multiple locations via electronic or other means is prohibited and is subject to penalties under law.

- T. Wende, M. Liebel, C. Schnedermann, R. J. Pethick and P. Kukura, *J. Phys. Chem. A*, 2014, **118**, 9976-84. Copyright 2014 American Chemical Society.[65]

- M. Liebel, C. Schnedermann, T. Wende and P. Kukura, *J. Phys. Chem. A*, 2015, **119**, 9506-17. Copyright 2015 American Chemical Society.[66]

3.1 Pulse Generation

All pulses employed in this work are provided by a Lightconversion Pharos-6W (Yb:KGW) amplifier system (200 fs, 1030 nm, 600 μJ). We split off 50 μJ to seed various whitelight (WL) stages, while the remaining fundamental is frequency-doubled via second-harmonic generation (SHG)[57,58] in a type I

phase-matched β-barium-borate crystal (BBO, 23.4°). This is followed by sum-frequency generation (SFG)[59] of the fundamental with the second harmonic in a type II phase-matched BBO (62.8°) to yield 200 fs pulses centred at 515 nm (250 μJ) and 343 nm (60 μJ), respectively.

3.1.1 Probe Pulses: Whitelight Continuum Generation

WL continuum generation allows significant broadening of a narrowband input pulse by focussing it with sufficient peak intensity into a bulk medium, such as sapphire. The physical basis of WL continuum generation has been discussed in various excellent reports.[62,63] Briefly, focussing of a high-energy femtosecond pulse into a bulk crystal triggers an optical Kerr effect, which leads to self-focussing of the beam. This results in drastically increased peak intensities, which activates multiphoton ionisation generating a local weakly ionised plasma spot. The accompanied change in refractive index forces the beam to diverge before self-focussing leads to the formation of another plasma spot. This process is repeated several times until the beam exits the bulk material leading to the formation of a plasma filament in the crystal. During this propagation various other nonlinear effects such as self-phase-modulation, self-steepening, and medium ionisation, generate additional frequencies predominantly on the high-energy side of the initial pulse spectrum, forming a WL continuum. Despite its complex physical description, WL continua are routinely employed in spectroscopy, due to their simple experimental implementation.[67–71]

We employ WL continua as probe pulses in transient absorption (TA) experiments and as seed pulses in multiple non-collinear optical parametric amplification (NOPA) stages.[66] For their generation we focus 2-3 μJ of a narrowband seed pulse (200 fs) into a 3 mm sapphire crystal with an achromatic lens (F = 100 mm). To minimise accumulated chirp, we collimate the resulting WL by means of a curved mirror (F = 50 mm, Figure 3.1a). Keeping the reflection angle of the curved mirror small reduces astigmatism, and the subsequent use of an iris enables selection of the most spatially homogeneous region of the WL. The use of a harmonic separator (0° AOI, EKSMA Optics) removes the residual seed pulse, providing a WL with a broad seed-dependent spectral coverage (Figure 3.1b). A seed wavelength of 1030 nm generates WL continua covering the spectral region from 500-900 nm, which can be tuned further to the blue (450-700 nm) if the seed wavelength is changed to 780 nm. To achieve an even bluer WL ranging from 400-490 nm a 515 nm seed can be

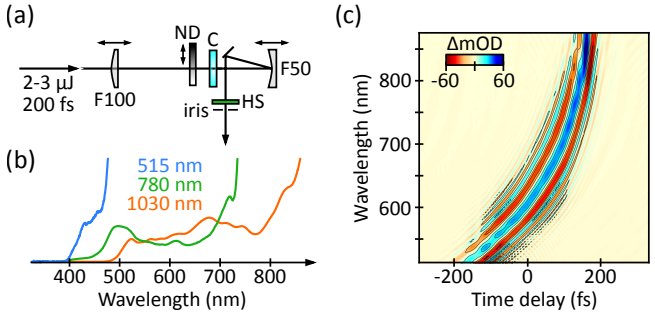

Figure 3.1: Whitelight (WL) generation and characterisation. (a) Typical setup for WL generation. Double-sided arrows indicate translation-stage mounting. (b) Spectral coverage for different seed wavelengths. (c) Temporal characteristics of a 1030 nm (200 fs) seeded sapphire WL obtained in a transient absorption measurement using a 10 fs visible pump pulse. The observed chirp of the WL indicates a probe duration of ∼300 fs. C - sapphire crystal (3 mm), ND - variable neutral-density filter, HS - harmonic separator (0° AOI, 1030 nm, EKSMA Optics). The WL spectrum pumped at 515 nm was provided by Alex S. Duarte, while 780 nm and 1030 nm pumped WL spectra were provided by Matz Liebel.

employed. Fine tuning of the seed power for optimal generation of a shot-noise limited WL is assured by an additional variable neutral-density filter close to the sapphire crystal. An alternative approach to generate blue-shifted WL continua involves different crystal materials. We find that fused silica (FS) shifts the blue edge to ∼450 nm, while calcium fluoride (CaF_2) extends the WL to 400 nm if seeded by 1030 nm (200 fs) pulses. At a repetition rate of 10 kHz, these materials have to be translated to avoid accumulation of thermal damage, which leads to a decreased shot-to-shot stability by an order of magnitude rendering seed-wavelength tuning a preferred approach.

Typical output powers of this setup are below 4 nJ, making WL pulses ideal weak-field probes for spectroscopy.[54] To generate a good spatial WL mode, as required in spectroscopic applications, it is essential that the seed mode is of high quality. In this context it may be beneficial to expand the seed pulse prior to WL generation and use a hard aperture to select only its most symmetric central spatial part. We find that seed-beam diameters of ∼3-5 mm in combination with a near-IR achromatic lens (F = 100 mm) provide a spatially homogeneous Gaussian-shaped WL mode.

The process of WL generation ultimately leads to temporally chirped pulses due to group-velocity dispersion (GVD) and third-order dispersion (TOD) as the pulse propagates through material.[51] The temporal characteristics can be assessed using TA with a short (<10 fs) pump pulse. In this work, we focus on

1030 nm seeded WL probes which have a duration of ∼300 fs with our setup (Figure 3.1c). A bluer WL continuum generated in the same way, will show more chirp due to the wavelength-dependent refractive index variation (∼500 fs for 515 nm seeded WL).

3.1.2 Pump Pulses

Typical WL continua have low intensities (<4 nJ) and are often too broad for spectroscopic applications requiring a more selective pulse spectrum with higher intensities. NOPAs have been developed to improve these shortcomings.[72–74] An excellent review on the topic can be found in Cerullo *et al.*[60] In short, the device is based on overlapping a WL pulse with a high-intensity narrowband pump pulse in a birefringent crystal such as BBO. The underlying process is a non-collinear implementation of difference-frequency generation (DFG) which results in a parametric amplification of the WL spectrum. By carefully adjusting the phase-matching conditions (pump-seed angle and crystal angle), it is possible to amplify parts of the WL red-shifted from the pump wavelength. These parameters can be obtained from programs such as SNLO. In the following we describe key principles in designing NOPAs for various spectroscopic applications, requiring short broadband pulses in the blue, visible and near-IR as well as spectrally tunable narrowband pulses in the near-IR.[66]

<10 fs near-IR Pulses Delivered by a 515 nm Pumped NOPA

NOPAs amplify WL continua to the low-energy side of the pump wavelength, allowing us to use the second harmonic of our laser system (515 nm) to achieve broadband amplification in the near-IR (650-1000 nm).[60,64] To this end, we focus 40 μJ of a 515 nm pump pulse (F = 500 mm lens) together with a 1030 nm sapphire WL (F = 1000 mm curved mirror) under an external angle of 4.1° into a type I phase-matched BBO crystal (2 mm, 23.4°). The resulting output is collimated (F = 200 mm curved mirror) and compressed using 7 bounces on a pair of TOD-optimised near-IR chirped mirrors and a pair of fused silica 2° apex angle wedge prisms (Layertec, Figure 3.2a). This NOPA produces near transform-limited (TL) <10 fs pulses centred around 800 nm with output powers up to 3 μJ (7.5% conversion efficiency). A typical output spectrum and retrieved SHG-FROG trace is shown in Figure 3.2b. The broad bandwidth required for short pulse generation limits the spectral tunability to centre frequencies ranging from 770-880 nm.

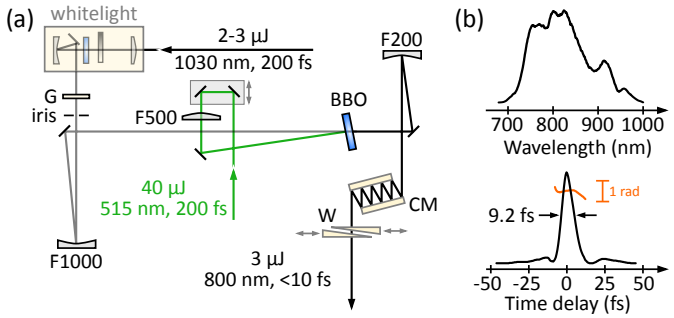

Figure 3.2: <10 fs near-IR pulses delivered by a 515 nm pumped NOPA. (a) Experimental configuration of a NOPA pumped by 40 μJ of 515 nm, 200 fs pulses in combination with a 1030 nm WL seed, generating <10 fs near-IR pulses (700-900 nm). (b) Typical output spectrum (top) and temporal characteristics retrieved via SHG-FROG (bottom). G - sapphire glass window (2 mm), CM - chirped mirrors (Layertec), W - 2° apex angle wedge prism pair (Layertec), BBO - β-barium-borate crystal (21.5°, 2 mm).

We find that optimal operation results if the temporal widths of pump and seed pulse (amplified region) are matched for maximum temporal interactions. In our setup we realise this by inserting a 2 mm sapphire window into the WL, while using reflective optics otherwise. To obtain compressible pulses, we adjust the peak intensity at the crystal to ~150 GW/cm^2, avoiding unwanted nonlinear effects, which can complicate the spatio-temporal profile of the output. This is achieved by placing the crystal behind the focus of pump (85 mm) and seed (50 mm) and employing long focal length optics. The chosen focal length combination (F_{seed} = 1000 mm, F_{pump} = 500 mm) leads to a 2.5 times larger pump spot size at the crystal compared to the seed spot size, thus improving spatially uniform amplification for a good mode profile. Fine adjustments are carried out using a hard aperture in the WL seed (~1-2 mm diameter) and varying the WL collimation mirror for an optimally compressed pulse. Since the generated pulses will be employed for spectroscopic purposes, we focus in this design on good beam parameters (mode quality, compressibility and long-term stability) at the expense of conversion efficiency.

200-300 fs Tunable Dump Pulses in the Near-IR

Narrowband pulses covering the range from 650-950 nm are generated using similar design principles as described above. We generate a 1030 nm sapphire WL acting as the seed pulse and amplify with 20 μJ of 515 nm pulses focussed (F = 250 mm lens) into a 2 mm type I BBO crystal (23.5°) under broadband

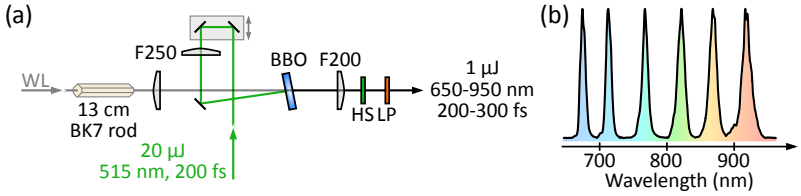

Figure 3.3: Narrowband near-IR pulses delivered by a 515 nm pumped NOPA. (a) Experimental configuration of a narrowband NOPA pumped by 20 μJ of 515 nm, 200 fs pulses in combination with a 1030 nm WL seed, generating tunable near-IR pulses of 200-300 fs duration. The use of the BK7 rod temporally chirps the seed allowing selective amplification by adjusting the time delay between seed and pump pulses. (b) Typical output spectra demonstrating wavelength tunability from 650-950 nm. HS - harmonic separator (0° AOI, 1030 nm, EKSMA Optics), LP - long-pass filter (0° AOI, 600 nm, Thorlabs), BBO - β-barium-borate crystal (23.5°, 2 mm), WL - whitelight.

phase-matched conditions (4.1° external pump-seed angle, Figure 3.3a). The output is collimated (F = 200 mm lens) and passed through a 1030 nm harmonic separator (0° AOI, EKSMA Optics) and a 600 nm long-pass filter (Thorlabs) to exclude fundamental and pump pulse contributions. Figure 3.3b shows typical output spectra with 200 fs duration at 1 μJ power.

The bandwidth of the output pulse is adjusted by inserting a 13 cm BK7 rod into the WL seed, leading to drastic temporal broadening. Consequently, only a narrow spectral range is temporally overlapped with the pump, ensuring an output bandwidth of $\sim$200 cm^{-1} (200-300 fs). Broadband phase-matching conditions are chosen to easily change the centre frequency of the output simply by adjusting the time delay of pump and seed pulses via the pump translation stage. To maximise output power we match pump and seed spot diameters for maximum overlap and employ the same focal lengths for similar divergence properties of pump and seed. We employ a lower conversion efficiency (5%) than possible (15-20%) by placing the BBO crystal 25 mm behind the focus of pump and seed in favour of long-term durability, stability and mode quality.

We remark that this NOPA can be extended to yield 325-450 nm (200-300 fs) pulses via subsequent SHG. In that case it is advisable to obtain higher near-IR output powers by increasing the pump power, since significant power losses occur if a good mode profile and long-term stability is desired. Using a pump energy of 90 μJ, we obtain 1 μJ centred at 400 nm, employing a 2 mm BBO crystal (23.5°) for SHG.

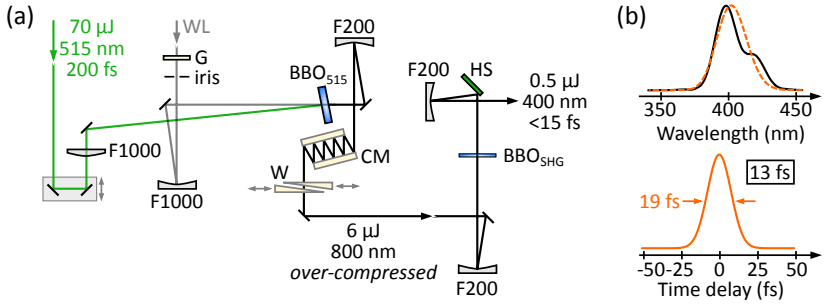

Figure 3.4: <15 fs pulses delivered via SHG of a 515 nm pumped NOPA output. (a) Experimental configuration of a NOPA pumped by 70 μJ of 515 nm, 200 fs pulses in combination with a 1030 nm WL seed, generating <10 fs near-IR pulses centred at 800 nm. The pulse is initially compressed for an additional BK7 window (2 mm) which is removed prior to SHG in a thin BBO crystal (25 μm) resulting in <15 fs pulses centred at 400 nm. (b) Typical output spectrum (top, black) and auto-correlation (envelope, bottom) obtained for a closely resembling simulated Gaussian pulse (top, orange) supporting a pulse duration of 13 fs. G - sapphire glass window (2 mm), CM - chirped mirrors (Layertec), HS - harmonic separator (45° AOI, 800 nm, Layertec), W - 2° apex angle wedge prism pair (Layertec), BBO - β-barium-borate crystal (BBO_{515}: 21.5°, 2 mm, BBO_{SHG}: 29°, 25 μm), WL - whitelight.

<15 fs Pulses Delivered via SHG of a 515 nm Pumped NOPA

The generation of short NOPA pulses around 400 nm is technically challenging since WL pulses at these wavelengths are not supported by common bulk materials (see Figure 3.1b). Instead, a broadband near-IR femtosecond NOPA can yield 400 nm, <15 fs pulses via SHG in a thin BBO crystal (Figure 3.4a). To this end, we generate 6 μJ of <10 fs 800 nm pulses as described earlier, using 70 μJ of a 515 nm pump and a 1030 nm sapphire WL, focussed (F = 1000 mm) into a 2 mm type I BBO crystal (21.5°). The seed pulse duration is adjusted with a 2 mm sapphire window and the BBO crystal position set to ~110 mm behind the focus of the pump and seed beam for spatially uniform and compressible output pulse generation, including a hard aperture for the seed (2 mm diameter). The output is collimated (F = 200 mm curved mirror) and compressed with a pair of TOD-optimised chirped mirrors and fused silica 2° apex angle wedge prisms (Layertec). The output pulse is then focussed (F = 200 mm curved mirror) into a 25 μm type I BBO crystal (29°) for SHG. Subsequently, a harmonic separator (45° AOI, 800 nm, EKSMA Optics) isolates the 400 nm pulses, which are collimated by a curved mirror (F = 200 mm) resulting in 0.5 μJ <15 fs pulses. No additional compression is needed after SHG.

The use of broadband fundamental pulses in SHG leads to chirped output pulses due to material dispersion.[51] Due to the low conversion efficiency, we over-compress the fundamental pulse instead of implementing another compression stage after SHG. We find that the shortest second-harmonic pulses are retrieved if the fundamental pulse is initially compressed for an additional BK7 window (2 mm, 90 fs^2 at 800 nm) which is removed prior to SHG. A typical output spectrum supporting a 13 fs pulse duration is displayed in Figure 3.4b. We use a 25 μm BBO crystal as a compromise between spectral acceptance bandwidth, ultimately limiting the pulse duration, and SHG conversion efficiency. To ensure an excellent mode quality and stability we kept the astigmatism of the fundamental to a minimum. Additionally, we position the SHG-BBO crystal 10 mm behind the focus of the fundamental and mount it on a computer-controlled translation stage (Newport, AG-LS25) for long-term mode and power stability. Since the polarisation of the SHG output is opposite to the fundamental, we additionally insert a reflective waveplate for all experiments carried out. The overall efficiency of 0.7% requires sufficient input power but is adequate for spectroscopy in the linear regime. For higher conversion efficiencies, more sophisticated schemes, such as achromatic frequency-doubling,[75] would have to be employed, dramatically increasing experimental complexity.

<10 fs Visible Pulses Delivered by a 343 nm Pumped NOPA

So far we have discussed the generation of short pulses in the blue and near-IR spectral region. If short visible pulses covering 480-650 nm are required, a NOPA pumped by the third harmonic (343 nm) of our laser system is needed. In principle, this can be achieved in the same way as discussed in the previous sections. It has to be considered, however, that 1030 nm WL sapphire seed pulses show almost no intensity at 500 nm, making amplification difficult. To be able to generate pulses with centre frequencies close to 500 nm, we change the WL by seeding it at 780 nm, rather than the fundamental, leading to an improved intensity distribution around 500 nm (Figure 3.4b).

Our NOPA design consists of WL seed generation with 780 nm in sapphire followed by the actual 343 nm pumped NOPA (amplification) stage (Figure 3.5a). For the WL seed, we construct a 2-stage 515 nm pumped (8 and 12 μJ) NOPA using a 1030 nm pumped sapphire WL seed. We set an external phase-matching angle of 0.8° and employ 2 mm BBO crystals (23.5°) in each stage. In contrast to the previous narrowband NOPA, tunability is not required,

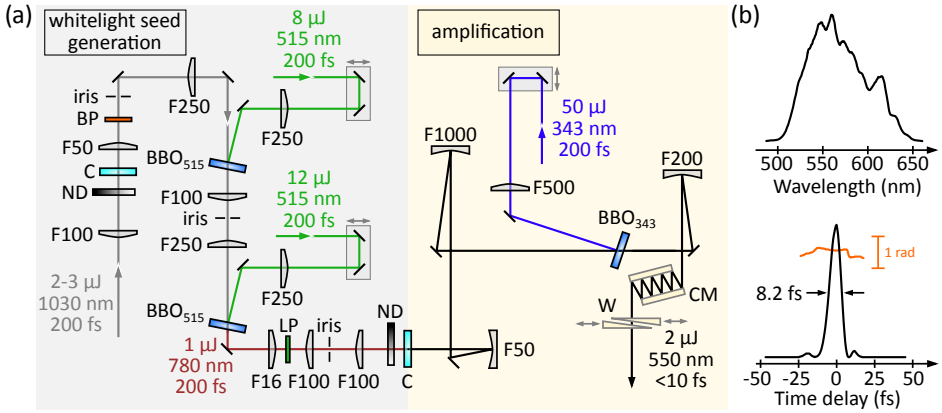

Figure 3.5: <10 fs visible pulses delivered by a 343 nm pumped NOPA. (a) Experimental configuration of a NOPA pumped by 50 μJ of 343 nm, 200 fs pulses using a separately generated 780 nm WL seed. (b) Typical output spectrum (top) and retrieved temporal characteristics obtained via SHG-FROG (bottom). C - sapphire crystal (3 mm), BP - band-pass filter (780 nm, FWHM = 10 nm, Thorlabs), ND - variable neutral-density filter, LP - long-pass filter (550 nm, Thorlabs), CM - chirped mirrors (Layertec), W - 2° apex angle wedge prism pair (Layertec), $BBO_{515,\ 343}$ - β-barium-borate crystal (BBO_{515}: 21.5°, 2 mm, BBO_{343}: 37°, 1 mm).

allowing us to insert a 780 nm band-pass filter (FWHM = 10 nm, Thorlabs) into the 1030 nm WL to spectrally select the required wavelength range. This approach additionally enables easy output power optimisation with a power meter. In both stages we place the BBO crystals 15 mm behind the probe and 25 mm behind the pump focus to ensure good spatial amplification and select a Gaussian beam profile after the first stage using a hard aperture (1-2 mm diameter) before the second stage. This provides good mode quality (elliptical, 2:1 ratio) while maintaining high power conversion. The output is passed through a 550 nm long-pass filter (Thorlabs) to minimise spectral contamination and expanded to a diameter of 10 mm, resulting in ~1 μJ 200 fs pulses at 780 nm. WL generation as described earlier subsequently provides the new WL seed for the NOPA covering a range from 450-700 nm. Special care has to be taken to amplify the same spatial part of the beam in both stages to ensure an excellent mode quality and conversion efficiency, crucial for WL generation. We find that the best output stability is achieved by weakly amplifying in the first stage (8 μJ) followed by stronger amplification in the second stage (12 μJ).

The actual pulse generation employs 50 μJ of 343 nm, 200 fs pump pulses focussed (F = 500 mm lens) into a 1 mm BBO crystal (37°) at an external angle with the WL seed (F = 1000 mm curved mirror) of 7.2°. The BBO is

placed 35 mm behind the focus, leading to peak intensities of ∼150 GW/cm^2. This improves long-term stability and avoids spatio-temporal artefacts. The latter is particularly pronounced in this NOPA due to the blue pump pulse (higher energy photons), which easily produces non-trivial temporal shapes and spatial chirp via 2-photon ionisation.[76] The output is collimated (F = 200 mm curved mirror) and compressed by 8 bounces on a pair of TOD-optimised visible chirped mirrors and a pair of fused silica 2° apex angle wedge prisms (Layertec) to give 2 μJ of <10 fs pulses centred in the visible (Figure 3.5b). As before, we make use of a hard aperture in the WL seed and fine-tune the spot size at the crystal with the WL collimation mirror. The use of a 1 mm BBO yields lower power conversions at the expense of a cleaner and more readily compressible pulse output. The centre frequency can be tuned from 505-590 nm which is limited by the broad bandwidth required for short pulse generation and the acceptance bandwidth of the chirped mirrors.

3.1.3 Pulse-Characterisation via SHG-FROG

The characterisation of short pulses is carried out using cross-correlation SHG frequency-resolved optical gating (SHG-FROG).[77] The method is based on splitting an unknown pulse into two identical copies, spatially separating and focussing them into a thin crystal (BBO). Each pulse will generate a second-harmonic signal along its propagation direction using two photons from the same pulse. Additionally, a third second-harmonic pulse is emitted utilising one photon from each pulse instead (cross correlation). Phase-matching considerations dictate that this beam is spatially located at exactly half the distance between the other second-harmonic signals, allowing for a background-free measurement of the cross correlation. Detection is carried out in a frequency-resolved fashion with a spectrometer while one beam is stepped in time across the other with a computer-controlled translation stage (Newport, Figure 3.6a). The intensity $I_{\mathrm{FROG}}^{\mathrm{SHG}}$ of the cross-correlation as a function of time-delay, τ, and detection frequency, ω, is then given as

$$I_{\mathrm{FROG}}^{\mathrm{SHG}}(\omega,\tau) = \left| \int_{-\infty}^{\infty} E(t)E(t-\tau)e^{-i\omega t}dt \right|^2, \tag{3.1}$$

where $E(t)$ denotes the time-dependent component of the pulsed electric field.

A typical SHG-FROG trace for a <10 fs pulse centred at 550 nm is given in Figure 3.6b. Based on this trace, an iterative algorithm (Swamp Optics,

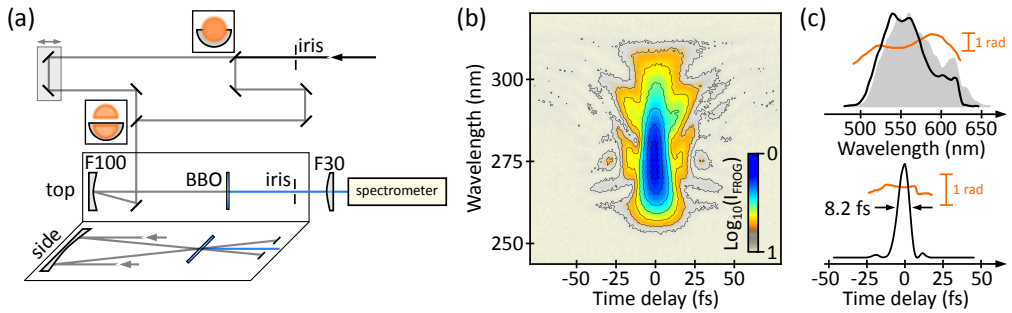

Figure 3.6: Second-harmonic generation frequency-resolved optical gating (SHG-FROG). (a) Experimental configuration of an ultrafast SHG-FROG setup. The incoming beam is hard aperture cut into two replicas and subsequently overlapped non-collinearly in a 10 μm thin BBO crystal. The time delay dependent cross correlation (blue) is isolated and recorded by a spectrometer. (b) Typical SHG-FROG traces obtained for <10 fs visible pulses. Note the logarithmic intensity scale. (c) Top: Retrieved spectrum (black) and spectral phase (orange) overlaid with the measured spectrum (grey). Bottom: Retrieved temporal profile (black) and phase (orange).

FROG version 3.2.4) recreates the trace and thereby retrieves the full spectral and temporal characteristics of the pulsed electric field.

A particularly useful property of the SHG-FROG signal is its time-delay mirror symmetry (Figure 3.6b) which enables easy alignments and thus provides a fast pulse characterisation technique (Figure 3.6c). Our SHG-FROG setup employs spatial hard-aperture splitting of the unknown pulse to create identical pulse copies. The setup is designed to be all-reflective to avoid temporal broadening due to additional material insertion, particularly pronounced for very short pulses (<10 fs). The spatially separated pulse copies are subsequently focussed (F = 100 mm curved mirror) into a thin BBO crystal and the cross correlation is detected by a spectrometer (B&W Tek, Lambda Photometrics). Special care is taken to minimise spatial chirp and polarisation artefacts. The SHG-BBO crystal is chosen to have a thickness of 10 μm to accommodate a large acceptance bandwidth required to reliable characterise pulses down to 7 fs. Below, phase-matching conditions require an even thinner crystal to match the full SHG bandwidth. In such cases, other pulse characterisation techniques like SEA-TADPOLE[78] or iFROG[79] can lead to more reliable results.

3.2 Spectroscopic Methods

All experiments presented in this work are based on a single-shot transient absorption (TA) setup. We will first outline the basic principles of TA and corresponding data processing before we proceed to discuss the extension to impulsive vibrational spectroscopy (IVS) and its use in determining Raman spectra of ground and excited electronic states. We conclude with a discussion of three- and four-pulse schemes employed to enable background- and baseline-free detection of excited-state Raman spectra to follow chemical reactions in real time.

3.2.1 Broadband Transient Absorption

TA spectroscopy is commonly used to investigate the time-dependent electronic structure of a system after photoexcitation.[10,27,80] The pulse sequence consists of a pump pulse initiating photoexcitation by promoting a subset of molecules into the excited electronic state. After a variable time delay, Δt, a weaker probe pulse interrogates the system and is subsequently detected in a spectrometer (Figure 3.7a). TA signals are recorded as a normalised differential transmittance (DTT) to enhance signal contrast according to

$$\begin{aligned} \mathrm{DTT}(\lambda, \Delta\mathrm{t}) &= \frac{\Delta T(\lambda, \Delta\mathrm{t})}{T(\lambda)} = \frac{T_{\mathrm{on}}(\lambda, \Delta\mathrm{t}) - T(\lambda)}{T(\lambda)} \\ &= \frac{T_{\mathrm{on}}(\lambda, \Delta\mathrm{t})}{T(\lambda)} - 1, \end{aligned} \tag{3.2}$$

where T is the detected probe transmittance in the absence of the pump pulse and $T_{\mathrm{on}}(\Delta\mathrm{t})$ the transmittance after the pump pulse has interacted with the system. To improve the signal-to-noise ratio (SNR), a mechanical chopper is inserted into the pump beam path operating at half the probe repetition rate such that consecutive laser shots can be used to compute the DTT signal (Figure 3.7b).[81] For chemical applications, it is often useful to convert the DTT signal into a differential optical density signal, ΔOD (absorbance), which shows a linear dependence on concentration, c, via the Lambert-Beer law

$$\begin{aligned} \Delta\mathrm{OD}(\lambda, \Delta\mathrm{t}) &= \Delta(\epsilon(\lambda) c(\Delta\mathrm{t})) l \\ &= -\log_{10}\left(\frac{T_{\mathrm{on}}(\lambda, \Delta\mathrm{t})}{T(\lambda)}\right) \\ &= -\log_{10}(\mathrm{DTT}(\lambda, \Delta\mathrm{t}) + 1), \end{aligned} \tag{3.3}$$

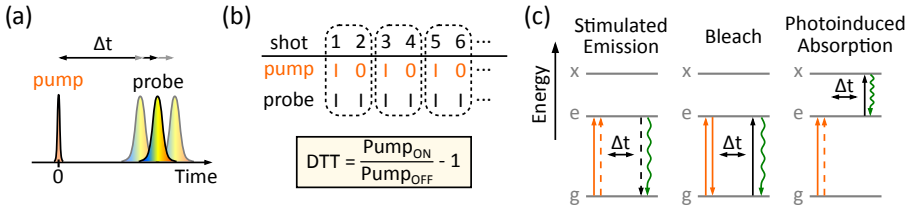

Figure 3.7: Principles of transient absorption (TA) spectroscopy. (a) Pulse sequence. A pump pulse initiates the photoreaction which is investigated by a probe pulse at varying time delays, Δt. (b) Chopping scheme employed in TA. The pump pulse repetition rate is adjusted by a mechanical chopper to half the probe frequency leading to pump ON and pump OFF spectra required to compute a differential TA signal, DTT. (c) Possible signals observed in TA spectroscopy indicated by wave-mixing energy level (WMEL) diagrams. The labels g, e and x refer to ground, excited and higher excited electronic states, while vertical arrows indicate electric field interactions with either the bra (solid) or ket (dashed) side of the wavefunction of the system. Orange - pump, black - probe, dark green - signal.

where ϵ is the decadic molar extinction coefficient and l denotes the pathlength. This representation will be used throughout this work and in further discussions.

Three possible signals can contribute to a TA spectrum (Figure 3.7c). If the pump pulse promotes molecules to an excited electronic state, they can either absorb the probe pulse leading to a photoinduced absorption (PIA, also excited-state absorption, ESA, if assignable) or radiate back to the ground electronic state via stimulated emission (SE). In case of PIA, the detected probe pulse contains fewer photons yielding a positive ΔOD signature, while SE provides the detected probe with more photons resulting in a negative ΔOD signal. The third contribution arises from the reduced attenuation of the probe pulse at the ground-state absorption spectrum after photoexcitation, leading to more detected probe photons and hence a negative ΔOD signal, referred to as ground-state bleach (GSB). Due to potential spectral overlaps between these signals, it is not always possible to unambiguously assign the observed features in TA.

TA experiments typically rely on compressed pump and probe pulses generated by NOPAs. It has, however, been shown that chirped probing provides equivalent results.[82] This opens the door to utilise a WL continuum as probe pulse, which would otherwise be too difficult to temporally compress due to the broad spectral bandwidth. The use of WL probes has two distinct advantages over NOPA pulses: Firstly, the reduced number of nonlinear interactions involved in the generation process leads to an improvement in stability by an

order of magnitude. Secondly, the broader spectral bandwidth extends the observation window spectrally and can thereby simplify spectral assignments. In the case of dispersed detection, it furthermore improves the effective time resolution.[82] In particular, the latter enables recording extremely fast dynamics with <10 fs time resolution, opening up the possibility to record molecular vibrations in real time via IVS.

3.2.2 IVS on Ground Electronic States

Concepts of IVS

In its most fundamental implementation, IVS is identical to TA spectroscopy employing very short (∼10 fs) pump and probe pulses. Due to the extremely large bandwidth of the pulses, multiple vibrational eigenstates are covered within the pulse. The implications of this are best explained considering a two-vibrational-level system. Interaction with the pump pulse leads to generation of vibrational coherence (VC) between all vibrational levels excited within the bandwidth of the impulsive pump (Figure 3.8a). Since this state is no longer an eigenfunction of the system Hamiltonian, the generated VC transfers into a time-dependent signal recorded by the broadband probe pulse which brings the system back to an eigenstate.[83] From a more chemical point of view, it is instructive to consider a harmonic oscillator picture (Figure 3.8b). Here, the interaction with the pump pulse results in the generation of a superposition of vibrational eigenstates (vibrational wavepacket) evolving in time according to the underlying potential energy surface. The time-dependent signal recorded by the probe pulse hence directly reports on the vibrational frequencies of the system and therefore on the molecular structure of the system. From an ensemble perspective we can also think of the impulsive pump as synchronising vibrational motion and thereby inducing a time-dependent macroscopic polarisation in the sample that modulates the refractive index of the material. The interaction of the probe pulse with the sample leads to an energy gain (blue shift) or energy loss (red shift) of the probe depending on the slope of the refractive index change (Figure 3.8c), while the total number of probe photons is preserved.[47,48,84] Impulsively generated signal modulations are hence encoded in the spectral domain and can be extracted using a spectrally-resolved detection scheme.

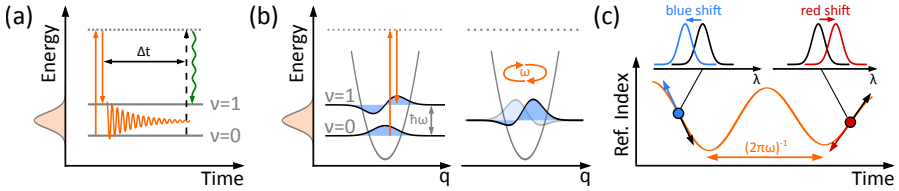

Figure 3.8: Principles of impulsive vibrational spectroscopy (IVS). (a) Wave-mixing energy level diagram illustrating the electric field interactions in IVS. Two field interactions prepare a vibrational coherence (VC) between $\nu = 0$ and $\nu = 1$, which decays as a function of time and is read out by a probe field interaction at varying time delays, Δt. (b) Effect of the impulsive pump pulse on a molecule in the harmonic oscillator approximation. The broad bandwidth of the impulsive pump pulse superimposes multiple vibrational energy levels (left), leading to the generation of a vibrational wavepacket which oscillates according to the given potential at an angular frequency, ω. (c) The interaction with the impulsive pump pulse generates an oscillating macroscopic polarisation resulting in a refractive-index modulation at the angular frequency, ω. This modulation causes energy gain (blue) or loss (red) of the probe pulse, while keeping the number of photons constant, which results in oscillatory spectral modulations of the detected probe.

Our IVS setup employs a 1030 nm chirped WL probe pulse (500-900 nm) in combination with <10 fs pump pulses either in the visible or in the near-IR (Figure 3.9a). The probe is stepped in time with a computer-controlled translation stage (PI, M-230.10 or P-625.1CL) and both pulses are focussed (F = 200 mm curved mirror) into the sample under a minimal reflection angle (<2°). The latter is required to achieve the highest possible effective time resolution by minimising spatial walk-off between pump and probe pulses. All experiments are carried out using parallel polarisations and a 200 or 500 μm pathlength sample flowcell (120 μm coverglasses, BK7) to replenish the sample between consecutive laser shots. Subsequently, we collimate the transmitted probe beam (F = 200 or 500 mm curved mirror) and send it into a home-built prism-based spectrometer equipped with an SF11 prism (60° apex angle), a near-IR achromatic lens (F = 60 mm) and a CMOS array detector (ISG, LW-ELIS-1024A-1394), providing $\leq$60 cm^{-1} spectral resolution.[85] We omit the use of an entrance slit to increase the number of detected photons at the expense of a daily calibration routine,[86] for which we employ the strong spectral modulations caused by an FGB67 filter (Thorlabs) to evaluate the filter response

$$R = \frac{T_{\text{filter}}}{T_{\text{no filter}}}, \tag{3.4}$$

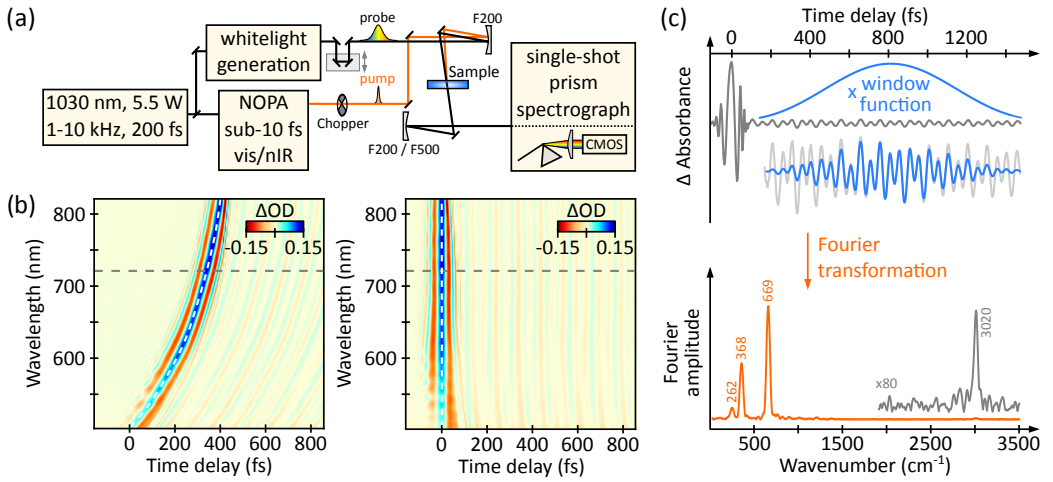

Figure 3.9: Experimental realisation of IVS. (a) Schematic IVS based on a standard transient absorption setup using short pump pulses and chirped continuum WL probe pulses. (b) Off-resonant IVS map for $CHCl_3$ obtained using a 10 fs pump pulses centred at 800 nm and probing with a chirped WL continuum. Left: Raw IVS map. Right: Chirp-corrected IVS map. The white dashed line illustrates the zero time delay position for each detected probe wavelength. (c) Transient at 725 nm (grey dashed line in (b)). Early time delays are CA dominated and excluded from further analysis, the residual coherences are windowed (blue) and subsequently Fourier transformed to give an impulsive Raman spectrum of $CHCl_3$ covering the 50-3000 cm^{-1} frequency range.

where T denotes the detected WL spectrum with or without an inserted filter. By choosing well-defined reference points and subsequently fitting the result to a prism-dispersion equation, we readily obtain the required wavelength calibration.[87] The use of a chirped WL probe in combination with the very stable output provided by our laser system renders this setup shot-noise limited, routinely reaching sensitivity levels in the μOD regime.[88] In comparison, VC typically shows a magnitude on the order of mOD (Figure 3.9b) which can be easily detected with our setup.

A typical result of an IVS experiment performed on chloroform ($CHCl_3$) recorded with a 10 fs near-IR pump pulse is illustrated in Figure 3.9b (left). The IVS map shows a temporal chirp highlighted by the pronounced curvature of the coherent artefact (CA) contribution due to the uncompressed probe pulse (∼300 fs duration).[89] In order to correct for the probe chirp, we select the central part of the CA and fit it to a Gaussian on a wavelength-by-wavelength basis. The obtained wavelength-dependent maximum is then used to interpolate all transients on a common time axis (Figure 3.9b, right).[85] This procedure allows us to exactly define the time delay at which pump and probe pulses

are overlapped in the sample (t_0). An alternative approach to determine the wavelength-dependent t_0 relies on the coherent oscillations observed after the CA. By measuring a solvent with a limited known number of modes, we can extract the phase of each oscillation for each wavelength and extrapolate back to the CA, where all oscillations have to start in-phase. We find that both methods agree to within 2 fs.

To illustrate how to extract the structural origin of the observed VC, we select a single transient at 590 nm (Figure 3.9c, top). We find strong CA contributions lasting for ∼150 fs after t_0, followed by regular and exponentially decaying oscillatory modulations lasting for >1 ps, encoding vibrational motion in the time domain. While the CA in theory contains all desired structural information, the combination of a short pump with a chirped probe pulse renders its shape too complicated to extract structural information.[44] We therefore restrict the analysis of the transient to a time delay >150 fs, to isolate exclusively impulsively generated VC contributions which can be Fourier transformed to yield the underlying frequency content. Prior to Fourier transformation, we apply a window-function to the residual VC to reduce Fourier ringing arising from the sharp cut-offs at the edges of the oscillation (Figure 3.9c, top, blue). A Kaiser-Bessel window[90] ($\beta = 2$) sufficiently reduces ringing, while largely preserving the corresponding lineshapes. In addition, we perform zero-padding to artificially increase the spectral resolution of the resulting spectrum, providing a smooth Fourier amplitude spectrum with correct peak frequencies.[88] The resulting Fourier amplitude spectrum for $CHCl_3$ exhibits modes over the full vibrational manifold (50-3000 cm^{-1}) identical to the ground-state Raman spectrum (Figure 3.9c, bottom).[91] We remark that it is necessary to sample the oscillations according to the Nyquist criterion to avoid frequency wrapping derived from undersampling.[92] Sampling ∼550-600 data points in steps of 2.8-3.5 fs leads to a good compromise between spectral shape, frequency space and acquisition time.

IVS beyond Solvents

In the previous section, we discussed the basic concepts of IVS and its application to an off-resonantly pumped and probed solvent. The wavelength-dependent Fourier amplitudes in this case turn out to be very sensitive to the employed pump, and in particular the probe shape, complicating an interpretation of the relative amplitudes.[83] In fact, the relative Fourier amplitudes of the

spectrum presented in Figure 3.9c do not match the Raman spectrum of $CHCl_3$. A way to obtain comparable Fourier intensities for ground-state molecules is to employ a resonant probe pulse. In that case, the probe pulse detects the VC on top of the ground-state absorption spectrum and the vibrational signal magnitudes experience amplification factors by up to 10^6, akin to resonance Raman (RR) spectroscopy.[40]

In a spectrally-resolved detection scheme, we have access to the wavelength-dependent intensity profile of the Fourier amplitudes similar to the information obtained in a RR excitation profile. The action of the impulsive pump pulse generates VC in all Raman-active modes, which in turn comprise the ground-state absorption spectrum. Wavepacket motion along these modes results in a spectral modulation of the absorption maximum for each mode and consequently results in a spectrally oscillating absorption spectrum (Figure 3.10a). This spectral oscillation is subsequently read out as an amplitude modulation for each wavelength pixel on the detector. In the ideal case of a Gaussian absorption profile, we expect little modulation near the ground-state absorption maximum, while the turning points to either side will show large amplitude variations as a function of pump-probe time delay. The corresponding Fourier amplitudes will therefore exhibit an absolute derivative shape of the ground-state absorption spectrum (Figure 3.10a, bottom).[66,93,94]

To illustrate the concepts above, we carry out off-resonant IVS on rhodopsin, showing a Gaussian-shaped ground-state absorption maximum at 498 nm (Figure 3.10b). After impulsive excitation with an 800 nm pump pulse (9 fs) and Fourier transformation, we retrieve the wavelength-dependent Fourier amplitude profile for rhodopsin. All modes show a node at 550 nm surrounded by local maxima at 510 nm and 590 nm in agreement with an absolute derivative shape of the underlying absorption spectrum. Closer examination reveals that the expected derivative shape is red-shifted from the ground-state absorption spectrum by ∼50 nm. This feature is explained by recalling that the impulsive pump pulse generates VC between at least two vibrational energy levels (Figure 3.10c). Consequently, the oscillating absorption spectrum will not be centred at the ground-state absorption maximum, but at a red-shifted value as the molecules are partially in an excited vibrational energy level. In rhodopsin, the largest contribution to this effect arises from the C=C stretching vibration at 1548 cm^{-1}. Due to the bandwidth (FWHM∼1600 cm^{-1}) of the impulsive pump pulse, most detected molecules will be predominantly in the first excited

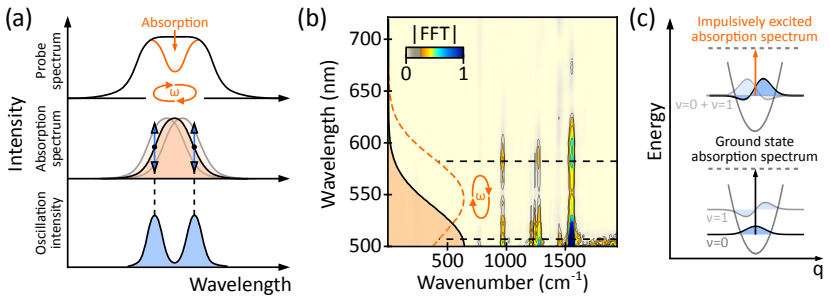

Figure 3.10: Ground-state absorption spectrum obtained with IVS. (a) Top: The probe spectrum (black) is reduced in intensity due to an overlaying molecular absorption spectrum (orange). Middle: The impulsive pump interaction with the sample leads to probe modulations which are imprinted on the absorption spectrum, leading to an oscillatory absorption spectrum. Note that the relative change of intensity is particularly large at the turning points of the absorption spectrum (blue arrows), while almost no modulation is observed in the centre. Bottom: Characteristic derivative-like wavelength-dependent intensity distribution of coherent oscillation due to a moving absorption spectrum. (b) Fourier transform amplitude map of rhodopsin impulsively excited at 800 nm (10 fs). We emphasise the derivative-shaped intensity distribution for each mode overlapping with a moving absorption spectrum which is red-shifted compared to the measured absorption spectrum. (c) Schematic illustration explaining the red-shifted absorption spectrum as a consequence of generating VC oscillating between ground and excited vibrational energy levels, thereby narrowing the energy gap between ground and excited electronic states.

vibrational state of the C=C stretching mode, yielding an impulsively generated absorption maximum at 543 nm in good agreement with the experimentally observed node at 550 nm (Figure 3.10b). The wavelength-resolved Fourier amplitudes can therefore be connected to the electronic state they originate from, which can provide a valuable route to distinguish overlapping vibrational signatures if resonant pumping conditions are employed.

IVS amplitudes for resonant probing conditions are related to RR intensities since the probe pulse is subject to the same cross sections. To quantitatively interpret IVS spectra, it is necessary to convert the obtained Fourier amplitudes into RR amplitudes. It turns out that a Fourier power spectrum compares best to a RR spectrum after time-resolution effects have been considered (see below).[88,95] IVS can thus be thought of as a time-domain variant of RR spectroscopy in the limit of off-resonant pumping and resonant probing.

Time-Resolution Effects in IVS

It is *a priori* surprising that we can observe VC over the full vibrational manifold employing a chirped probe pulse. In particular considering that the

effective time resolution, τ_{res}, of our setup can be approximated to first order as the convolution of two Gaussian pulses with temporal duration $\tau_{\text{pump}} = 10$ fs and $\tau_{\text{probe}} = 300$ fs according to

$$\begin{aligned}\tau_{\text{res}} &= \sqrt{\tau_{\text{pump}}^2 + \tau_{\text{probe}}^2} \\ &= \sqrt{10^2 + 300^2} \approx 300\,\text{fs}.\end{aligned} \tag{3.5}$$

This contradiction is resolved by the use of spectrally-resolved detection, which carries out a Fourier transformation of the transmitted probe, rendering the detection scheme non-time-resolved.[85,96,97] It can be shown that the actual pulse duration of the probe pulse in this scenario is replaced by its transform-limit (TL) as long as the spectral resolution of the employed spectrometer is high enough.[82] The actual effective τ_{res} becomes therefore pump pulse limited for a 1030 nm WL probe with a TL of 4 fs

$$\begin{aligned}\tau_{\text{res}} &= \sqrt{\tau_{\text{pump}}^2 + \text{TL}_{\text{probe}}^2} \\ &= \sqrt{10^2 + 4^2} \approx 10.8\,\text{fs}.\end{aligned} \tag{3.6}$$

To model the effect of a finite time resolution on an oscillation of frequency ω, we convolve the oscillation with a Gaussian function of full-width-half-maximum (FWHM) of τ_{res} (Figure 3.11a). By comparing the Fourier amplitudes of both oscillations, we can obtain a scaling factor to correct for a finite time resolution modelled by

$$S(\tau_{\text{res}}, \omega) = a\text{e}^{-b\tau_{\text{res}}^2\omega^2}, \tag{3.7}$$

with $a = 0.3$ and $b = 3.197 \cdot 10^{-9}\,\text{fs}^{-2}\,\text{cm}^2$. Equation 3.7 shows that the scaling factor drops drastically the higher the effective time resolution and frequency is, thus preventing the detection of high-frequency VC (Figure 3.11b).

The effective time resolution calculated in equation 3.6 has to be modified to account for pulse broadening[51] and spatio-temporal walk-off of pump and probe pulses in the sample.[95,98] Since we employ pump-probe crossing angles $<2°$, the spatial walk-off does not contribute. On the other hand, temporal walk-off may be significant, especially if the probe wavelength of interest differs significantly from the pump wavelength (Figure 3.11c). To account for the temporal walk-off we compute the wavelength-dependent GVD due to material dispersion with respect to the centre wavelength of the pump. This is extended in the case of a resonant pump pulse by multiplying the GVD square window

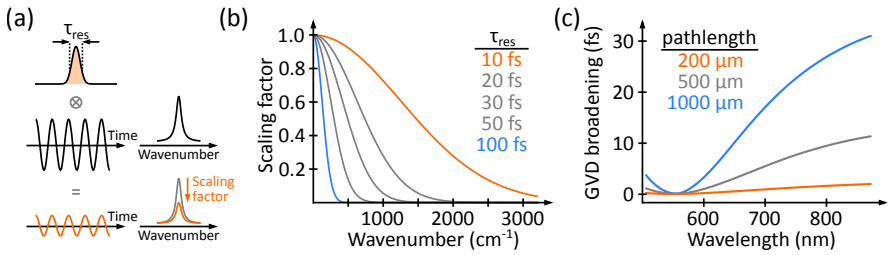

Figure 3.11: Effective time resolution in IVS. (a) To account for a finite time resolution in an IVS experiment, a wavelength-dependent scaling factor can be obtained considering a perfect oscillation convolved by a Gaussian function with a FWHM equal to the effective time resolution (τ_{res}) of the experiment. (b) Scaling factor deduced using the method described in (a) for various time resolutions. (c) Calculation of the effective time resolution as a function of probe wavelength due to group-velocity dispersion (GVD) for a 550 nm pump pulse (10 fs) as a function of flowcell pathlength. The calculation assumes a probe pulse duration of 4 fs.

by an exponential decay function to account for pump depletion. The final wavelength-dependent τ_{res} is then obtained as the FWHM of the convolution of the pump/probe cross correlation with the corresponding GVD window.[88,95,99]

It is crucial to employ very short pump pulses, yielding an effective $\tau_{res} \leq 15$ fs, to be able to observe the entire vibrational manifold while simultaneously ensuring high signal sensitivity. Furthermore, thin sample cells (≤ 500 μm) should be employed to reduce temporal broadening, and the impulsive pump pulse is best chosen to be close to the probe wavelength to avoid distortions in the wavelength-dependent amplitudes via GVD effects.[88,95]

Experimental Isolation of Excited-State Coherences

Up to this point, we have solely discussed the characterisation of IVS on the ground electronic state by employing off-resonant pump pulses. If the pump pulse is tuned into resonance, we generate excited electronic state VC on top of the electronic TA signal, since the excitation bandwidth for a <10 fs resonant pump pulse covers multiple vibrational energy levels on the excited electronic state.[100] In the context of the previous discussions, it comes as no surprise that resonant impulsive electronic excitation also generates ground-state and solvent VC. This is particularly problematic if excited and ground electronic states show overlapping absorption features, and when strongly scattering solvents have to be employed.

To isolate VC on the excited electronic state, we introduce an additional population-control pulse (dump pulse) that is temporally long and resonant only

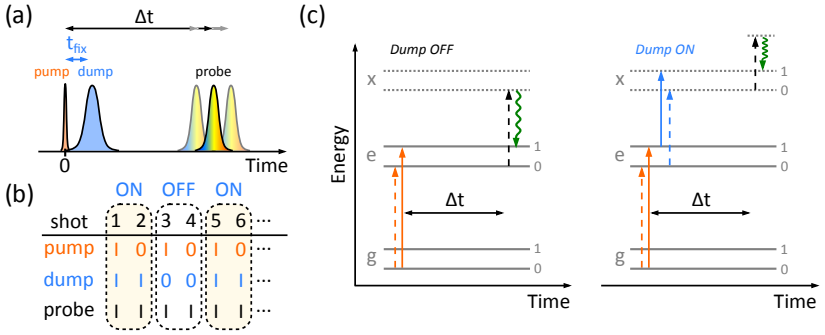

Figure 3.12: Isolation of excited-state vibrational coherence. (a) Pulse scheme employed in pump-dump-probe (PDP) IVS. The scheme is identical to a resonantly pumped IVS process, but includes an additional temporally long, narrowband dump pulse (>200 fs) specifically tuned into an excited-state resonance to vibrationally deactivate excited-state molecules. (b) Chopping scheme employed in PDP IVS leading to dumped (ON) and non-dumped (OFF) transient absorption spectra of the sample. (c) Selected WMEL diagrams depicting the pathways of a single molecule after interacting with pump (left) or pump and dump (right) pulses.

with an excited electronic state.[65,99] The dump pulse is placed ∼100 fs after the impulsive pump pulse in the pulse sequence (Figure 3.12a) and chopped at half the pump repetition rate (a quarter of the laser repetition rate) leading to spectra with (ON) and without (OFF) the dump pulse (Figure 3.12b). In the absence of the dump pulse, the pump pulse will generate excited electronic state VC which is read out by the probe as before. In the presence of the dump pulse, the selective resonance condition leads to a promotion of excited-state molecules to a higher lying (or lower lying) excited electronic state (Figure 3.12c). This results in a removed fraction of oscillating excited-state molecules, reducing the corresponding VC, while leaving the ground-state VC unaltered. It is important that the dump pulse is temporally long (>200 fs) to avoid further generation of VC, which can otherwise interfere with the excited-state vibrational signal. A direct subtraction of OFF and ON experiments of a sample in scattering solvent yields pure excited-state VC following from

$$\begin{aligned} \text{OFF} - \text{ON} &= (a\text{VC}_{S_0} + b\text{VC}_{S_1} + c\text{VC}_{solvent}) \\ &\quad - (a\text{VC}_{S_0} + (b-x)\text{VC}_{S_1} + c\text{VC}_{solvent}) \\ &= x\text{VC}_{S_1}. \end{aligned} \tag{3.8}$$

To illustrate the concept of pump-dump-probe (PDP) IVS, we investigate diphenyl-octatetraene (DPO), a prototypic system for the light-harvesting molecule β-carotene (Figure 3.13). DPO is a three-level system with a

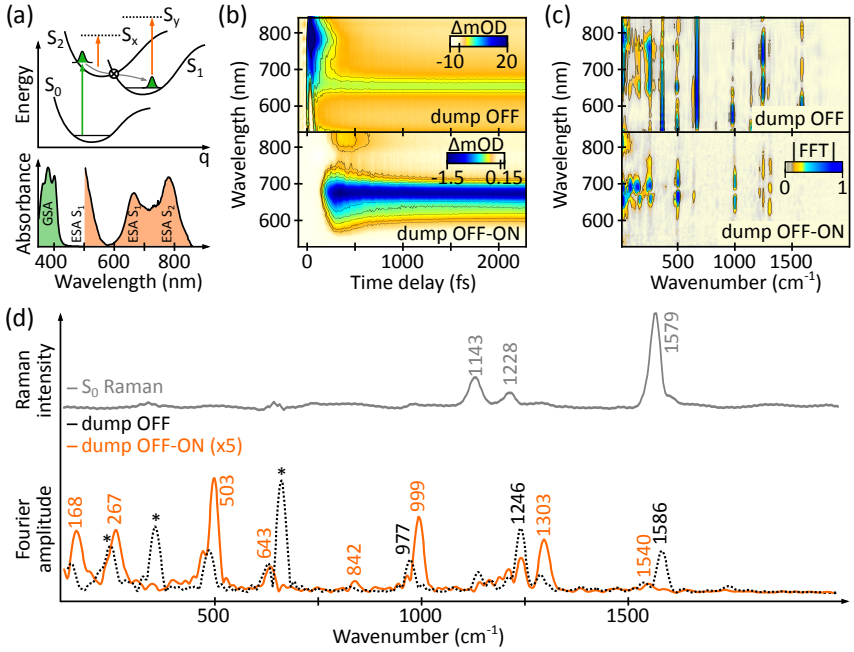

Figure 3.13: PDP IVS on diphenyl-octatetraene (DPO) in chloroform. (a) Energy level scheme indicating the main electronic transitions (green and orange arrows, top) and absorption features of ground (GSA) and excited electronic states (ESA, bottom). (b) Top: TA map after excitation centred at 390 nm (12 fs), bottom: Resulting difference map for dump OFF-ON using a dump pulse centred at 515 nm (200 fs). (c) Fourier transform amplitude map for dump OFF (top) and dump OFF-ON (bottom). (d) Spectral comparison between the ground-state Raman spectrum (grey, top) and selected IVS amplitude spectra (black - dump OFF, orange - dump OFF-ON). The ground-state Raman spectrum was provided by Torsten Wende.

symmetry-forbidden $S_1 \leftarrow S_0$ transition, an $S_2 \leftarrow S_0$ absorption maximum at 390 nm, and a conical intersection (CI) connecting S_2 and S_1.[101,102] Photoexcitation of DPO at 390 nm provides a TA spectrum characterised by three ESA bands in the visible centred at 790, 650 and 450 nm (Figure 3.13a). While the absorption features at 650 and 450 nm remain unchanged throughout the probed time delay, the band at 790 nm rapidly decays with a time constant of 80 fs, and is assigned to the $S_1 \leftarrow S_2$ internal conversion via a CI (Figure 3.13b, top). It was shown for β-carotene[99] that internal conversion occurring on such time scales efficiently transfers VC, making it an ideal candidate to explore PDP IVS.

We photoexcite DPO in $CHCl_3$ at 390 nm (12 fs) and employ a 515 nm dump pulse (200 fs) 120 fs after photoexcitation to selectively remove S_1 molecules. Subtraction of dump OFF and dump ON traces (Figure 3.13b, bottom) shows a strong negative signal at the S_1 ESA maximum at 650 nm, indicating that

predominantly S_1 molecules have been removed by the dump. To extract VC, we exclude the CA contributions and globally fit the remaining electronic signal (>150 fs) to a sum of exponentials

$$F(\lambda, t) = \sum_i a_i(\lambda) \mathrm{e}^{-\frac{t}{\tau_i}}, \tag{3.9}$$

with $a_i(\lambda)$ providing the decay-associated spectral amplitudes and τ_i the lifetimes of component i.[103,104] The vibrational information is subsequently obtained after subtraction of the electronic signal and Fourier transformation as outlined previously (Figure 3.13c).

In the absence of the dump pulse, the Fourier amplitude map is dominated by ground-state (1143, 1228, 1579 cm^{-1}) and solvent (263, 369, 669 cm^{-1}) contributions, which are non-resonantly probed and hence show no clear wavelength dependence (Figure 3.13c, top). In the subtracted Fourier amplitude map, however, all ground-state and solvent features are removed, leading to a clean wavelength dependence around the S_1 absorption maximum. This is more clearly illustrated by comparing a ground-state RR spectrum to a spectral average over the entire S_1 absorption region (600-750 nm, Figure 3.13d). The ground state is dominated by modes at 1143, 1228 and 1579 cm^{-1} present also in the IVS spectrum (dump OFF) with additional solvent modes dominating the spectrum. The subtracted spectrum, however, lacks all unwanted modes and reveals a clean S_1 spectrum with prominent modes at 168, 267, 503, 643, 842, 999, 1303 and 1540 cm^{-1}, generated after resonant impulsive photoexcitation into S_2 and VC transfer to S_1.

PDP IVS is an extension to IVS able to isolate background- and baseline-free VC of excited electronic states. We routinely aim to dump 20-30% of the excited-state population to ensure a linear operation regime. However, if higher dump pulse powers have to be employed, we observe dump-pulse perturbation of solvent and ground-state VC, which subsequently leads to a contamination of the dump OFF-ON spectra. In these cases, the best approach to obtain clean excited-state spectra is to record the solvent separately and perform a subtraction algorithm of the two subtracted spectra, as outlined below.[85,88]

3.2.3 IVS on Excited Electronic States

In the previous section we demonstrated a technique to isolate excited-state VC generated upon photoexcitation. In this case, the probability of VC generation

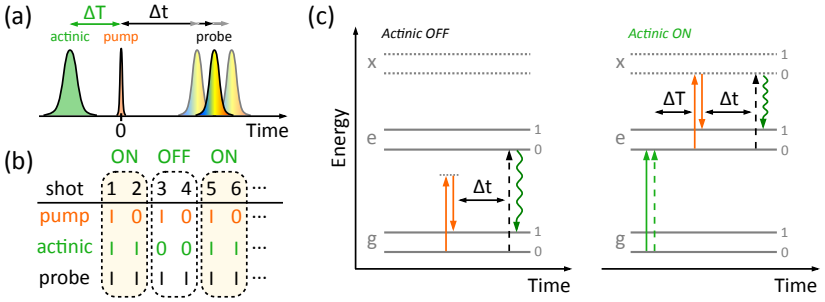

Figure 3.14: Direct generation of VC on excited electronic states. (a) Pulse scheme employed in actinic-pump-probe (APP) IVS. The scheme is identical to an off-resonantly pumped IVS process, but includes an additional temporally long, narrowband pump pulse to pre-excite a fraction of the molecules in the ensemble. (b) Chopping scheme employed in APP IVS leading to transient absorption spectra of the pumped (ON) and non-pumped (OFF) sample. (c) Selected WMEL diagrams depicting the pathways of a single molecule after interacting with pump (left) or pump and actinic (right) pulses.

is connected to the FC factors involved in the $S_e \leftarrow S_g$ transition and local potential energy surface features such as regions of high anharmonicity or conical intersections.[105,106] Consequently, the retrieved Raman spectrum might differ strongly from a Raman spectrum generated directly on the (vibrationally cold) excited electronic state. The latter is governed by the FC factors involved in the $S_x \leftarrow S_e$ transition and lacks all distortions described previously. Such an excited-state Raman spectrum can be obtained by combining IVS with an actinic pump pulse incident on the sample prior to the impulsive pump pulse (Figure 3.14a). The same chopping sequence as in PDP IVS is applied, leading to ON (actinic present) and OFF (actinic absent) IVS maps (Figure 3.14b). The actinic pump pulse prepares an excited-state population, which is subsequently investigated by an IVS pump-probe sequence to obtain a Raman spectrum of the excited electronic state at a given actinic-impulsive pump delay, ΔT. Importantly, the impulsive pump pulse is chosen to be resonant with an excited-state absorption to avoid VC generation via an $S_g \leftarrow S_e$ transition, while it is off-resonant with the ground-state absorption to prevent direct excitation via $S_e \leftarrow S_g$ (Figure 3.14c). This allows us to take advantage of resonance Raman enhancement, greatly improving the SNR. The approach consists of two experiments: (1) IVS reporting on the ground-state and solvent Raman modes, and (2) IVS on a mixture of excited and ground-state molecules

with vibrational contributions given by

$$\mathrm{OFF} = a_0 \mathrm{VC}_{S_0} + c_0 \mathrm{VC}_{solvent} \tag{3.10}$$

$$\mathrm{ON} = a_1 \mathrm{VC}_{S_0} + b_1 \mathrm{VC}_{S_1} + c_1 \mathrm{VC}_{solvent}. \tag{3.11}$$

The constants a and c vary between OFF and ON experiments, since actinic excitation changes the refractive index of the sample which leads to a different distribution of the number of impulsive pump photons over the various sample constituents. A straightforward experimental subtraction is therefore not possible. Employing an appropriate subtraction algorithm, however, can isolate the excited-state Raman spectrum[85] and therefore even allows us to obtain time-resolved structural information by varying the actinic-impulsive pump delay, ΔT. Briefly, the algorithm is based on a nonlinear Levenberg-Marquardt minimisation routine in the time domain with the real- and imaginary part of the corresponding Fourier transformation as feedback. First, a neat solvent trace has to be recorded, which is subtracted from both IVS maps (actinic OFF and ON) by selecting an isolated solvent mode as minimisation target. Subsequently, the OFF map is subtracted from the ON map using the full fingerprint frequency region as target.

To illustrate actinic-pump-probe (APP) IVS, we study the benchmark system *trans*-stilbene in n-hexane. Photoexcitation populates S_1 and internal conversion through a CI leads to isomerisation or backreversion to S_0. The excited electronic state shows a characteristic ESA at 590 nm with a lifetime of ∼70 ps (Figure 3.15a).[108] We photoexcite *trans*-stilbene at 320 nm (300 fs) and allow the system to undergo vibrational relaxation for 2 ps. Subsequently, we employ a 580 nm (10 fs) impulsive pump pulse and probe the system over the full ESA range. In the absence of the actinic pump pulse we observe mainly CA contributions with weak coherent oscillations arising mainly from the weak Raman scatterer n-hexane (Figure 3.15b, top). In the presence of the actinic pump, the impulsive pump pulse excites S_1 molecules to a short-lived higher lying excited electronic state leading to the appearance of a negative TA band at 590 nm (excited-state bleach), which shows pronounced oscillatory modulations (Figure 3.15b, top). After the removal of the electronic background, Fourier transformation reveals numerous modes with a well-defined wavelength dependence belonging to S_1, while almost no activity is found in the absence of the actinic pump pulse (Figure 3.15c). Comparing a spectral average from 520-640 nm shows S_1 modes at 286, 620, 846, 981, 1079, 1151, 1183, 1240,

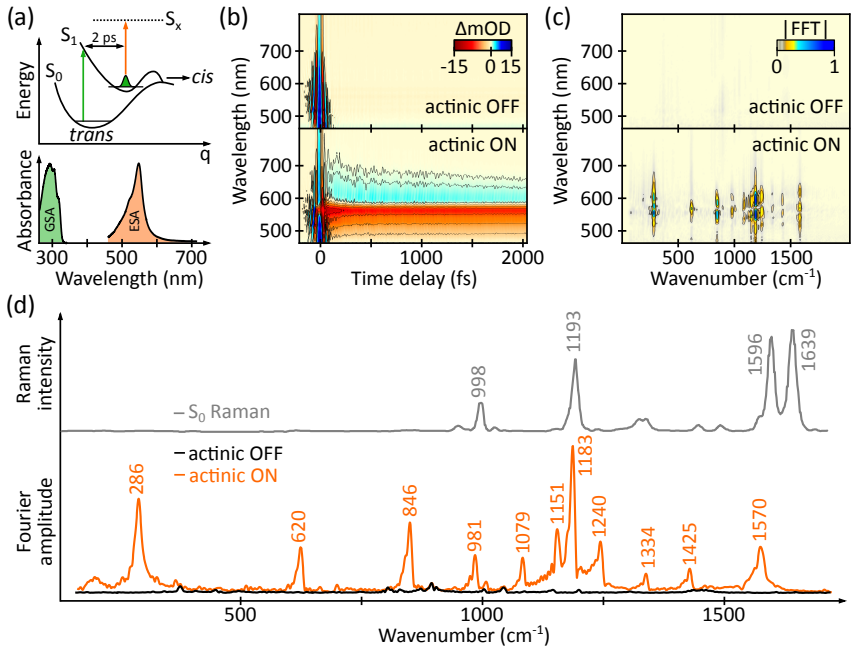

Figure 3.15: APP IVS on *trans*-stilbene in n-hexane. (a) Energy level scheme indicating the main electronic transitions (green and orange arrows, top) and absorption features of ground (GSA) and excited electronic states (ESA, bottom). (b) IVS maps using a visible impulsive pump pulse centred at 580 nm, 10 fs without (actinic OFF) and with (actinic ON) pre-excitation by the actinic pump pulse centred at 325 nm, 300 fs at ΔT=2 ps. (c) Extracted Fourier amplitude maps, respectively. (d) Ground-state Raman spectrum (grey) compared to Fourier amplitude spectra averaged from 520-640 nm for actinic OFF (black) and actinic ON (orange). Actinic OFF is displaying mainly n-hexane solvent modes, while actinic ON (orange) shows the appearance of excited-state modes distinctly different from ground-state modes. The ground-state Raman spectrum is reproduced with permission from: Dobryakov, A. L., Ioffe, I., Granovsky, A. A., Ernsting, N. P., Kovalenko, S. A. *J. Chem. Phys.* **137**, 244505 (2012), `http://dx.doi.org/10.1063/1.4769971`. Copyright 2012, AIP Publishing LLC.[107]

1334, 1425 and 1570 cm^{-1}, distinctly different from the ground-state Raman spectrum (Figure 3.15d). The obtained spectrum is in excellent agreement with previously published spectra obtained by femtosecond stimulated Raman spectroscopy (FSRS), validating this approach.[65,107,108]

In this context we want to point out that the acquisition of excited-state Raman spectra in the time domain holds a number of advantages over state-of-the-art frequency-domain methods like FSRS. Since APP IVS can record the full coherent evolution in the time domain, its spectral resolution is limited only by the natural dephasing time of the molecular vibration. For *trans*-stilbene we sampled the entire VC decay (5 ps) and obtained Raman linewidths of ~9 cm^{-1}

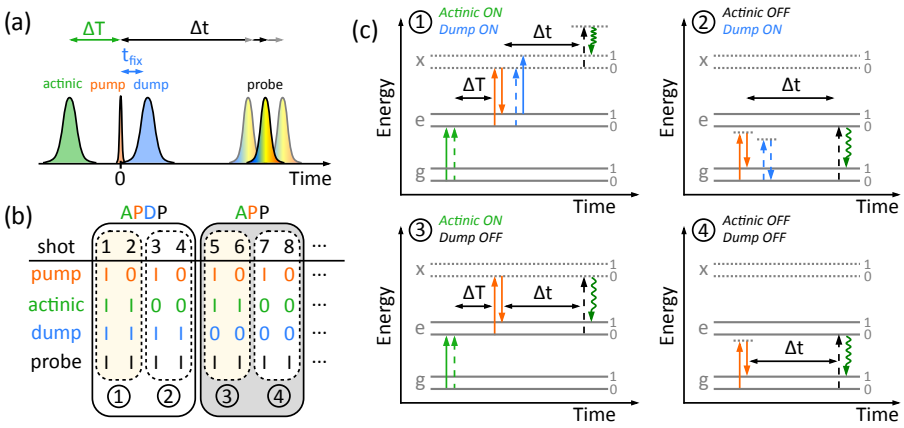

Figure 3.16: Concepts of PC-IVS. (a) Pulse sequence for PC-IVS consisting of an actinic excitation pulse followed by an impulsive pump pulse resonant only with the excited electronic state of interest, immediately followed by a long state-selective dump pulse as described for PDP IVS. The response of the system is subsequently investigated by a probe pulse. (b) Chopping scheme of PC-IVS. Letters on top are colour-coded to represent impulsive pump (P, orange), actinic pump (A, green), dump (D, blue) and probe (P, black) pulses. (c) Selected WMEL pathways describing the four major signals obtained in PC-IVS.

difficult to achieve using other methods. Additionally, baseline and lineshape problems arising from resonance enhancement, fluorescence and non-resonant contributions commonly complicating FSRS are avoided in APP IVS since these signals appear as slowly varying electronic background which can be easily removed in the time domain. APP IVS thus provides a valuable alternative to record baseline-free resonance Raman spectra in the time domain with high spectral resolution and SNR.

3.2.4 Population-Controlled IVS

A drawback of APP in condensed phases is the need to subtract ground-state and solvent contribution from the final spectrum, which can be very complicated depending on the experimental settings. We previously introduced PDP as a clean way of isolating excited-state VC. In the following, we combine APP with an additional narrowband dump pulse (>200 fs, APDP) after the impulsive pump has interacted with the sample (Figure 3.16), to extract baseline- and background-free excited-state Raman spectra in the time domain (Figure 3.16a).[65] The chopping scheme for this four-pulse experiment is an extension of APP IVS with the dump pulse being chopped at one eighth of the laser repetition rate (Figure 3.16b). Since this experiment employs an

actinic pump pulse to populate the excited electronic state and a dump pulse to alter the excited-state population, we term the technique population-controlled IVS (PC-IVS). Overall, PC-IVS requires an actinic pump pulse resonant with the ground-state absorption spectrum, an impulsive pump pulse off-resonant with the ground-state absorption and a temporally long dump pulse (>200 fs) selectively resonant only with the excited electronic state. As a consequence of the chopping scheme we obtain four IVS maps (Figure 3.16c):

(4) The absence of actinic and dump pulses leads to an off-resonantly pumped IVS map reporting on S_g and solvent VC, as discussed in IVS.

(3) The actinic pump pulse excites a subset of molecules to S_e followed after a time delay, ΔT, by the impulsive pump pulse generating VC on S_e, S_g and solvent. The scheme provides baseline-free but not background-free excited-state VC as discussed in APP IVS.

(2) The addition of a dump pulse to (4) leads to an off-resonantly pumped IVS map reporting on S_g and solvent VC which is perturbed by the electric field of the dump pulse. The scheme reduces to (4) if a weak-field dump pulse is employed which does not affect the impulsively generated VC.

(1) The actinic pump pulse excites molecules to S_e followed after a time delay, ΔT, by the impulsive pump pulse generating VC on S_e, S_g and solvent. Subsequently, the dump pulse removes a fraction of molecules from the excited electronic state leading to a reduction of the probed excited-state VC, while preserving S_g and solvent VC. The process is similar to PDP but the role of the resonant impulsive pump pulse is split into an actinic pump pulse (photoexcitation) and an off-resonant impulsive pump pulse (VC generation) to recover time-resolved excited-state Raman spectra.

The scheme can be summarised in terms of the corresponding VC contributions:

$$\mathrm{VC}_{(4)} = a_0\mathrm{VC}_{S_0} + c_0\mathrm{VC}_{solvent} \tag{3.12}$$

$$\mathrm{VC}_{(3)} = a_1\mathrm{VC}_{S_0} + b_1\mathrm{VC}_{S_1} + c_1\mathrm{VC}_{solvent} \tag{3.13}$$

$$\mathrm{VC}_{(2)} = a_0\mathrm{VC}_{S_0} + c_0\mathrm{VC}_{solvent} \tag{3.14}$$

$$\mathrm{VC}_{(1)} = a_1\mathrm{VC}_{S_0} + (b_1 - x)\mathrm{VC}_{S_1} + c_1\mathrm{VC}_{solvent}. \tag{3.15}$$

The aim of this approach is to compute the difference in pathways (3) and (1) in exactly the same way as for PDP. This can then be compared to (4)-(2) to test for potential artefacts ('leakage') introduced to the ground-state VC which would reappear in (3)-(1):

$$\begin{aligned} \mathrm{VC}_{(4)} - \mathrm{VC}_{(2)} &= (a_0\mathrm{VC}_{S_0} + c_0\mathrm{VC}_{solvent}) - (a_0\mathrm{VC}_{S_0} + c_0\mathrm{VC}_{solvent}) \\ &= 0 \end{aligned} \tag{3.16}$$

$$\begin{aligned} \mathrm{VC}_{(3)} - \mathrm{VC}_{(1)} &= (a_1\mathrm{VC}_{S_0} + b_1\mathrm{VC}_{S_1} + c_1\mathrm{VC}_{solvent}) \\ &\quad - (a_1\mathrm{VC}_{S_0} + (b_1 - x)\mathrm{VC}_{S_1} + c_1\mathrm{VC}_{solvent}) \\ &= x\mathrm{VC}_{S_1}. \end{aligned} \tag{3.17}$$

We remark that is important to temporally separate dump and impulsive pump pulses to avoid corruption of the signals by dumping a fraction of excited-state molecules before the impulsive pump interaction is complete.

To demonstrate the capabilities of PC-IVS, we investigate all-*trans* n-butyl retinal protonated Schiff base (nBu-RPSB) in methanol. nBu-RPSB shows an absorption maximum at 445 nm ($S_1 \leftarrow S_0$) and undergoes a photoisomerisation reaction within ∼5 ps after photoexcitation.[109] The transient absorption spectrum of the excited electronic state is characterised by a broad SE band covering almost the entire visible region, overlaid by a weaker ESA at 750 nm, leading to a double-humped TA shape (Figure 3.17a). We performed PC-IVS with a 400 nm (25 fs) actinic pump pulse followed after 60 fs by a visible 590 nm (11 fs) impulsive pump and a 1030 nm (200 fs) dump pulse, both resonant with the SE. After removal of the electronic dynamics in all IVS maps, we carry out a Fourier transformation to extract the underlying frequency contents (Figure 3.17b). The Fourier amplitude maps of (4) and (2) are dominated by ground-state and solvent modes as expected in the absence of the actinic pump. The negligible difference in these maps further suggests little perturbation effects of the dump pulse. Fourier maps (3) and (1) also appear similar but, on closer inspection, show differences in particular in the low-frequency region and around 1000 cm^{-1}. Since these maps are recorded with the actinic pump pulse present, the comparison to (4) and (2) indicates the presence of excited-state modes.

This comparison is made clearer by computing the difference between corresponding maps in the presence and absence of the dump pulse, i.e. (3)-(1) and (4)-(2). We observe intense Fourier modes around 1000 cm^{-1} and in the low

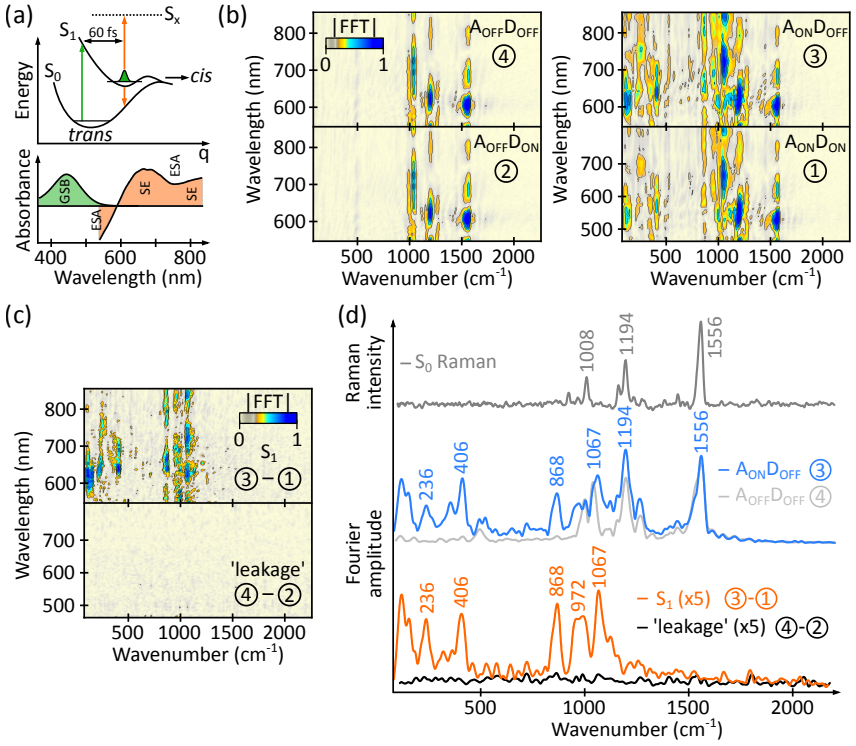

Figure 3.17: PC-IVS on all-*trans* n-butyl retinal protonated Schiff base (RPSB) in methanol. (a) Energy level scheme (top) and absorption features of nBu-RPSB in methanol solution (bottom). (b) Fourier transform maps obtained for the processes illustrated in Figure 3.16c, after excitation with a 400 nm actinic pump pulse (A, 25 fs) and impulsive excitation at 590 nm (11 fs) at $\Delta T = 60$ fs. The dump was tuned into resonance with the SE feature at 1030 nm (D, 200 fs). (c) Fourier transform maps obtained after subtracting dump ON and dump OFF traces while the actinic pump pulse was ON (top) or OFF (bottom). (d) Spectral comparison of selected traces averaged from 600-800 nm to the resonance Raman spectrum of the ground electronic state, demonstrating clean subtraction of ground and solvent features in PC-IVS. The ground state Raman spectrum was provided by Torsten Wende.

frequency region centred around the SE region (Figure 3.17c). The wavelength dependence of the Fourier amplitudes is not as clear as in the previous examples due to the broad spectral nature with overlapping excited-state features, but nevertheless fits with an assignment to S_1. In comparison, the ④-② Fourier amplitude map shows no modes leaking in through the dump electric field, thereby rendering this experiment background- and baseline-free. A spectral comparison of the RR spectrum with the obtained spectra demonstrates that the background subtraction carried out by the dump is excellent. While the ground state exhibits dominant modes at 1008, 1194 and 1556 cm^{-1}, which are reproduced by the off-resonant IVS experiment ④ and still present after actinic excitation ③, the subtracted spectrum ③-① displays a completely

new set of frequencies. In particular the activity around 1000 cm^{-1} is reporting on the twisted nature of the molecule in S_1 crucial for the photoisomerisation process.

In summary, PC-IVS can provide baseline- and background-free Raman spectra of excited electronic states with excellent SNR and straightforward extension of a TA setup.[65] We note that PC-IVS, in comparison to APP, is applicable independently of the nature of the excited-state resonance, rendering it a more universal tool. However, the dumping process reduces the number of detected molecules and relies on a subtraction between two intrinsically small numbers, requiring high sensitivity. In comparison, APP provides roughly an order of magnitude more signal, simplifying detection, but cannot be applied if the impulsive pump pulse is resonant with a SE of the excited electronic state. An additional advantage of APP is that VC is not perturbed by the presence of the dump electric field as in PC-IVS, which can introduce ground-state or solvent peaks in the experimental subtraction. In an independent measurement on neat toluene (actinic: 450 nm (300 fs, 160 nJ), impulsive: 800 nm (9 fs,180 nJ), dump: 1030 nm (200 fs, 250 nJ)), we determined the solvent extinction factor to be on the order of 10^3, which has to be kept in mind when designing experimental conditions for PC-IVS. Regardless, both techniques allow us to record time-resolved excited-state Raman spectra, making it possible to follow chemical reactions in real time on a structural level. In addition, both techniques can in principle utilise a short <15 fs actinic pump pulse to obtain a time resolution of 20 fs along ΔT. Employing a short excitation pulse leads to VC generation on the excited electronic state, which is then probed with the IVS sequence, resulting in modulations of the excited-state Raman spectrum as a function of ΔT. These oscillations can also be Fourier transformed, providing a second frequency axis leading to a 2D Raman map, in analogy to 2D-FSRS,[110,111] discussed in chapter 7 and 8.

Chapter 4

Mode-Specific Photoisomerisation in Rhodopsin

The following chapter is adapted with permission from C. Schnedermann, M. Liebel and P. Kukura, *J. Am. Chem. Soc.*, 2015, **137**, 2886-91. Copyright 2015 American Chemical Society.[95] Rhodopsin samples were provided by Katelyn M. Spillane and Giovanni Bassolino.

4.1 Introduction

Photoisomerisation reactions are ideally suited to study the origins of fast and efficient photochemistry.[107,109,112–115] Absorption of a photon causes electronic excitation and provides molecules with excess energy, which is converted into atomic motion to drive the reaction.[116–120] A classic example is the 11-*cis* to all-*trans* photoisomerisation of the retinal chromophore in rhodopsin, marking the first step in vision.[121–123] Recently, ultrafast transient absorption spectroscopy provided evidence for the involvement of a conical intersection (CI) in this reaction,[10] also demonstrated in biomimetic photoswitches.[124] Theoretical studies have proposed backbone torsion, pyramidalisation and hydrogen out-of-plane motions to be crucially involved in the mechanism, but little information exists on the identity of the nuclear degrees of freedom that contribute to the formation of the CI.[122,123,125–128]

To illustrate the dynamic evolution of a system in a photochemical reaction mediated by a CI, it is instructive to consider a simplified potential energy diagram (Figure 4.1). Following population of the first excited electronic state,

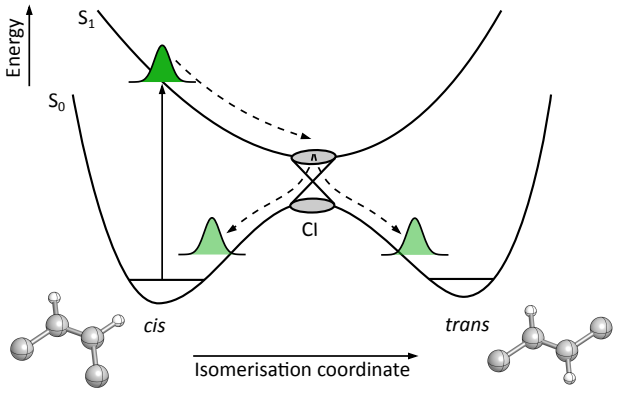

Figure 4.1: Schematic potential energy diagram for a *cis* to *trans* photoisomerisation mediated by a conical intersection (CI). Excited molecules rapidly leave the Franck-Condon region towards the CI mediating internal conversion to the ground-state potential. The overall reaction leads to the formation of photoproduct (*trans*) and backreversion to the reactant (*cis*).

the system quickly evolves out of the Franck-Condon (FC) region towards the CI, where internal conversion to the ground-state potential energy surface takes place, leading to the photoinduced formation of photoproduct and reactant.[129] The kinetics of such photoreactions are often studied by time-resolved transient absorption spectroscopy.[8,10,112,129] A short resonant pump pulse photoexcites the molecule and is followed by a probe pulse, which records a transient absorption spectrum at various time delays after the pump pulse. By using a short pump pulse (∼10 fs), the excitation process additionally generates vibrational coherence (VC) in all FC-active modes.[99] The resulting wavepacket motion modulates the transient absorption signal, thus providing vibrational information in addition to the electronic dynamics.[85,99] Such wavepacket motion can be highly affected by passage through a CI depending on the involvement of the underlying degree of freedom in the CI,[105,106] implying that monitoring VC after internal conversion could provide detailed information on the structure of the CI.

We have recently demonstrated that internal conversion through a CI is vibrationally coherent.[99] In the case of the $S_2 \leftarrow S_1$ transition in β-carotene, we observed strong similarities between the Raman spectrum derived from VC passing through the CI and the Raman spectrum of the S_1 product state, with some weak modes in the fingerprint region enhanced upon internal conversion. In the case of rhodopsin, such an experimental approach uncovered a dominant low-frequency torsional mode after internal conversion assigned to the primary

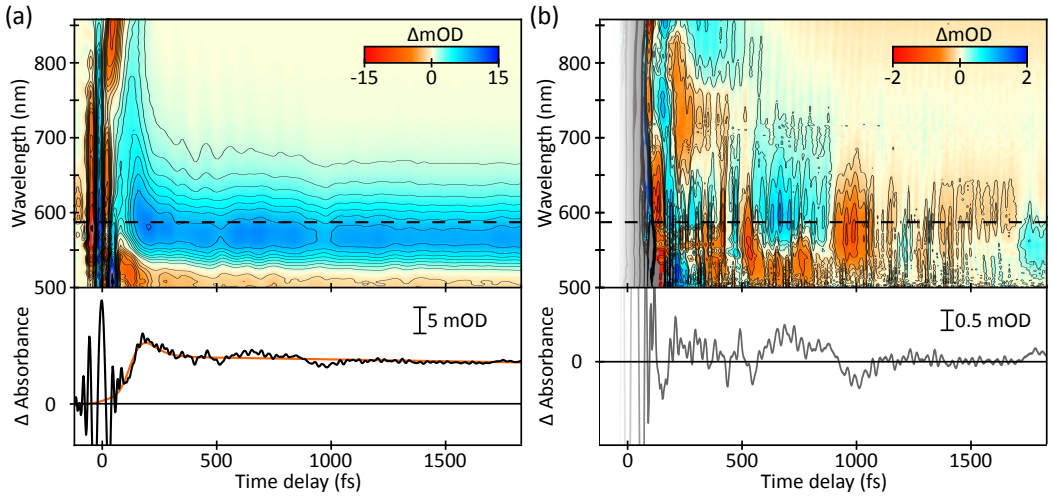

Figure 4.2: Transient electronic and vibrational signatures after photoexcitation of rhodopsin with an 8 fs pulse. (a) Differential absorbance exhibiting a coherent artefact at early time delays and the appearance of photoproduct absorption at 560 nm. The transient at 587 nm illustrates the growth of the photoinduced absorption within 200 fs and is shown together with the corresponding fit to the electronic kinetics (orange). (b) After subtraction of the electronic response by global fitting, the underlying vibrational coherence becomes visible, shown for the transient at 587 nm. Early time points dominated by the coherent artefact have been shaded for clarity as they are not included in further analysis.

photoproduct bathorhodopsin.[8] The employed pump pulses, however, remained too long and the spectroscopic sensitivity too low to reveal the fate of higher frequency modes suggested by theory to be significant contributors to the photoisomerisation. A detailed understanding of the CI region and the factors connecting chemical reactivity and efficiency on an atomic level is therefore still missing.

4.2 Results and Discussion

We performed transient absorption spectroscopy of rhodopsin with an unprecedented combination of time resolution (∼10 fs), detection bandwidth (500-900 nm) and spectroscopic sensitivity (∼10 μOD). In particular the high spectroscopic sensitivity is a critical advance over previous studies and allows us to reveal nuclear coherences over the full vibrational manifold that cause small oscillatory features on top of the transient absorption spectra. The corresponding differential absorbance map after photoexcitation with an 8 fs pulse centred at 500 nm is shown in Figure 4.2a. Around zero time delay,

we observe a coherent artefact followed by a rapidly red-shifting stimulated emission band initially appearing at 800 nm. After leaving the probe window in the near-IR, the stimulated emission converts into a photoinduced absorption signal, which blue-shifts to its final maximum at 560 nm indicating formation of bathorhodopsin within 200 fs.[8,10] Longer time delays (>200 fs) exhibit a stationary transient absorption spectrum with overlapping signatures of ground-state bleach (498 nm) and bathorhodopsin absorption (560 nm). Individual transients such as that shown at 587 nm furthermore reveal large oscillatory modulations of the electronic signal caused by the generation of vibrational wavepackets upon photoexcitation.

We are able to extract the residual VC as a function of the probe wavelength (Figure 4.2b) by globally fitting the electronic dynamics of the transient absorbance map, as indicated for a transient at 587 nm (Figure 4.2a). Here, we opted for a model describing the entire transient absorbance map to capture even the earliest dynamic events by using a sum of three exponentially-modified Gaussian functions with a common rise time, σ, given by

$$\begin{aligned} F(\lambda,t) &= \mathrm{e}^{-\frac{(t-t_0)^2}{2\sigma^2}} \otimes \sum_i a_i(\lambda)\mathrm{e}^{-\frac{t}{\tau_i}} \\ &= \sum_i a_i(\lambda)\mathrm{e}^{\frac{\sigma^2}{2\tau_i^2}-\frac{(t-t_0)}{\tau_i}}\,\mathrm{erfc}\left(\frac{\sigma}{\sqrt{2}\tau_i}-\frac{(t-t_0)}{\sqrt{2}\sigma}\right). \end{aligned} \tag{4.1}$$

The coherent oscillations (Figure 4.2b) are most pronounced in the 500-650 nm window, with a node near the bathorhodopsin absorption maximum at 560 nm,[85] and contain both high- and low-frequency components lasting for more than 1.5 ps. Probe wavelengths >700 nm, however, exhibit only very short-lived coherence activity. Wavelength-dependent Fourier transformation of the residual coherences reveals the spectral intensity distributions of all vibrational modes up to 1800 cm^{-1} (Figure 4.3a). We find pronounced activity in the torsional (<500 cm^{-1}), hydrogen out-of-plane (HOOP, 800-1100 cm^{-1}), C-C stretching (1150-1350 cm^{-1}) and the C=C stretching (1500-1650 cm^{-1}) regions. Additionally, the overall wavelength dependence of the Fourier intensities closely resembles the absorption spectra of rhodopsin and bathorhodopsin, with maxima at 500 nm and 580 nm, respectively.

To rationalise the molecular origin of the VC in the bathorhodopsin absorption window, we compare an averaged Fourier power spectrum (570-640 nm) with the resonance Raman (RR) spectrum of bathorhodopsin (Figure 4.3b).

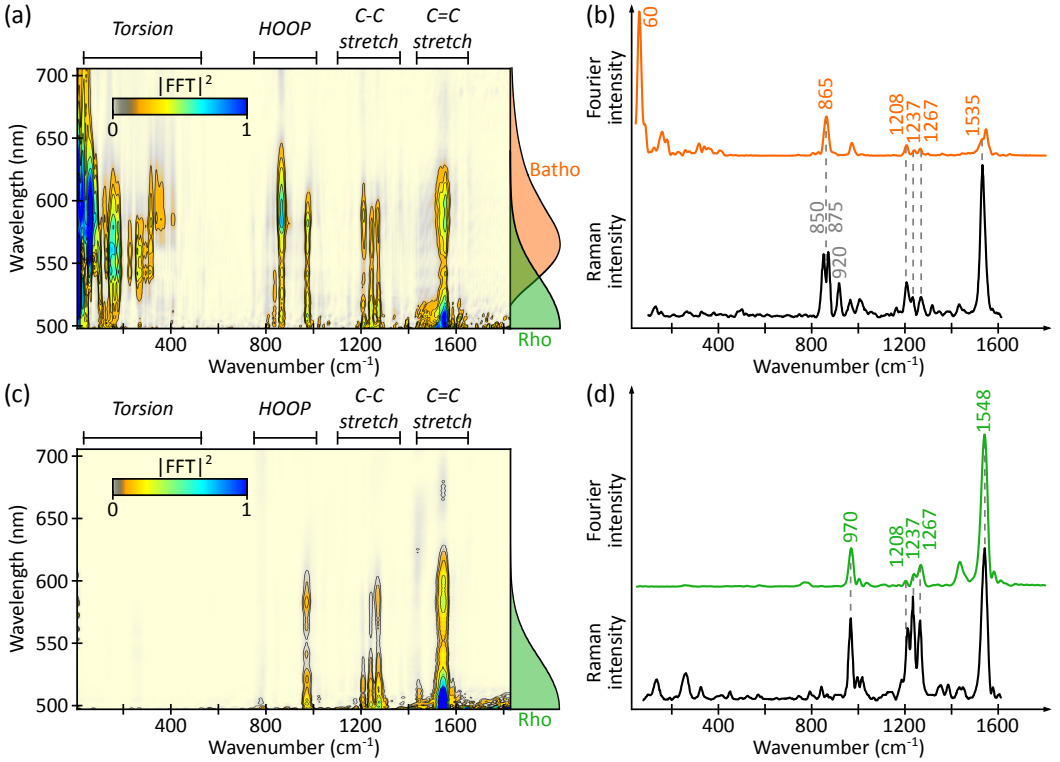

Figure 4.3: Fourier transform power maps and spectra compared to resonance Raman. (a) Fourier power map following resonant excitation with an 8 fs pump pulse centred at 500 nm and (b) resonance Raman spectrum (black) compared to a spectral average from 570-640 nm for bathorhodopsin (orange). (c) Fourier power map following off-resonant excitation with a 9 fs pulse centred at 800 nm and (d) resonance Raman spectrum (black) compared to a spectral average from 570-640 nm for rhodopsin (green). The pump-probe data have been scaled to correct for amplitude effects caused by finite time resolutions. Resonance Raman spectra are adapted with permission from Lin *et al* (488 nm),[130] copyright 1998 American Chemical Society and Kukura *et al* (805 nm),[131] copyright 2005 American Association for the Advancement of Science. We remark in this context that the resonance Raman spectrum of rhodopsin and bathorhodopsin is largely invariant to a change in the excitation wavelength.[130–132] Absorption spectra for rhodopsin (Rho, green) and bathorhodopsin (Batho, orange) are indicated on the side of (a) and (c), respectively. Time-domain power spectra were obtained by Fourier transformation of the residual coherence map for time delays greater than 80 fs.

We chose the 570-640 nm window specifically due to the known dependence of the coherent amplitudes on the shape of the underlying absorption spectrum (Figure 4.3a).[133] In the high-frequency region (>1000 cm^{-1}) we find signatures of bathorhodopsin C-C stretching modes at 1208, 1237 and 1267 cm^{-1} with matching relative intensity distributions, as well as a shoulder at 1535 cm^{-1} assigned to the C=C stretching mode in bathorhodopsin, albeit with decreased

relative intensity. The low-frequency torsional region shows enhanced activity compared to the RR spectrum, with a pronounced mode at 60 cm^{-1}, previously shown to originate from coherently excited bathorhodopsin.[8] The HOOP region is dominated by an intense mode at 865 cm^{-1}, which we attribute to the unresolved C_{10}-H and C_{12}-H HOOPs at 850 and 875 cm^{-1}, respectively. We furthermore note the distinct lack of coherence activity in the C_{11}-H HOOP at 920 cm^{-1}.

Resonant excitation by a short pump pulse generates coherent wavepacket motion on both ground and excited electronic states,[134] complicating the interpretation of the VC. It is thus necessary to record a pure ground-state time-domain spectrum which can be achieved in an off-resonant pump-probe experiment. Keeping the probe pulse unchanged and using a 9 fs pump pulse centred at 800 nm, we completely avoid photoexcitation and only generate wavepacket motion on the ground electronic state of rhodopsin.[47,48] The resulting Fourier power map (Figure 4.3c) exhibits coherence activity in the HOOP, C-C stretch and C=C stretch regions but lacks all intensity in the torsional region of the spectrum. The overall wavelength dependence of the coherence activity is shifted towards the shorter wavelength region compared to the resonant experiment, now closely resembling the absorption spectrum of rhodopsin. The Fourier power spectrum averaged over the same probe window (570-640 nm), as for the resonant experiment, exhibits a HOOP mode at 970 cm^{-1}, three C-C stretches at 1208, 1237 and 1267 cm^{-1} and an intense C=C stretch at 1548 cm^{-1}, in excellent agreement with the ground-state RR spectra of rhodopsin.[130,131]

The coherence activity obtained in the off-resonant experiment is related to the RR intensities, as shown by the similarity to the RR spectrum of rhodopsin in Figure 4.3d. Resonant probing ensures proportionality to the RR cross sections, yielding comparable intensities to a RR spectrum.[133] The use of a short resonant pump pulse, will generate wavepackets in all FC-active modes on the excited electronic state. After preparation, these wavepackets will rapidly evolve out of the FC region and through the CI before they arrive on the photoproduct potential energy surface. For a fully coherent reaction, a resonantly probed photoproduct spectrum would equal the corresponding RR spectrum, for the same reasons as in the off-resonant case.

This allows us to assign which modes in Figure 4.3a,b correspond to bathorhodopsin and which to rhodopsin coherences. In the low-frequency

region, no coherence activity can be detected in the off-resonant experiment (Figure 4.3c), while resonant excitation leads to very strong coherence activity centred around the absorption maximum of bathorhodopsin. These modes must hence originate from (vibrationally hot) bathorhodopsin. An examples is the intense mode at 865 cm^{-1}, which does not appear in the off-resonant experiment and is a clear marker mode of bathorhodopsin.[130,131] Its wavelength-dependent coherence activity is also centred around the absorption maximum of bathorhodopsin. We furthermore attribute the shoulder appearing at 1535 cm^{-1} to the C=C stretch of the photoproduct because the off-resonant experiment does not show such a characteristic signature. The C-C stretch region is difficult to assign due to the mutual Raman signatures of reactant and product (compare Figure 4.3b, d). However, resonant excitation significantly shifts the wavelength-dependent coherence activities towards the bathorhodopsin absorption spectrum, while the reactant shows most activity near the absorption maximum of rhodopsin. The spectral average displayed in Figure 4.3b additionally ranks the intensities in order of: 1208>1237>1267 cm^{-1}, while the opposite is found in Figure 4.3d, suggesting that, despite overlap, we observe VC in ground-state bathorhodopsin modes. We therefore assign all modes in the resonant spectrum to bathorhodopsin with the exception of the modes at 970 and 1548 cm^{-1}.

CIs are theoretically predicted to affect wavepacket propagation significantly depending on the type of involvement in the formation of the CI.[105,106] Passage through a CI should therefore lead to a change of the vibrational coherence activity in a pump-probe experiment. In the case of rhodopsin, differences between the coherence activity after internal conversion and the RR spectrum of bathorhodopsin therefore provide information on the CI geometry. Theoretical studies have categorised the vibrational degrees of freedom involved in the formation of a CI into tuning and coupling modes.[105,106] Tuning modes are required to reach the CI energetically by reducing the energy gap between the involved electronic states, whereas coupling modes are active in forming the CI. Based on this description, wavepackets in tuning modes are expected to be largely unaffected by the internal conversion event, while coupling mode wavepackets will be strongly influenced.

Comparison of the RR and Fourier spectra of bathorhodopsin allows us to divide the Raman-active modes into three categories: those that are strongly

enhanced (<500 cm^{-1}), those that exhibit expected relative intensities (500-1600 cm^{-1}) and those that are unexpectedly weak (920 cm^{-1}). Figure 4.4a illustrates the dynamic evolution of vibrational wavepackets in a coupling mode in the vicinity of a CI.[105,106] Photoexcitation of a molecular ensemble by a short pump pulse generates wavepackets on the excited electronic state, which initially evolve in-phase. Upon encountering the CI, a fraction of the excited molecules internally converts,[135] leading to wavepackets oscillating on the photoproduct potential. The wavepackets in the remaining molecules on the excited electronic state revisit the CI half a vibrational period later, again forming photoproduct wavepackets after internal conversion. The successively arriving photoproduct wavepackets are therefore necessarily out-of-phase with each other, provided the vibrational period is shorter than the excited-state lifetime. The signal recorded in an ensemble measurement will hence be diminished due to destructive interference. Coherence activity in coupling modes can be further reduced in intensity due to their high anharmonic character near the CI, which leads to a delocalisation of the vibrational wavepacket, as pointed out by Kühl *et al.*[105] We remark that an alternative explanation based on a phase-dependent CI space may be equally valid.[136] Which model is ultimately responsible for the lack of coherence activity in the C_{11}-H mode will require further detailed quantum-chemical calculations, guided by the experimental results reported here.

Vibrational wavepackets in tuning modes, on the other hand, are not strongly affected by such a phase relationship (Figure 4.4b).[105,106] In rhodopsin, the isomerisation is volume-conserving and spatially localised. The involved reactant and photoproduct potentials are therefore not significantly displaced, giving rise to coherence activities comparable to the RR spectrum. Minor deviations from the expected RR intensities in such modes can, however, be rationalised by considering a small change in the potential energy surface upon internal conversion. If the photoisomerisation proceeds with a change of frequency or displacement along a tuning mode, then internal conversion will project wavepackets on a slightly steeper or shallower part of the photoproduct surface. This results in a small perturbation in the wavepacket dynamics causing minor intensity deviations compared to the RR spectrum due to partially destructive interference. These effects are particularly small for the photoisomerisation in rhodopsin, since the volume-conserving nature of the reaction

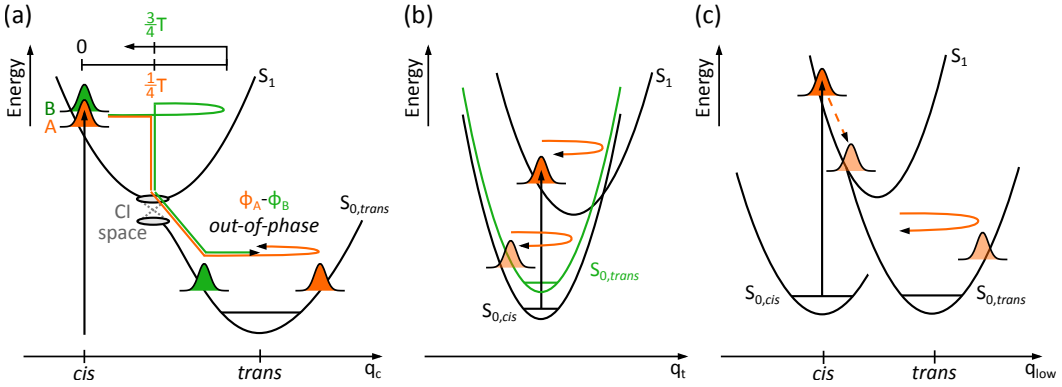

Figure 4.4: Schematic representation of wavepacket dynamics. (a) Coupling modes: Upon encountering the CI, a fraction of the excited molecules internally converts, forming wavepackets on the photoproduct *trans* potential energy surface (A, orange). Remaining excited-state wavepackets (B, green) cross to the *trans* surface half a vibrational period (T) later, resulting in out-of-phase wavepacket motion and hence destructive interference due to the accumulated phase difference $\phi_A - \phi_B$. The coherence activity is drastically decreased compared to a RR spectrum. We remark that the CI space contains a multitude of CIs with different geometries, one of which has been chosen to represent the behaviour of wavepackets in coupling modes. (b) Tuning modes: Vibrational wavepackets created in the excited electronic state will reduce the energy gap between the involved electronic states, leading to internal conversion. These modes are not part of the CI space and are thus unaffected by the crossing. Wavepackets will, after change of the electronic state, simply continue to oscillate in the new potential, resulting in coherence activities similar to RR. (c) Low-frequency modes: Large initial displacements on the excited electronic state lead to high accumulated momentum which is transferred to the photoproduct potential giving rise to large coherence activity observed in the photoproduct. Note that q_{low} refers to photoproduct normal coordinates rather than the reaction coordinate itself, which is a complex combination of the above.

leaves most modes unchanged, as apparent by the overall similarity of C-C and C=C stretching region in the RR spectra of rhodopsin and bathorhodopsin.[10]

Finally, the low-frequency region of the time-domain spectrum is characterised by a number of very intense modes including the previously reported bathorhodopsin mode at 60 cm^{-1}. Theoretical simulations[122,125] and RR intensity analysis[137] show that low-frequency modes experience a steep slope on the excited-state potential energy surface, leading to fast relaxation particularly along these coordinates. For vibrational modes such as the backbone torsion at 60 cm^{-1}, corresponding to a 555 fs vibrational period, the short excited-state lifetime (50-100 fs) necessarily implies only minimal structural evolution along that coordinate on the excited electronic state. Since the overall isomerisation reaction requires a large localised torsional rearrangement, the rapid internal

conversion projects wavepackets in these modes on a very steep part of the photoproduct potential energy surface. This leads to enhanced nuclear motion and results in pronounced coherence activity (Figure 4.4c). Such a behaviour does not, however, exclude significant twisting along the C_{11}=C_{12} dihedral coordinate, as predicted by quantum-chemical studies,[122,125] since the reaction coordinate represents a linear combination of many normal modes, including modes with much higher frequencies and thus shorter vibrational periods.

Based on this theoretical description and extensive previous theoretical efforts,[116,122,123,125] we assign the coherence activity observed in the C-C stretching region (1208, 1237, 1267 cm^{-1}), the $C_{10/12}$-H HOOP modes (850, 875 cm^{-1}) and the C=C stretching shoulder at 1535 cm^{-1} to tuning modes of the isomerisation reaction. This assignment is further supported by the excited-state lifetime of rhodopsin (50-100 fs) requiring high-frequency FC-active modes with short vibrational periods to act as efficient tuning coordinates. Minor deviations from the RR intensities as seen for the $C_{10/12}$-H HOOP or the C=C stretch are likely due to different frequencies in ground and excited electronic states.[105] The complete lack of activity in the 920 cm^{-1} mode in the resonant time-domain Raman spectrum (Figure 4.3b) suggests that the C_{11}-H HOOP is one of the major coupling modes of the system. This assignment is also supported by recent high-level quantum mechanical calculations suggesting an asynchronous bicycle-pedal motion with major involvement of the C_{11}-H HOOP.[122] We remark that our technique is surprisingly insensitive to the photo to bathorhodopsin structural relaxation previously observed with femtosecond stimulated Raman spectroscopy (FSRS),[131] resulting in a Fourier power spectrum that mainly reflects the properties of the final (vibrationally hot) bathorhodopsin photoproduct.

Theoretical Analysis of HOOP Frequency Shifts

Previous studies using FSRS have shown that in particular the HOOP region around 900 cm^{-1} undergoes significant frequency shifts, sensitive to the underlying isomerisation reaction.[131] The model put forward contains a set of three C-H out-of-plane modes with an exponential change in frequency. To model the effect of such frequency shifts in our experiment, we adopted the revised model devised by McCamant[138] and simulated three C-H out-of-plane modes with frequency shifts according to Figure 4.5a. By combining the resulting oscillations, we are able to obtain a single coherence, as shown in Figure 4.5b

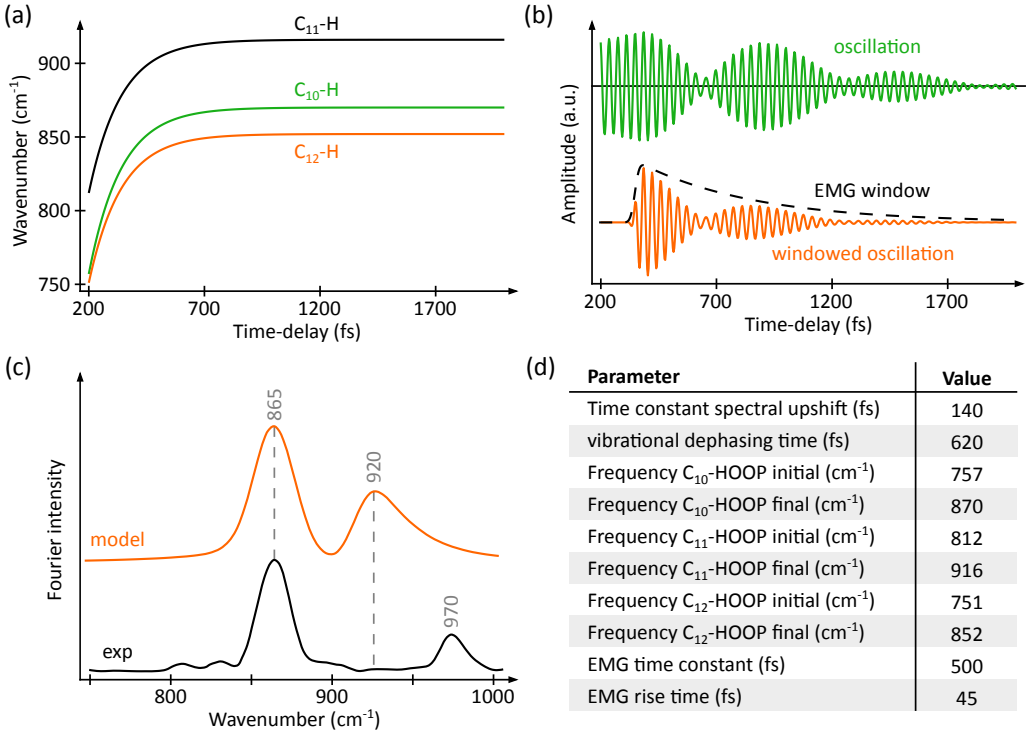

Parameter	Value
Time constant spectral upshift (fs)	140
vibrational dephasing time (fs)	620
Frequency C_{10}-HOOP initial (cm^{-1})	757
Frequency C_{10}-HOOP final (cm^{-1})	870
Frequency C_{11}-HOOP initial (cm^{-1})	812
Frequency C_{11}-HOOP final (cm^{-1})	916
Frequency C_{12}-HOOP initial (cm^{-1})	751
Frequency C_{12}-HOOP final (cm^{-1})	852
EMG time constant (fs)	500
EMG rise time (fs)	45

Figure 4.5: Simulation details of HOOP evolution. (a) Time-dependent frequency shifts for hydrogen out-of-plane motions C_{10}-H, C_{11}-H and C_{12}-H. (b) Resulting overall coherent oscillation (green, top) and EMG windowed oscillation (bottom, black and orange, respectively). (c) Obtained Fourier power spectra of simulated data (orange) compared to experimental results showing the lack of the 920 cm^{-1} C_{11}-H mode. (d) Overview of simulation parameters adapted from McCamant.[138] Note that the relative initial phases have been assumed to be zero, zero and π for C_{10}-H, C_{11}-H and C_{12}-H modes to account for the overall isomerisation process.

(green). Application of an exponentially-modified Gaussian (EMG) window function (Figure 4.5b, orange) followed by Fourier transformation reveals the expected Fourier power spectrum (Figure 4.5c, orange). In addition to the model parameters given in Figure 4.5d,[138] we have to assume an initial phase for each oscillation at a time delay of 200 fs. We assumed a phase of zero for the C_{10}-H and C_{11}-H while a phase of π was set for C_{12}-H. The latter phase was chosen to be out-of-phase with the C_{11}-H vibration to ensure that the respective hydrogen atoms move away from each other to lead to an isomerisation. If the hydrogen atoms were to start in-phase, no net isomerisation would occur on the reaction time scale of photoexcited rhodopsin. Comparison to the experimental data, analysed in the same way shows excellent agreement in the 860 cm^{-1} mode. However, the lack of the C_{11}-H mode at 920 cm^{-1} cannot be explained by this model, providing additional evidence for the effect of a CI on a vibrational

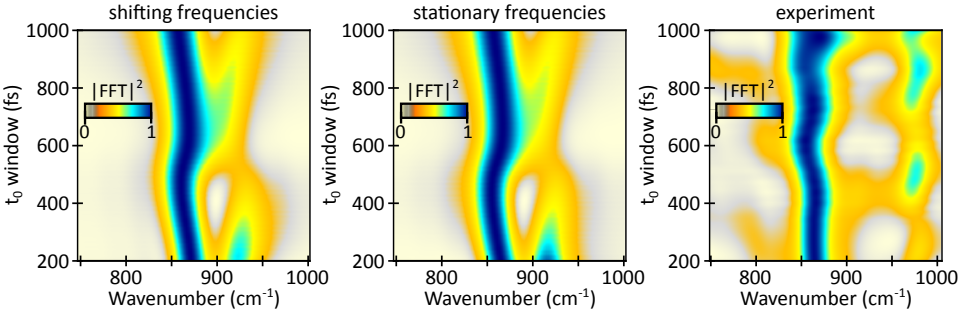

Figure 4.6: Sliding-window Fourier transform analysis of the model presented in Figure 4.5 (left), a set of stationary bathorhodopsin modes (middle) and the experimentally observed data (right) as a function of the window time delay, t_0. The spectra for each window time delay have been normalised to the largest mode for visibility purposes.

wavepacket in a coupling mode. We note that the observed lineshape of the 860 cm^{-1} mode in the Fourier power spectrum was not reproducible if we assumed phases of zero, π and zero for the C_{10}-H, C_{11}-H and C_{12}-H modes instead.

To trace potential frequency shifts, we performed a sliding-window Fourier transform (SWFT) on this model (Figure 4.6, left), a model with non-shifting, stationary oscillations at bathorhodopsin HOOP frequencies (Figure 4.6, middle), and our experimental data (Figure 4.6, right). The Fourier power spectrum as a function of the window position is obtained and scaled to the maximum for each window time, removing exponential decay dynamics for clarity. We observe only minor differences between between the two sets of simulated data, both showing clear signatures of the C_{11}-H mode at 920 cm^{-1}. In contrast, the experimental data never shows the appearance of this mode, strengthening the proposed coupling mode mechanism. Residual oscillations in the SWFT of the measured data are mainly caused by the interference with the residual rhodopsin mode at 970 cm^{-1}.

These results show that the detection of frequency shifts in the time domain is very challenging. While in FSRS all oscillations are generated in-phase when the Raman probe pulse interacts with the sample, we are initiating the VC directly upon photoexcitation. Since we cannot temporally separate excitation and coherence generation, our method becomes less phase sensitive to the overall isomerisation and provides spectral signatures dominated mainly by the bathorhodopsin photoproduct. It is this difference, however, which allows us to obtain information on the CI by careful comparison to the reactant and product Raman spectra. To reproduce the FSRS data, actinic-pump-probe

(APP) IVS would have to be performed.

4.3 Conclusions

We have used ultrafast transient absorption spectroscopy with high temporal resolution and spectroscopic sensitivity to investigate the fate of nuclear wavepackets generated by photoexcitation after internal conversion mediated by a CI during a photochemical process. When comparing the coherence spectrum after passage through the CI with the RR spectrum of the photochemical product, we observed both strong enhancement and suppression of coherences. This behaviour is in contrast to that observed during the $S_2 \leftarrow S_1$ internal conversion in β-carotene.[99] There, some high-frequency (>600 cm^{-1}) coherences are amplified while the other mode intensities remain unchanged. The major difference between the two systems is that in β-carotene only small structural changes are coupled to the internal conversion, while a complete photoisomerisation is driven in rhodopsin. As a result, we observe clear differences in coherence intensities compared to the RR spectrum of bathorhodopsin that can be explained by the displacement of the respective potential energy surfaces upon internal conversion. Our results provide a strong proving ground for theoretical studies, especially in the comparison of how nuclear wavepackets are affected by a CI for reactive and unreactive processes. The ability to monitor VC throughout chemical reactions and across multiple electronic surfaces is likely to provide detailed insight into the mechanistic and structural origins of ultrafast processes such as charge and proton transfer, singlet fission and photochemical transformations in general.

Methods

Sample Preparation

Rhodopsin ($OD_{500\,nm} = 15$) was obtained from rod outer segments of bovine retinae and purified by sucrose flotation followed by sucrose density gradient centrifugation, as described by de Grip *et al.*[10,139] Hydroxylamine was added to a final concentration of 2 mM to suppress the accumulation of photoproduct.

Ultrafast Spectroscopy

Transient absorption traces were recorded employing <10 fs visible and near-IR pump pulses centred at 500 nm and 800 nm together with chirped continuum probe (500-900 nm) at a repetition rate of 1 kHz. The samples were flowed through a 200 μm pathlength flowcell ($\mathrm{OD}_{500\ \mathrm{nm}}^{200\ \mu\mathrm{m}} = 0.3$) by a peristaltic pump at a rate to ensure replenishment of the sample during consecutive pulses. Pump and probe diameters in the focus were 75 and 50 μm with corresponding pulse energies set to 60 nJ (visible pump), 120 nJ (near-IR pump) and 2.5 nJ (probe).

Chapter 5

Coherent Isotope Effect in Rhodopsin

All samples investigated in this chapter were provided by Katelyn M. Spillane.

5.1 Introduction

The primary event in vision is the 11-*cis* to all-*trans* photoisomerisation of the retinal chromophore in the trans-membrane protein rhodopsin.[121] Over the past decades, the reaction has become a paradigm for efficient photochemistry due to the associated high speed ($\tau = 200$ fs),[7] quantum yield (QY $= 0.65$)[140] and selectivity in the protein compared to the same chromophore in solution ($\tau = 5$ ps, QY $= 0.22$).[141] Extensive theoretical studies have proposed a number of potential origins for this discrepancy, including steric and dielectric constraints, effects induced by the protein pocket,[12,116,142,143] pre-distortion of the backbone structure[144] or the phase of vibrational motions upon encounter of the conical intersection connecting ground and excited electronic states.[122,135,136]

Experimental studies aimed at unravelling the source of this unique reactivity have either focused on characterising steady-state properties such as absorption spectra and QYs or changes in reaction kinetics after modification of the protein pocket or the retinal backbone.[113,145–147] All reported retinal modifications, however, have in common that they substantially alter the electronic structure of the chromophore, which in itself can have a dramatic effect on reaction speed and isomerisation QY, even in solution for apparently minor modifications such as the methylation of a single backbone hydrogen.[148,149] As a result, it is difficult to differentiate whether electronic effects on the chromophore or changes in the interaction with the protein pocket were responsible

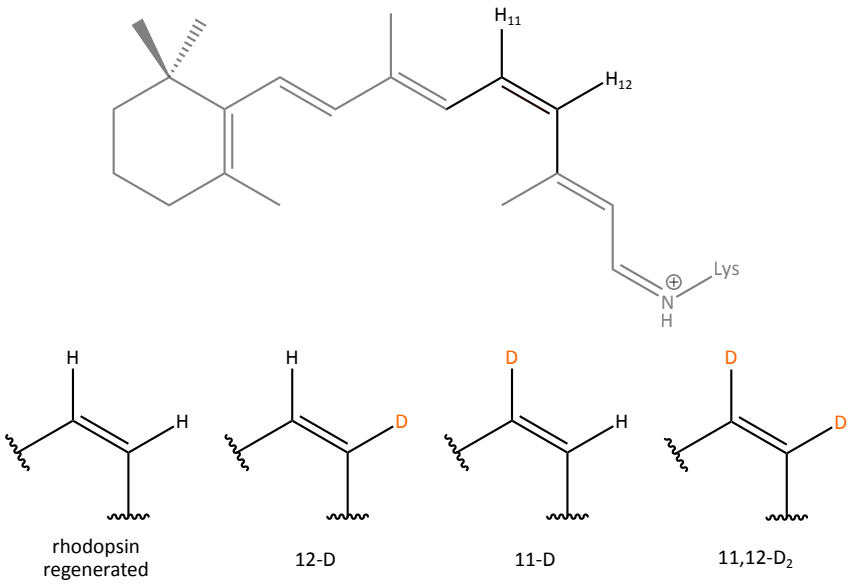

Figure 5.1: Native and isotopically labelled retinal chromophores in rhodopsin studied in this work.

for the changes in reactivity, and thus the physical origin of the observed effects.

We have thus opted for the smallest possible perturbation to the system, deuteration of the isomerising bond, and studied the ensuing kinetic and reactive consequences. The prepared synthetically modified retinal analogues, 11-D, 12-D and 11,12-D_2 allow us to keep the overall perturbation limited to changes in the vibrational frequencies and couplings of hydrogen out-of-plane motions (Figure 5.1).[146] All other modes and the electronic nature of the system are unaffected by this modification. The study is complemented by regenerated rhodopsin, which underwent the same synthetic procedure as the isotopes but without isotopic modification. We characterise the photophysics by recording the rise of the photoproduct via ultrafast transient absorption spectroscopy[8,95] and the isomerisation QY using stationary measurements with an incoherent light source.[140,145]

5.2 Results and Discussion

The growth of the photoinduced absorption band at 560 nm is a well-established marker for the formation of the primary bathorhodopsin photoproduct in the rhodopsin photocycle.[7,8,10] By averaging the transient absorption spectrum obtained after excitation with a 500 nm (20 fs) pump pulse we find excellent agreement amongst the studied compounds (Figure 5.2, left). All traces exhibit

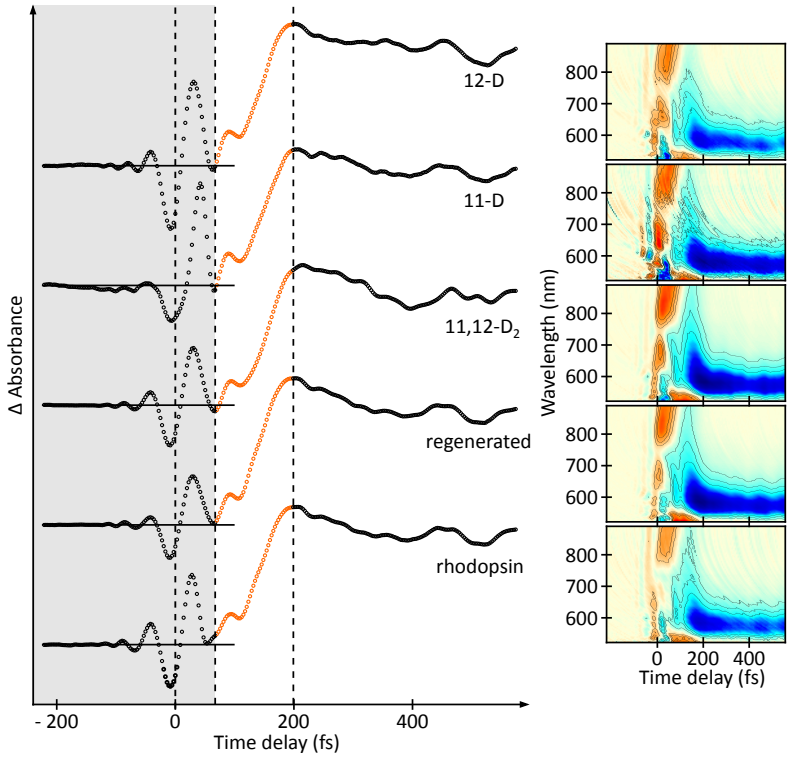

Figure 5.2: Transient absorption of isotopically labelled rhodopsins. Left: Spectral average over photoproduct absorption band from 545-590 nm. Transients are coloured according to the dominant contribution: grey - coherent artefact; orange - photoproduct rise, black - coherent photoproduct dynamics. Right: Corresponding broadband transient absorption maps illustrating the similarities in dynamics between different isotopes. CA contributions arising from non-resonant interactions have been subtracted.

a coherent artefact near zero pump-probe time delay,[95] a delayed (∼80 fs) rise of photoproduct signal that completes within 200 fs[8,10] as well as weak modulations of the electronic signal for longer time delays. The latter arise from impulsively generated vibrational coherence (VC) by the pump pulse and report on the structural evolution of the system, as shown previously.[8,95] The coherent artefacts appear nearly identical for all species with differences most likely due to the different optical densities available for the five samples (see methods). Minor differences in the traces are furthermore discernible in the appearance of the VC superimposed on the electronic signal in the 300-500 fs time delay window, as expected for changes in vibrational frequencies caused by isotopic substitution. The similarity observed in the photoproduct absorption transients persists throughout the entire probed region (Figure 5.2, right).

Comparison of the photoisomerisation QY for the same compounds, on the

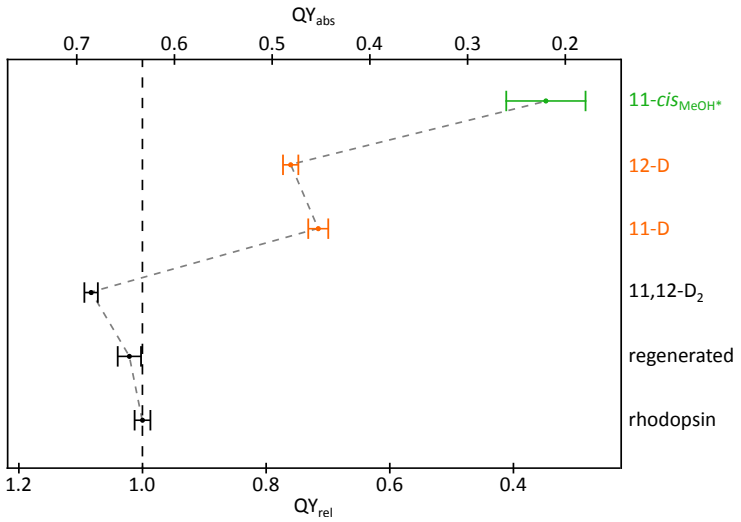

Figure 5.3: Isomerisation quantum yields for native and isotopically labelled retinal chromophores in rhodopsin and solution at 532 nm. Black - symmetrically substituted, orange - asymmetrically substituted, green - chromophore in methanol solution obtained in a different procedure (*).[149] The QY for the chromophore in solution was provided by Giovanni Bassolino.

other hand, reveals significant differences (Figure 5.3). The results separate into two groups: those with identical isotopic substitution at the C_{11}-C_{12} bond and those asymmetrically substituted. The first group (black) comprises of native and regenerated rhodopsin, as well as 11,12-D_2, showing a QY of 0.63 to 0.68. The second group (orange) contains 11-D and 12-D isotopes, which exhibit significantly lower QYs of 0.43 and 0.49. Despite this modification, the chromophores show still a considerably higher QY than the protonated chromophore in solution (0.22, green).

The similarity of the ultrafast dynamics shows that deuteration has no measurable influence on the excited-state lifetime, while the QY exhibits drastic differences (Figure 5.3). Such a pronounced effect on the QY without changes to the reaction speed implies that the QY and the reaction speed are highly decoupled in rhodopsin. In fact, our results illustrate that the C_{11}-H and C_{12}-H hydrogen out-of-plane (HOOP) motions are not rate-limiting in agreement with a barrierless excited-state potential energy surface, ruling out the influence of any traditional kinetic isotope effects reported for the related photoisomerisations in stilbene.[150]

To understand this observation, it is instructive to first consider a traditional Jablonski diagram representative of the 11-*cis* to all-*trans* isomerisation in rhodopsin (Figure 5.4a, black).[151] In this framework, the QY is derived as a

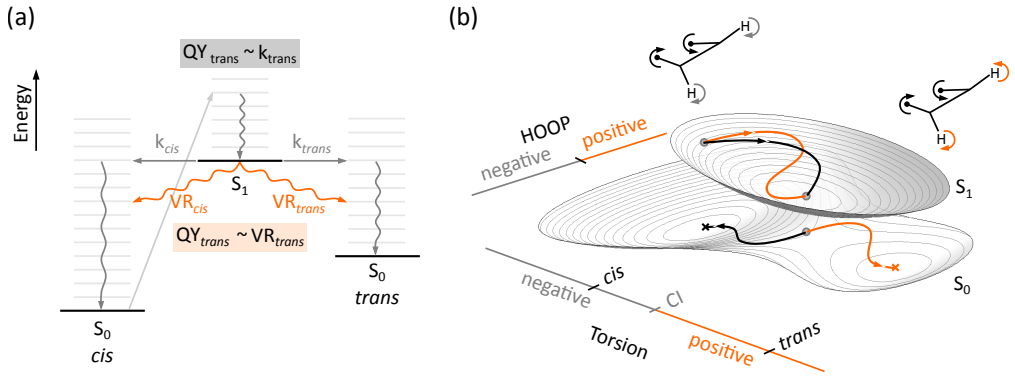

Figure 5.4: Energy level diagram and schematic potential energy surfaces for the retinal photoisomerisation in rhodopsin. (a) Jablonski diagram assuming branching into reactive and unreactive channels. Grey: Slow internal conversion providing a QY proportional to the rate of internal conversion. Orange: Fast internal conversion providing a QY proportional to the VR on the ground electronic state. (b) Potential energy surfaces illustrating the effect of hydrogen out-of-plane (HOOP) motions on the nuclear evolution out of the Franck-Condon region via a conical intersection (CI). Orange trajectory: Successful isomerisation due to the correct phase-space coordinate of HOOP and torsional modes. Black: Unsuccessful isomerisation since the HOOP mode is not correctly located in phase-space as found for asymmetrically substituted isomers.

branching ratio between all possible decay channels after vibrational relaxation (VR) has taken place, making the QY for photoproduct formation directly proportional to the internal conversion rate for photoproduct formation (k_{trans}). We observe, however, no change in the excited-state lifetimes despite large QY variations, which is not explained by a Jablonksi diagram treatment. The discrepancy stems from the extremely short excited-state lifetime of rhodopsin (<100 fs), which takes place on a much faster time scale than typical VR (∼1 ps). Consequently, QYs can no longer solely be determined by the electronic dynamics alone.

Since the dynamics of the system are invariant to isotopic substitution, the reaction outcome is most likely decided close to or at the surface crossing. This interpretation is in line with recent quantum-chemical calculations that predict that both reactive and unreactive surface crossings take place on similar time scales within the first 100 fs after photoexcitation.[122,123] Based on this assumption, the experimental observations might be explained in a simple extended branching model which replaces rate constants with the individual VR time constants to the respective ground-state configuration (Figure 5.4a, orange). In such a model, we would, however, expect a monotonic

trend in isomerisation QYs with respect to the level of isotopic substitution. Instead, we find that symmetrically substituted retinal chromophores (11,12-H_2 and 11,12-D_2) exhibit increased reactivity compared to single deuteration, implying that the QY must crucially depend on the nature of the HOOP motion. In symmetrically substituted isotopes, the C_{11}-H and C_{12}-H out-of-plane motions are coupled and form symmetric and anti-symmetric HOOP modes.[146] This splitting most likely enables the anti-symmetric HOOP mode to couple efficiently to a torsional subset of the isomerisation coordinate and promotes isomerisation at the surface crossing. On the other hand, if the C_{11}-H and C_{12}-H out-of-plane motions are decoupled, torsional coupling is also reduced, which in turn lowers the QY for isomerisation as observed for asymmetrically substituted isotopes.

Such a behaviour can only be explained if the reaction outcome is decided upon internal conversion through a phase-space-dependent conical intersection.[136] At a given conical intersection coordinate, the system will only have a momentum vector pointing towards the photoproduct for symmetric substitution, while asymmetric substitution will have the wrong momentum vector, inhibiting isomerisation (Figure 5.4b). Since the reaction proceeds on an ultrashort time scale, the conical intersection space cannot be equally sampled leaving only selected conical intersection space coordinates which lead to isomerisation. The momentum vector thus becomes critically dependent on the vibrational modes that constitute the isomerisation coordinate. Our results show that the HOOP modes are crucially involved in the isomerisation coordinate and define how the phase-space at the conical intersection is sampled to result in successful isomerisation. As a consequence, it is not possible to directly predict the outcome of an ultrafast photoisomerisation, since a detailed knowledge of the underlying potential energy surface is required to determine the relevant phase-space coordinates leading to a successful reaction.

5.3 Conclusion

We employed broadband transient absorption spectroscopy to determine the photoproduct dynamics of isotopomers of 11-*cis* retinal in rhodopsin (11-D, 12-D, 11,12-D_2). The results were complemented by evaluating the corresponding photoisomerisation quantum yields using an incoherent light source. Our results are consistent with a model in which reaction speed and QY cannot be

explained with a competition between decay rate processes alone. Instead, our observations suggest that a phase-space approach is a better description, in which a higher probability of finding the two protons on opposite sides of the isomerising bond while moving towards a *trans* conformation at the surface crossing, equates to a higher QY.

Methods

Sample Preparation

Samples were prepared according to Eyring *et al*[146] with the following optical densities: $OD^{rho}_{500\ nm} = 3.0$, $OD^{11,12\text{-}D_2}_{500\ nm} = 4.2$, $OD^{regen}_{500\ nm} = 3.4$, $OD^{11\text{-}D}_{500\ nm} = 0.54$ and $OD^{12\text{-}D}_{500\ nm} = 1.3$. NH_2OH was added before the experiment to avoid photoproduct accumulation.[139]

Ultrafast Spectroscopy

Transient absorption traces were recorded using a 20 fs visible pump pulse centred at 500 nm and a 1030 nm generated continuum probe at a repetition rate of 1 kHz. The samples were flowed through a 500 μm pathlength flowcell ($OD^{500\ \mu\ m}_{500\ nm} = 0.027\text{-}0.21$) by a peristaltic pump at a rate to ensure replenishment of the sample during consecutive pulses. Pump and probe diameters in the focus were 65 and 44 μm with corresponding pulse energies set to 20 nJ and 2.5 nJ, respectively.

Quantum Yield Measurements

A 532 nm continuous-wave laser output (0.6 mW) was polarisation cleaned by a Glan-Taylor polariser (Thorlabs), narrow-band filtered (532 nm, FWHM = 10 nm, Thorlabs) and attenuated to 1 μW before being split by a 50:50 beamsplitter (Thorlabs) into a reference and a sample beam. The sample beam illuminated a 1 cm pathlength quartz cuvette. Both reference and transmitted sample beams were subsequently detected with an emCCD (Andor iXon3 860, Figure 5.5a). The signal and reference beams were integrated over the spot size (Figure 5.5b), converted to incident power (corrected for 4.5% backreflection of the cuvette) and used to obtain a referenced signal. Afterwards, application of a 5-point running-average filter cleaned the referenced signal, before it was converted into OD (Figure 5.5c).

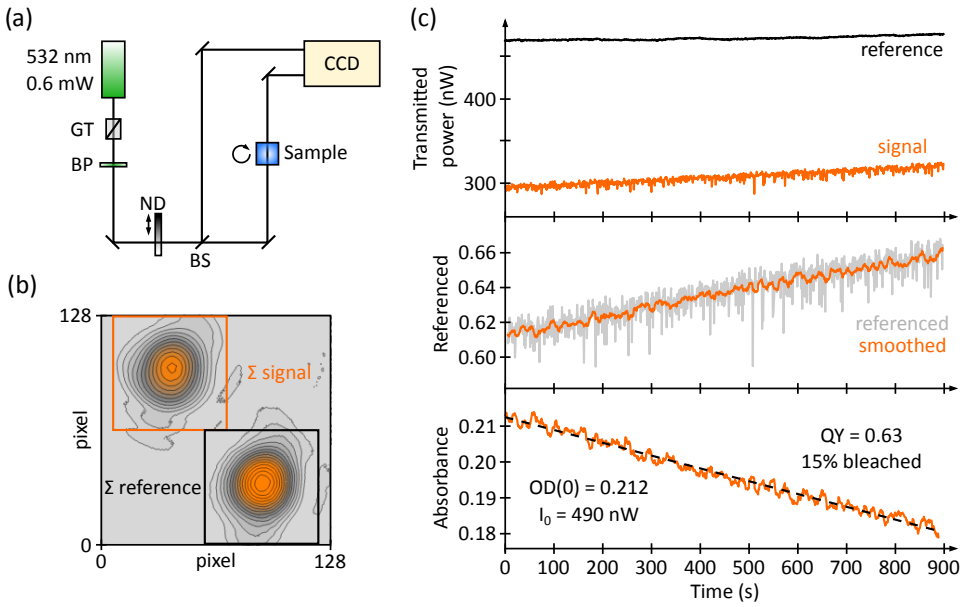

Figure 5.5: QY determination for isotopomers of rhodopsin. (a) Referencing setup employing a 532 nm continuous-wave light source and a magnetically stirred sample cell. (b) Detected beam arrangement collecting the reference and signal beams. (c) Overview over data analysis steps for rhodopsin. Top: Recorded incident powers on sample and reference arm. Middle: Referenced trace employing a 5-point moving average smoothing filter. Bottom: OD trace (orange) and linear fit (black) showing the bleaching of the sample. GT - Glan-Taylor polariser (Thorlabs), BP - band-pass filter (532 nm, FWHM = 10 nm, Thorlabs), BS - 50:50 beamsplitter (Thorlabs), ND - neutral-density filter.

Samples were diluted with buffer solution to an OD of ∼0.2-0.3 and NH_2OH was added to avoid photoproduct accumulation,[139] giving a total volume of 540 μl. The sample was stirred constantly during the measurement. Every sample was illuminated for 20 min corresponding to bleaching of $\leq$15% of the initial number of molecules. From the change in OD and the measured reference beam power, the QY, Φ, at 532 nm was calculated from the initial rates method described by Kochendoerfer *et al*[145] which expresses the change in OD with time as

$$\frac{d\mathrm{OD(t)}}{dt} = -2.3\,\mathrm{OD}(0)\,\epsilon\,l\,I_0\,\Phi, \tag{5.1}$$

where l is the pathlength, ϵ the molar extinction coefficient at the excitation wavelength, OD(0) the initial optical density and I_0 the average incident power on the sample. The measurements were repeated four times to obtain approximate error margins of this method and special care was taken to use only measurements during which no significant power drift in the illumination was observed.

Chapter 6

Vibronic Dynamics of the Ultrafast all-*trans* to 13-*cis* Photoisomerisation of Retinal in Channelrhodopsin-1

The following work was carried out in collaboration with Vera Muders, David Ehrenberg, Ramona Schlesinger and Joachim Heberle (FU Berlin). The protein samples were provided by Vera Muders and David Ehrenberg measured the low-temperature Raman spectrum. Ramona Schlesinger and Joachim Heberle supervised the project in Berlin.

6.1 Introduction

Photoreceptors form an important class of membrane proteins with a wide range of functionalities such as visual signalling, proton pumping and ion channeling.[13,121,152] Channelrhodopsins, which act as light-activated cation channels, have recently received great attention due to their enormous potential in optogenetics, an emerging field where photosensory proteins trigger physiological responses by light. Most prominently, channelrhodopsins are used in neuroscience to depolarise specific nerve cells upon light activation.[13,14] Originally, channelrhodopsins are located in the eyespot of green flagellate algae to mediate phototaxis[153] and can be divided in channelrhodopsin-1 (ChR1) and channelrhodopsin-2 (ChR2) based on their structural and mechanistic differences.[154,155] Channelrhodopsin-2 from *chlamydomonas reinhardtii* (*Cr*ChR2) is mostly used in optogenetics[156] and has been subject to a range of spectroscopic studies on the intermediates contributing to the photocycle.[155,157–160]

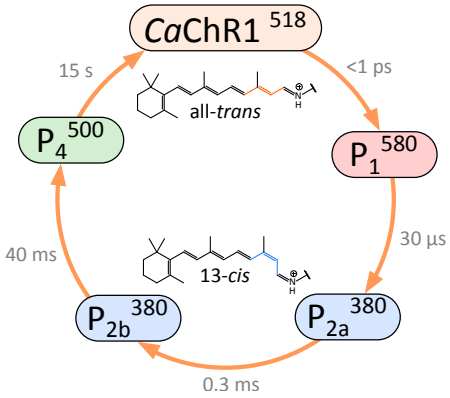

Figure 6.1: Photocycle of *Ca*ChR1. The photocycle is initiated by irradiation of the all-*trans* retinal chromophore of *Ca*ChR1 and proceeds via a 13-*cis* intermediate. Absorption maxima are indicated as superscripts and interconversion time constants are given in grey.

Much less is known about the dynamics of *Cr*ChR1, largely due to the difficulties associated with overexpression to obtain sufficient amounts of protein for biophysical analysis. In contrast, channelrhodopsin-1 derived from *chlamydomonas augustae* (*Ca*ChR1) can be heterologously expressed in large quantities in the yeast *pichia pastoris*.[14,159] Moreover, *Ca*ChR1 has two desirable features for optogenetic application: (i) slower inactivation under continuous illumination and (ii) a red-shifted absorption maximum allowing for deeper penetration of the excitation light into biological tissue.[14]

*Ca*ChR1 exhibits a heterogeneous ground-state population of chromophore isomers comprised of 30% 13-*cis* to 70% all-*trans* retinal with a protonated Schiff base and an absorption maximum at 518 nm.[159] The photocycle of *Ca*ChR1 has been analysed using time-resolved UV/Vis, resonance Raman and FT-IR spectroscopy (Figure 6.1).[159,161–163] Photoexcitation results in an early P_1 intermediate at 580 nm, followed by a long-lasting biphasic $P_{2a,b}$ intermediate at 380 nm on the millisecond time scale which matches the lifetime of the cation current. While in *Cr*ChR2 a red-shifted P_3 intermediate was detected, no such intermediate is present in the photocycle of *Ca*ChR1.[163,164] Here, mainly the P_2 intermediate accumulates under continuous illumination at room temperature, facilitating the biophysical analysis of the conductive state in *Ca*ChR1. Resonance Raman spectroscopy revealed that the P_2 intermediate consists of 13-*cis* retinal with a deprotonated Schiff base.[159] Additionally, large conformational changes as well as hydrogen-bonding changes of carboxylic groups, cysteine side chains and of a dangling water molecule were detected between the closed and

the open state of *Ca*ChR1 via FT-IR difference spectroscopy. After channel closure, time-resolved IR spectroscopy revealed ongoing conformational changes in the P_4 intermediate.[164] The key structural changes occurring directly after photoexcitation, however, are poorly understood, as structural information on the early photocycle of *Ca*ChR1 is restricted to photointermediates trapped under cryogenic conditions.[162]

Here, we combine high time-resolution (<10 fs) transient absorption spectroscopy,[28,95] actinic-pump-probe impulsive vibrational spectroscopy[85,98] and low-temperature resonance Raman spectroscopy to characterise the vibronic dynamics of the all-*trans* retinal chromophore in *Ca*ChR1 during the primary photoisomerisation event. Although the kinetics of this process have been recently reported using ultrafast UV/Vis spectroscopy, the structural dynamics remain uncharacterised.[165] We show that *Ca*ChR1 undergoes a rapid photoisomerisation to the first stable P_1 intermediate containing 13-*cis* retinal, with an exponential time constant of 110 fs. This intermediate appears to persist for several hundreds of nanoseconds.

6.2 Results and Discussion

Following photoexcitation of *Ca*ChR1 with an 8 fs pulse centred at 560 nm, we observe ground-state bleaching around 520 nm, partially overlapped with a red-shifted photoinduced absorption (PIA) band at 600 nm and a rapidly decaying stimulated emission (SE) band at 850 nm, similar to previous reports for bacteriorhodopsin.[98,129,134] After 500 fs, the SE band has decayed completely while the PIA and ground-state bleach (GSB) bands persist and decay on a slower time scale, accompanied by a blue-shift and narrowing of the PIA. A global fitting routine employing an offset and two exponential decay functions is sufficient to describe the observed dynamics. The first time constant (110 fs) correlates with the rapid decay of the SE, while the second time constant (600 fs) is predominantly related to the spectral blue-shift of the GSB and PIA contributions, as indicated in Figure 6.2a (orange and black transient spectra). The transient absorption spectrum at 1400 fs appears almost identical to a spectrum recorded at a time delay of 700 ns via flash photolysis, suggesting that the formation of the previously assigned intermediate, P_1,[165] completes on a sub-picosecond time scale. Identical dynamics were retrieved using a red-shifted pump pulse centred at 580 nm (20 fs).

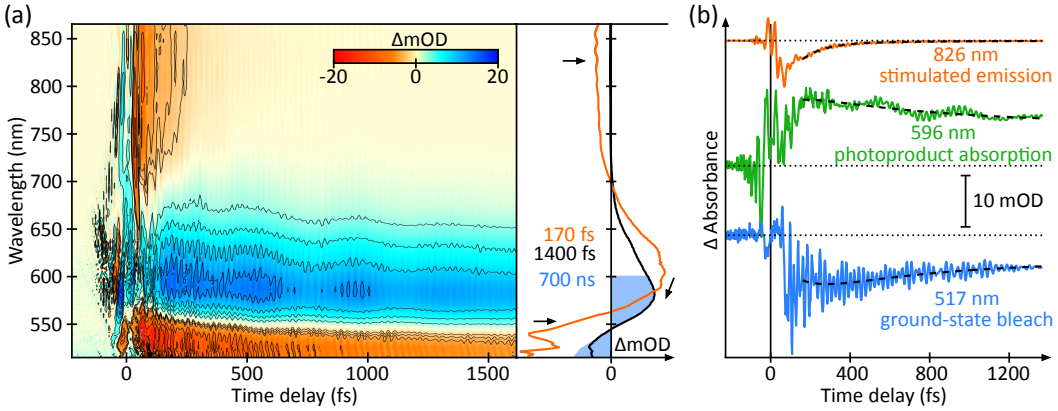

Figure 6.2: Ultrafast vibronic dynamics of *Ca*ChR1. (a) Transient absorption map of *Ca*ChR1 employing a visible pump pulse (560 nm, 8 fs) and a chirped broadband whitelight continuum probe pulse (500-900 nm, 4.5 fs transform limit). Early coherent artefact contributions (-100 to 100 fs) have been subtracted for clarity. Selected transient absorption spectra at 170 fs (orange) and 1400 fs (black) illustrating the rapid initial photodynamics are shown on the right with arrows indicating spectral changes. A flash photolysis spectrum obtained at a time delay of 700 ns for comparison (blue) suggests no significant spectral evolution after the initial fast response over several hundreds of nanoseconds. (b) Selected transients demonstrating the main dynamic characteristics with exponential fits (dashed black). We remark that the electronic signals show pronounced oscillatory modulations. The flash photolysis spectrum was provided by Vera Muders.

Closer examination of the individual transients (Figure 6.2b) reveals that the dynamics of the dominant transient absorption features are modulated by coherent oscillations, particularly pronounced in the PIA and GSB band, as previously reported for bacteriorhodopsin and visual rhodopsin.[7,95,98] The origin of the vibrational coherence (VC) is impulsive generation of nuclear wavepackets by the excitation pulse.[47,48,85,94] After subtraction of the slowly varying electronic dynamics, a Fourier transform of the residual coherent oscillations reveals the wavelength-dependent impulsive Raman spectra of the system (Figure 6.3a). The Fourier intensities decrease towards the near-IR with maxima close to the GSB and PIA bands, in line with previous reports.[95] We find strong contributions in the low-frequency region (<500 cm^{-1}) with dominant modes at 81 cm^{-1} and in the hydrogen out-of-plane (HOOP, ∼1000 cm^{-1}), C-C (∼1200 cm^{-1}) and C=C (∼1530 cm^{-1}) stretching regions (Figure 6.3b, green spectrum).[159]

A transient absorption experiment employing a short resonant pump pulse will generate both, ground- and excited-state VC, leading to a superposition of spectral features. To identify VC arising from photoexcited molecules only,

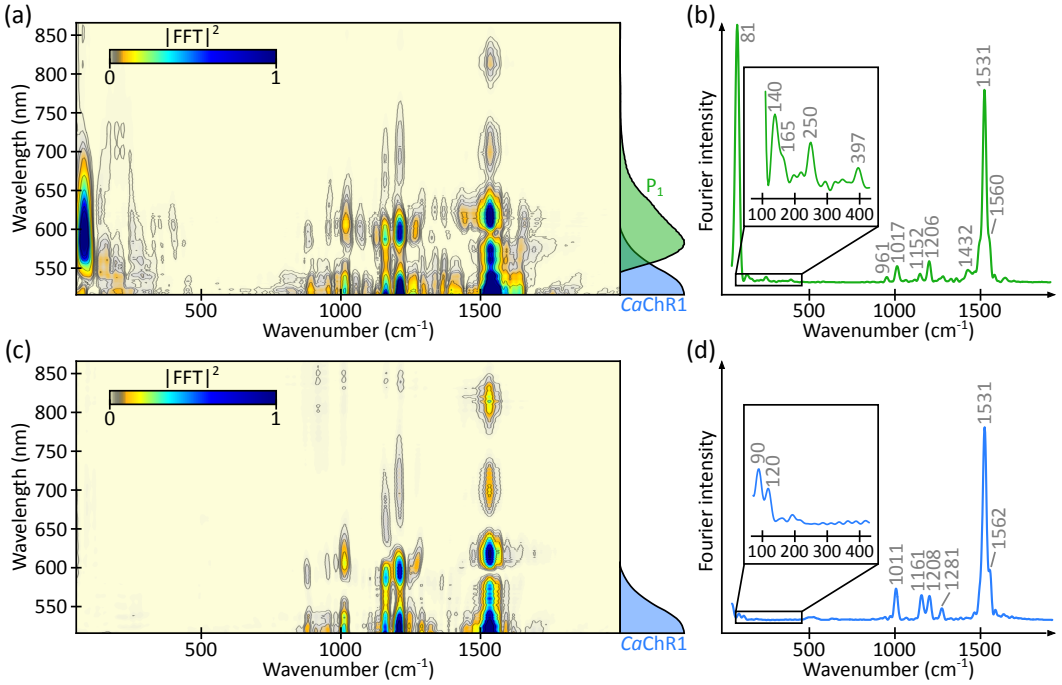

Figure 6.3: Time-domain impulsive vibrational spectroscopy on *Ca*ChR1. (a)Wavelength-resolved Fourier transform power map of *Ca*ChR1 obtained with a resonant 8 fs pump pulse centred at 560 nm. Representative absorption spectra of the photoproduct (P_1, green) and ground electronic state (*Ca*ChR1, blue) are shown for comparison. (b) Spectral average over the low-energy side of P_1 (620-680 nm) showing strong activity in the low-frequency region below 500 cm^{-1}. (c) Wavelength-resolved Fourier transform power map of *Ca*ChR1 obtained with a 9 fs off-resonant pump pulse centred at 800 nm providing exclusively ground-state contributions. The ground-state absorption spectrum is shown for comparison (*Ca*ChR1, blue). (d) Spectral average over the same probe region as in (b) lacking all major activity in the low-frequency region as well as the mode at 961 cm^{-1}.

we repeated the experiment under identical conditions with an off-resonant pump pulse centred at 800 nm (9 fs) generating exclusively ground-state VC.[65] The resulting wavelength-dependent Fourier transform power map reveals intense coherence activity in the HOOP, C-C and C=C stretching regions with an almost identical wavelength-dependence as under resonant conditions, while lacking all activity in the low-frequency region (Figure 6.3c, d). Closer inspection reveals that off-resonant excitation generates less coherence activity around the PIA band at 600 nm, providing evidence for a vibrationally coherent formation of the P_1 intermediate, as observed for visual rhodopsin.[8] This is further emphasised in a comparison of the spectral average at the low-energy side of the P_1 absorption spectrum from 620-680 nm. We find altered relative intensities of the fingerprint modes >800 cm^{-1} upon resonant excitation and

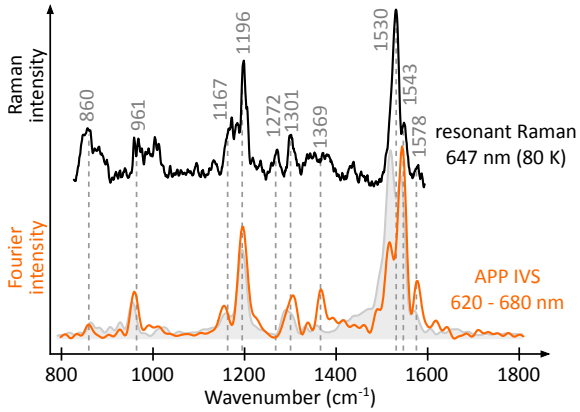

Figure 6.4: Raman spectra of the P_1 intermediate of *Ca*ChR1. Top: Low-temperature (80 K) resonance Raman spectrum of the primary photoproduct, P_1, obtained at 647 nm following photoexcitation at 502 nm. Bottom: Actinic-pump-probe impulsive vibrational (APP IVS) spectrum of the P_1 intermediate recorded 1 ps after photoexcitation at 515 nm (200 fs) using a 9 fs impulsive pump pulse centred at 800 nm (orange). The grey spectrum represents the extracted IVS spectrum using the same subtraction algorithm employed in the resonance Raman spectrum (see methods). The IVS spectral intensities have been corrected for the finite time resolution of the experiment and averaged over the low-energy side of the photoproduct absorption band from 620-680 nm. Vertical dashed lines indicate matching frequencies and are labelled accordingly. In particular the modes at 860, 961, 1196 and 1301 cm^{-1} are sensitive marker modes for the 13-*cis* configuration of retinal in the photoproduct state.[166,167] The low-temperature resonance Raman spectrum was provided by David Ehrenberg.

an additional mode at 961 cm^{-1} which forms a sensitive marker mode of a twisted retinal geometry.[166] This observation strongly supports the notion that the P_1 state with 13-*cis* retinal is formed in less than 1 ps.

To further validate this assignment, we trapped the P_1 state at cryogenic temperatures (80 K) to perform resonance Raman spectroscopy using continuous-wave excitation at 647 nm after photoexcitation at 502 nm. Upon subtraction of the ground-state spectrum recorded in the absence of photoexcitation under otherwise identical conditions, we obtain the resonance Raman spectrum of the P_1 state (Figure 6.4, black spectrum). In addition, we carried out room temperature actinic-pump-probe impulsive vibrational spectroscopy (APP IVS)[85] to determine the configuration of the molecular species present 1 ps after photoexcitation (Figure 6.4, orange spectrum). We find excellent agreement between the resonance Raman and APP IVS spectra, strongly supporting the earlier structural assignment. In particular the HOOP modes at 860 and 961 cm^{-1} are sensitive markers for a distorted retinal conformation.

Furthermore, the modes in the C-C stretching region at 1167, 1196 cm^{-1} and in the methyl rocking region at 1301 cm^{-1} indicate that retinal exhibits a 13-*cis* configuration.[166,167] The modes at 1196, 1301 and 961/959 cm^{-1} were also observed in the FT-IR difference spectrum of the P_1 intermediate.[162] This demonstrates that the initial photoisomerisation from all-*trans* to 13-*cis* retinal in *Ca*ChR1 occurs on a sub-picosecond time scale.

We observe small frequency shifts between the APP IVS and resonant Raman spectra (Figure 6.4, orange and black spectra), which may arise due to the cryogenic temperatures required to trap the P_1 state in the resonance Raman experiment (<8 cm^{-1}),[168] or due to different spectral resolutions between the two spectra. Furthermore, we find altered relative intensity ratios between the two Raman spectra, in particular in the C=C stretching region (1530/43 cm^{-1}), which are not explained by the temperature difference. Instead, a difference in subtraction algorithm accounts for the inverted intensity distributions. In APP IVS, the extracted Raman spectrum is derived from a global minimisation routine in the time domain, as outlined elsewhere.[85] The low-temperature resonance Raman spectra, on the other hand, were subtracted by minimising with respect to a significant ground-state mode (see methods). By re-analysing the APP IVS data in an analogous way to the resonance Raman procedure we retrieve a similar relative intensity distribution as found in the low-temperature resonance Raman spectrum (Figure 6.4, grey spectrum). We stress that the remaining fingerprint region is unaffected by the choice of subtraction algorithm. Further minor intensity differences might be explained by the different resonance conditions employed, arising from the wavelength-dependent photodynamics of *Ca*ChR1.[165]

The structural assignment of the P_1 state allows us to explain the appearance of the direct-excitation Fourier Raman spectra (Figure 6.3a,b). Low-frequency modes in *Ca*ChR1 are strongly enhanced upon photoexcitation, also observed for visual rhodopsin.[95] Such a behaviour is characteristic for an isomerisation coordinate comprising a number of low-frequency retinal backbone modes, which is crucial to obtain a controlled photoisomerisation reaction capable of dissipating the excess photon energy rapidly. As a consequence, large low-frequency coherence activities arise, since low-frequency modes provide an internal energy sink for excess excitation energy for ultrafast processes on a sub-picosecond time scale.[169,170] We further attribute the small intensity changes observed between the impulsive Fourier Raman spectra >800 cm^{-1}

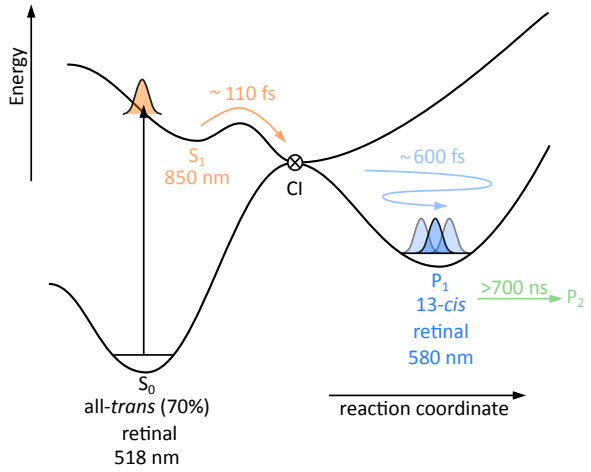

Figure 6.5: Potential energy surface diagram for the primary isomerisation event in *Ca*ChR1. Photoexcitation at the absorption maximum (518 nm) promotes predominantly all-*trans* molecules to a short-lived (110 fs) excited electronic state characterised by a SE band at 850 nm. After crossing back to the ground-state potential energy surface through a conical intersection (CI), a fraction of molecules form the primary photoproduct, P_1, with 13-*cis* retinal. Subsequent cooling with a 600 fs time constant relaxes the isomerised molecules, forming an intermediate that is stable for several hundred nanoseconds.

with the presence of an intermediate with 13-*cis* retinal. However, due to the strong contamination of the resonant spectrum by ground-state features (1206/8, 1531 cm^{-1}) it is challenging to make a confident structural assignment. In contrast, APP IVS (Figure 6.4) significantly suppresses this background and confirms that the observed intensities are indeed due to the photoisomerisation reaction forming a 13-*cis* intermediate, with pronounced marker modes for a distorted 13-*cis* retinal such as the HOOP (861 and 961 cm^{-1}), C-C stretching (1167 and 1196 cm^{-1}) and methyl rocking (1301 cm^{-1}) modes.

Combining these experimental results, we can assign the initial steps in the photocycle of *Ca*ChR1 (Figure 6.5). Absorption of a photon at 515-560 nm preferentially excites all-*trans* retinal chromophores to the first excited electronic state,[165] followed by rapid relaxation to an excited-state plateau characterised by a SE band at 850 nm. The structure associated with this plateau is most likely already pre-twisted along the 13-*trans* bond of retinal, in analogy to bacteriorhodopsin,[98] but due to the extremely short lifetime (110 fs) it is not possible to obtain an insightful vibrational signature of this state.[99] We emphasise that the exponential dynamics observed for the SE necessarily imply an excited-state barrier despite the short excited-state lifetime, in contrast to the ballistic dynamics observed in the barrierless photoisomerisation in visual

rhodopsin.[10,95] After passing the small excited-state barrier, crossing back to the ground-state potential energy surface through a conical intersection[99,148,149] leads to the vibrationally coherent formation of a hot P_1 intermediate with retinal in a twisted 13-*cis* configuration. The associated coherence activity of the low-frequency modes (Figure 6.3a,b) suggests that the reaction coordinate is in fact not a simple normal mode but a superposition of several low-frequency modes which also function as an internal heat sink to prevent coherent re-crossing back to S_1.[105] Subsequent vibrational cooling on a 600 fs time scale forms a stable P_1 isomer containing 13-*cis* retinal, with an absorption maximum at 585 nm, which appears to persist for several hundreds of nanoseconds before it turns into the conductive P_2 intermediate.[159]

6.3 Conclusion

We have used high time-resolution (<10 fs) transient absorption spectroscopy to characterise the transient vibronic dynamics of *Ca*ChR1 from 500-900 nm upon photoexcitation. The observed signatures are consistent with the formation of the P_1 intermediate within 110 fs and subsequent vibrational relaxation with a 600 fs time constant. Resonant impulsive vibrational spectroscopy applied to the initial photoreaction of *Ca*ChR1 provided experimental evidence for an ultrafast photoisomerisation of the retinal chromophore from an all-*trans* to a 13-*cis* configuration. Combining low-temperature resonance Raman spectroscopy with actinic-pump-probe impulsive vibrational spectroscopy verified the assignment by revealing the 13-*cis* retinal structure of the P_1 intermediate formed in a vibrationally coherent fashion within 1 ps.

Methods

Sample Preparation

*Ca*ChR1 was cloned, expressed and purified as described previously.[159] An additional gel filtration step was introduced to yield highly purified sample with a ratio of $OD_{280\ nm}/OD_{518\ nm} = 2.5$. The protein was concentrated to 10 mg/mL in an aqueous solution of 100 mM NaCl, 20 mM Hepes, pH 7.4 with 0.03% dodecylmaltoside. The sample was kept in the dark prior to the experiments.

Low-Temperature Resonance Raman Spectroscopy

3 μL concentrated *Ca*ChR1 sample (5-10 mg/mL in 5 mM NaCl, 5 mM Hepes, pH 7.4, 0.05% dodecylmaltoside) was dried on top of a quartz crucible and rehydrated by vapour diffusion of 4.5 μL of a water/glycerol mixture (8/2 w/w) placed nearby the protein film. The sample was cooled down to 80 K with a cryostat (freezing stage TMHS600, Linkam). For the resonance Raman experiment of the ground electronic state of *Ca*ChR1 a krypton ion laser (Innova 90C, Coherent) was used at 647 nm (see Radu *et al*[171] and Nack *et al*[172] for more details on the Raman setup). The spectral resolution of the Raman spectra was 3 cm^{-1}. For photoactivating *Ca*ChR1, an argon ion laser (35 MAP-431-23, Melles Griot) emitting at 502 nm with an intensity of 20 mW was focused on the sample. Raman spectra were recorded in the presence and absence of the photoactivating laser under otherwise identical conditions. The contribution of vibrational modes of ground-state *Ca*ChR1 were interactively subtracted from the Raman spectrum of the photostationary state using the all-*trans* retinal mode at 1165 cm^{-1} to yield a pure Raman spectrum of the P_1 state. The subtraction factor was found to be 0.8.

Ultrafast Spectroscopy

All experiments were carried out using an $OD_{518\ nm} = 10$ sample, flowed through a 200 μm flowcell ($OD_{518\ nm}^{200\ \mu m} = 0.2$) by a peristaltic pump, at a sufficient flow speed to ensure a fresh sample volume for every shot at a laser repetition rate of 2 kHz. All pulses were parallel polarised with respective focus diameters of 34 μm (probe), 75 μm (530 nm, 8 fs, 150 nJ), 65 μm (800 nm, 160 nJ) and 90 μm (515 nm, 200 fs, 50 nJ) at the sample.

Chapter 7

Excited-State Dynamics of wild-type Green Fluorescent Protein

The protein samples used in this work were provided by Giovanni Bassolino. Tullio Scopigno, Giuseppe Fumero and Giovanni Batignani are acknowledged for providing initial theoretical simulation results aiding the interpretation of the 2D Raman data.

7.1 Introduction

Fluorescent marker molecules are imperative tools in biotechnology to monitor and understand processes on a cellular level of living organisms.[173,174] A particularly important marker is the green fluorescent protein (GFP) derived from the jellyfish *aequorea victoria*. It can be expressed in the cell in a variety of mutations, making it highly versatile, and is typically detected using fluorescence microscopy to reveal cellular processes and architectures.[175] Its structure consists of a β-barrel with eleven β-strands surrounding the covalently bound photoactive 4-hydroxybenzylidene-2,3-dimethylimidazolinone chromophore (Figure 7.1a).[173,176,177] Wild-type GFP (wt-GFP) exists in two distinct ground-state configurations: a neutral, protonated A_0 state; and an anionic, deprotonated B_0 state, with absorption maxima at 397 and 480 nm, respectively. Excitation of either state results in pronounced green fluorescence at $\sim$510 nm, with an emission quantum yield of 0.8 in both cases, but with different photodynamics.[174,178] The origin for this behaviour lies in an excited-state proton transfer (ESPT) occurring after photoexcitation of the

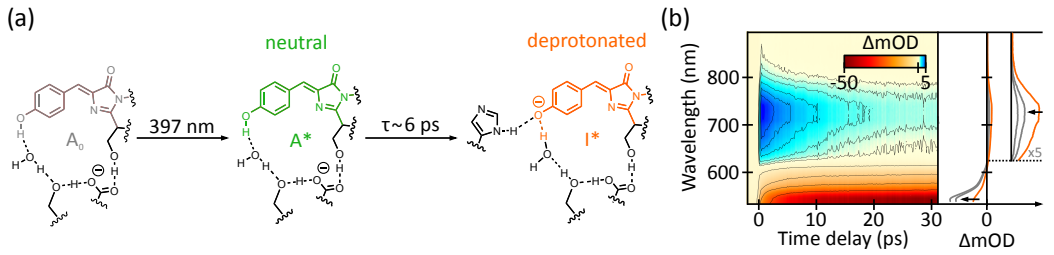

Figure 7.1: Photochemistry of the A state in wt-GFP. (a) Molecular structures involved in the excited-state proton transfer (ESPT) reaction after photoexcitation at 397 nm. Upon absorption of a photon, molecules in the ground electronic state, A_0, are promoted to the first excited electronic state, A^*, and subsequently undergo an ESPT with a time constant of 6 ps to a deprotonated and highly fluorescent I^* state. (b) Transient absorption map of wt-GFP after photoexcitation at 400 nm (250 fs) illustrating the overall photodynamics of the system. Selected transient absorption spectra are displayed on the right with arrows indicating spectral changes as a function of time delay.

neutral A_0 state, which leads to the formation of a fluorescent and deprotonated intermediate, I^*, structurally similar to B^* but with minor modifications in the protein environment.[179,180] The ESPT is believed to originate from the phenol O-H proton, which migrates along a proton wire spanned by a water and an S205 residue toward a carboxy group on the residue E222, which in turn is hydrogen-bonded to the imidazole ring end of the molecule (Figure 7.1a).[181–185] Despite the large number of studies on GFP, the exact underlying structural changes accompanying and leading to the ESPT are not fully understood. In particular the earliest structural changes, which contain the trigger for the ESPT, are rarely examined due to insufficient signal-to-noise ratios or lack of effective time resolutions.[173,186]

Here, we present time-domain excited-state Raman spectra of the A^* and I^* states, and monitor the structural dynamics underlying the $I^* \leftarrow A^*$ transition using actinic-pump-probe impulsive vibrational spectroscopy (APP IVS).[65,85] In addition, high time-resolution (∼15-20 fs) APP IVS is employed to characterise the primary chromophore rearrangements responsible for the ESPT. In combination with a 2D excited-state Raman map, we tentatively assign the directional energy flow occurring in the chromophore after photoexcitation from Franck-Condon (FC) active phenol-ring modes to the phenol C-O stretching mode that releases the proton.

7.2 Results and Discussion

Electronic Dynamics of wt-GFP

We characterise the electronic resonances and system dynamics of wt-GFP using transient absorption spectroscopy employing a 400 nm (250 fs) pump pulse to photoexcite the A_0 state in combination with a broadband (500-900 nm) probe pulse (Figure 7.1b). After photoexcitation, wt-GFP reveals a pronounced stimulated emission (SE) band at 510 nm as well as a weak excited-state absorption (ESA) band centred at 720 nm. The ESA decay is concomitant with the SE growth, and is described by a global mono-exponential time constant of ∼6 ps, which is assigned to the ESPT, in agreement with previous studies.[187,188] The ESA is thus characteristic of the decay of the A^* state, while the SE belongs primarily to the rise of the I^* state.

Structural Evolution of the $I^* \leftarrow A^*$ Transition

The excited-state Fourier transform Raman spectra after photoexcitation at 400 nm (250 fs) and impulsive excitation at 800 nm (9 fs) are illustrated in Figure 7.2a. The spectra were obtained by averaging the probe region over the red edge of the SE band (550-625 nm, Figure 7.1b). The initial spectrum near zero time delay is characterised by modes at 518, 604, 821, 889, 976, 1144, 1177 and 1270 cm^{-1} which evolve into a Raman spectrum (>10 ps) dominated by modes at 518, 604, 821, 889, 976 1144 and 1302 cm^{-1}. The modes at 1144, 1177 and 1270 cm^{-1} show a significant decay, while a single mode at 1302 cm^{-1} gains intensity over time. Modes at 604, 821, 889 and 976 cm^{-1}, on the other hand, display negligible temporal evolution. A global fitting routine with an offset and a mono-exponential function (∼6 ps) is sufficient to describe the observed dynamics, suggesting a single-step conversion from A^* to I^* without intermediates. We assign the early Raman spectrum to the initially excited A^* state and the Raman spectrum at later times (>10 ps) to the fluorescent I^* state, in agreement with the underlying transient absorption features (Figure 7.1b).

A direct comparison of the Raman spectra of A^* and I^* reveals a significant difference in the relative intensity ratio between the modes at 1144 and 1302 cm^{-1} (Figure 7.2b). It was previously shown that the phenol C-O stretching vibration for a protonated A^* state occurs at 1275 cm^{-1}, and blue-shifts upon deprotonation to 1295 cm^{-1} in the I^* state.[189] The mode observed at 1302

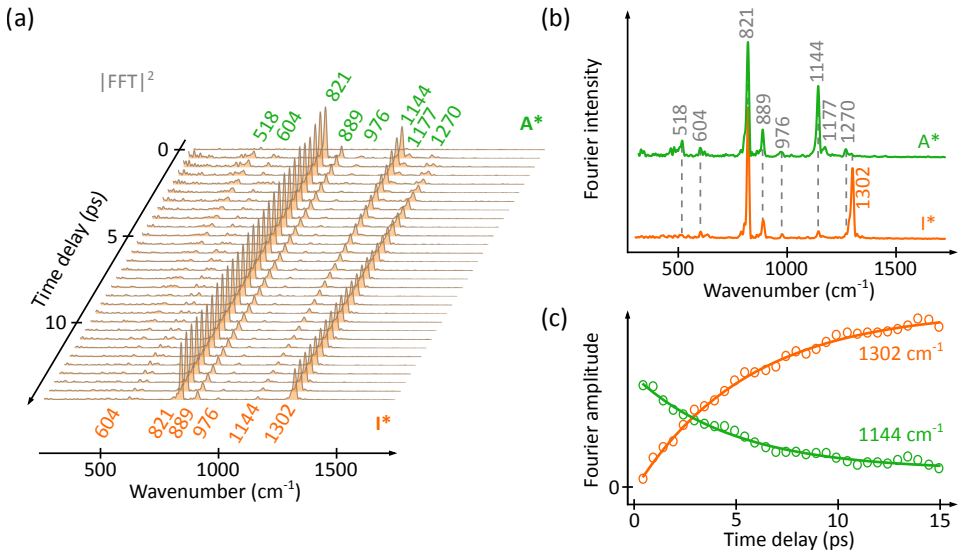

Figure 7.2: ESPT in wt-GFP resolved with APP IVS. (a) Excited-state time-domain Raman spectra recorded as a function of actinic-impulsive pump delay monitoring the ESPT from A* (green) to I* (orange), averaged over the red edge of the SE band (550-625 nm). Photoexcitation at 400 nm (250 fs) was followed by an impulsive pump pulse centred at 800 nm (9 fs). (b) Isolated Raman spectra of the initially excited (A*, green) and fluorescent state (I*, orange). (c) Dynamics of selected excited-state modes (1144/1302 cm^{-1}) monitoring the ESPT. The retrieved exponential time constants (4.8 ps - 1144 cm^{-1}, 5.5 ps - 1302 cm^{-1}) are in excellent agreement with the formation of the fluorescent state obtained transient absorption (6 ps). Note that the Raman amplitude is used to obtain the decay dynamics as the initially recorded vibrational coherence reports directly on the concentration of the available species.

cm^{-1} is therefore assigned to a deprotonated phenol C-O stretching vibration and is a sensitive marker mode for the ESPT. A mono-exponential fit of the corresponding dynamics recovers a time constant of 5.5 ps in agreement with the ESPT time constant derived from transient absorption. These observations validate our earlier structural assignment of the >10 ps Raman spectrum to the deprotonated I* state (Figure 7.2c, orange transient). Consequently, the 1144 cm^{-1} mode (phenol C-H rocking) corresponds to a protonated A* state based on the observed decay time constant of 4.8 ps (Figure 7.2c, green transient).[190,191] The structure of the A* state is initially in a phenol configuration and changes through the ESPT to a quinone-like structure in the I* state by increasing the double-bond character of the phenol C-O bond. This process changes the π-bonding in the phenol ring and affects the phenol C-H rocking mode (1144 cm^{-1}), making it a sensitive marker for the ESPT from the perspective of the reactant (A*), while the phenol C-O stretching mode (1302 cm^{-1}) monitors

the ESPT from the perspective of the product (I^*). The remaining modes (500-1000 cm^{-1}) show negligible temporal evolution and are most likely not crucially involved in the ESPT.[186] Consequently, constant Raman intensity throughout the proton transfer reaction are observed.

Primary Structural Evolution directly after Photoexcitation

To gain insight into the structural changes after photoexcitation, we record excited-state Raman spectra using a short actinic pump pulse centred at 400 nm (13 fs) with otherwise identical pulse settings (Figure 7.3a). Akin to high time-resolution transient absorption spectroscopy, pronounced oscillatory intensity modulations of the exponentially decaying excited-state Raman spectrum appear. Since the actinic pump pulse is short in time it generates vibrational coherence (VC) in the FC region, which subsequently modulates the impulsively generated Raman spectrum. Close inspection reveals that the oscillatory modulations are composed of multiple frequencies, hinting towards a structural origin.

To exclude potential artefacts arising from direct VC generation, we simultaneously record the direct excitation Raman spectrum by blocking the impulsive pump pulse and keeping the Fourier transform parameters (impulsive pump-probe delay, coherence length and window) unaltered (Figure 7.3b). This results in an altered temporal position of the probe window for each time point and generates an experimental sliding-window Fourier transform (SWFT) map.[192] SWFTs are typically employed to detect frequency shifts within a time signal.[88] Here, no frequency shifts and importantly, no pronounced amplitude modulations are found, enabling us to attribute the oscillatory modulations observed in Figure 7.3a to the interaction of the system with both short pulses (actinic and impulsive pump).

Direct impulsive VC generation upon photoexcitation leads to a Raman spectrum that potentially differs from a Raman spectrum derived from VC generation on the excited electronic state. In particular, different FC factors employed in the VC generation step, as well as the topography of the potential energy surface, can alter the relative intensity distributions hugely.[95,99,105] To distinguish between the mechanism of VC generation, we refer to a FC Raman spectrum for impulsive VC generation upon photoexcitation, which can be derived by averaging the first 200 fs of the SWFT map displayed in Figure 7.3b. The frequency content of the FC Raman spectrum (blue) is largely identical to

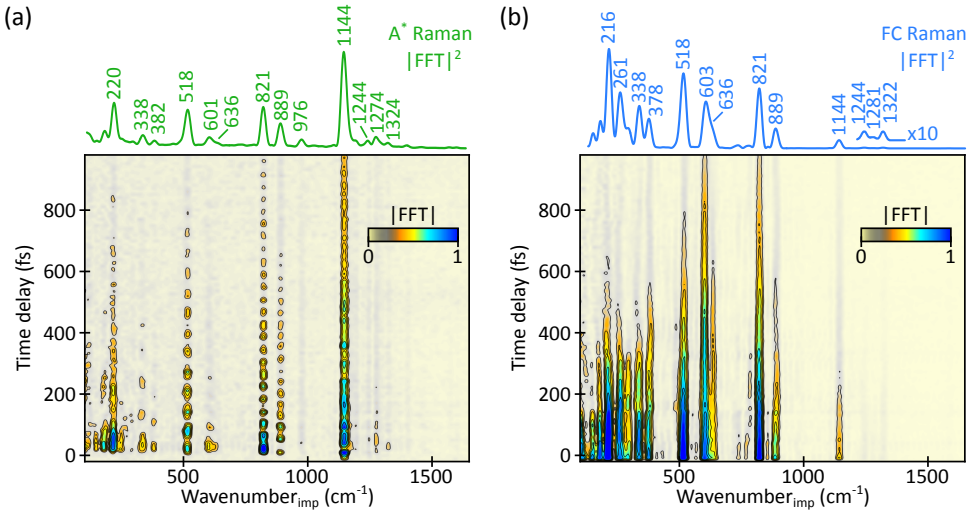

Figure 7.3: High time-resolution APP IVS on wt-GFP. (a) Temporal evolution of the excited-state Raman spectrum within the first picosecond after photoexcitation at 400 nm (13 fs) and impulsive vibrational coherence generation at 800 nm (9 fs). A probe region from 550-625 nm was averaged. The Raman spectrum averaged over the first 200 fs is shown at the top (green). (b) Temporal evolution of the vibrational coherence generated by the actinic pump pulse only, equivalent to an experimental sliding-window Fourier transform. The corresponding Franck-Condon (FC) Raman spectrum is obtained by averaging the first 200 fs and shown on top for comparison. Note the distinct differences between the two spectra in (a) and (b) in particular in the low-frequency region.

the Raman spectrum of the A* state (green) apart from an increased number of peaks in the low-frequency region. The decreased Raman intensities for higher frequency modes in the FC Raman spectrum arise from a lower effective time resolution, as discussed elsewhere.[95,98] The remaining differences in relative intensities as well as the reduced number of A* Raman modes can be accounted for by different Raman cross sections involved in the VC generation processes. For the A* state Raman spectrum, we generate VC via the ESA ($S_2 \leftarrow S_1$) at 800 nm, while in the FC Raman spectrum, the VC is generated via the ground-state absorption ($S_1 \leftarrow S_0$) at 400 nm.

2D Excited-State Raman Map of wt-GFP

The frequency content of the oscillations modulating the A* Raman spectrum is obtained by subtracting the slowly varying exponential dynamics and Fourier transforming the resulting oscillations, which gives rise to a 2D Raman map (Figure 7.4a). We find pronounced diagonal peaks and a range of less intense cross peaks, asymmetrically arranged around the diagonal, contrary to what is

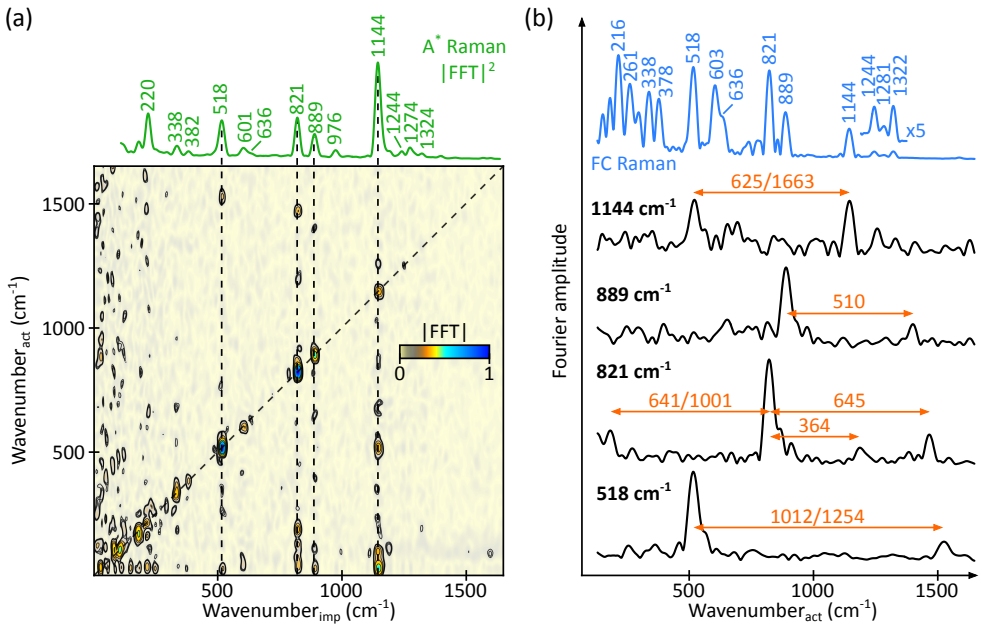

Figure 7.4: 2D Raman map of wt-GFP derived from high time-resolution APP IVS. (a) 2D Raman map obtained after Fourier transformation along the actinic-impulsive time delay of the data presented in Figure 7.3a. The excited-state Raman spectrum is shown at the top (green) for comparison. (b) Vertical cuts along the major excited-state modes (bold, grey dashed vertical lines in (a)) compared to the FC Raman amplitude spectrum (blue). Numbers indicate frequency differences between the diagonal peak and the observed cross peaks. The first number denotes direct subtraction, while the second number accounts for Fourier artefacts due to an insufficient sampling frequency and is given for frequencies which can be resolved by the effective time resolution of the experiment of ∼20 fs.

obtained for 2D NMR or 2D IR.[35] Cross peaks appear only along vertical lines coincident with the most intense A* Raman modes. In addition, the observed peaks (cross and diagonal) are elongated along the actinic frequency axis.

To gain an understanding of the involved frequencies, we extract the actinic Raman spectrum along the major A* Raman modes (Figure 7.4a, dashed lines) and compute the frequency differences with respect to the diagonal peaks (Figure 7.4b). This analysis is motivated by a preliminary theoretical description of the underlying signal pathways (see below). It has to be taken into account that the experiment presented was carried out at an actinic time step of 10 fs, limiting the Nyquist frequency to ∼1650 cm^{-1}. Frequencies higher than the Nyquist frequency will not be correctly displayed but can still appear in the 2D map. This can lead to incorrect frequency difference values and requires the additional computation of peak differences taking undersampling into account (second number). In addition, it must be kept in mind that the

origin of the modulations of the Raman spectrum lies in the VC generated by the actinic pump pulse. The visibility of the resulting oscillations is dependent on the effective time resolution of ∼20 fs due to group-velocity dispersion.[95,98] Nominal frequencies >1700 cm^{-1} are thus unlikely to be resolved in this experiment, significantly reducing the number of difference frequency peaks (Figure 7.4b). The obtained frequency differences are best compared to the FC Raman spectrum (blue) since the origin for cross peaks lies in the VC generation by the actinic pump pulse. We find matching frequencies close to 518, 636 and 1281±25 cm^{-1}, which can be approximately assigned to skeletal in-plane phenol-ring deformations (518 and 636 cm^{-1}) and the phenol C-O stretching vibration (1281 cm^{-1}).[189,193] Based on this analysis, we assign cross peaks between the following modes:

515 cm^{-1}	→	1281 cm^{-1}	:	ph ring def.	→	ph C-O str.
821 cm^{-1}	→	1281 cm^{-1}	:	ph ring def.	→	ph C-O str.
821 cm^{-1}	→	643 cm^{-1}	:	ph ring def.	→	ph ring def.
889 cm^{-1}	→	518 cm^{-1}	:	ph C-H rock.	→	ph ring def.
1144 cm^{-1}	→	643 cm^{-1}	:	ph C-H rock.	→	ph ring def.

Importantly, all cross peaks appear to be concentrated on the phenol (ph) ring that releases the proton for the ESPT.

Short Theoretical Description of Excited-State 2D APP IVS

The 2D Raman map presented in Figure 7.4a arises from five electric field interactions: two actinic, two impulsive pump and one probe electric field, giving rise to a fifth-order polarisation in the sample. In this scheme, the actinic pump pulse generates an excited-state vibrational wavepacket, composed of FC-allowed excited-state vibrational modes. The subsequent interaction with the impulsive pump fields modifies this vibrational wavepacket by impulsive excitation into another Raman-allowed mode, and the probe pulse reads out the resulting oscillating wavepacket by returning the system to a population state (Figure 7.5a). In the harmonic limit (assuming for simplicity a high- and a low-frequency mode, v_H and v_L), this leads to signals oscillating at v_H and v_L (diagonal peaks) as well as $v_H + v_L$ and $v_H - v_L$ (cross peaks).

In contrast to traditional 2D Raman techniques, investigating ground electronic states,[194–197] we resolve only pathways which consist of two consecutive optically-allowed one-photon transitions with significant intensity. These pathways become possible due to the initial electronic excitation, which is not subject

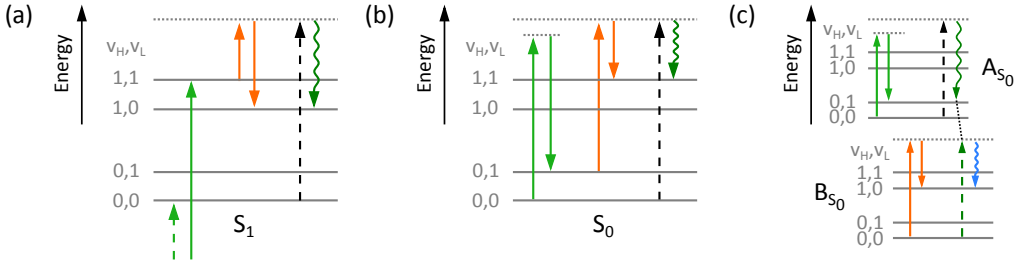

Figure 7.5: Selected wave-mixing energy ladder diagrams for different 2D Raman pathways giving rise to a sum-frequency cross peak at $v_H + v_L$. (a) Excited-state 2D Raman pathway generating a double-quantum coherence upon electronic excitation followed by a sequence of one-photon transitions to emit the signal field. (b) Ground-state 2D Raman generating a single-quantum coherence with the actinic pulse followed by another single-quantum impulsive transition, requiring a double-quantum transition to produce the signal field. (c) Parallel cascade arising in two molecules. Molecule A provides a third-order signal through the actinic and probe pulse, which is used as a probe field in molecule B after the impulsive pump has interacted, producing another third-order signal field. Light green - actinic pump, orange - impulsive pump, black - probe, dark green/blue - signal.

to the selection rule, $\Delta v \pm 1$. This significantly limits the number of possible Liouville pathways in our approach, increases the observed overall intensities, and explains the sparse appearance of the 2D Raman map. Ground-state 2D Raman techniques, on the other hand, rely on a weak two-photon transition for the emitted signal field, drastically reducing the observed intensities (Figure 7.5b).

The relative intensity of the peaks depends on the FC factors for generating the initial VC as well as the transition dipole moments coupling two excited-state vibrational modes via the impulsive pump pulse. In addition, lineshapes (and hence intensities) are affected by dynamic processes leading to fast vibrational dephasing. The latter leads to a uni-directional linewidth broadening of the peak and all corresponding cross peaks.

In the harmonic limit, we expect cross peaks to appear at an exact excited-state Raman frequency. If this approximation is relaxed to account for anharmonic potentials, as appropriate for photoreactions, slight variations in the actual peak frequency can occur, which provide an understanding of the anharmonic curvature of the underlying potential energy surface. Depending on the system, these can be significantly larger than in the ground electronic state. The presented 2D Raman map thus contains a wealth of information sensitive to the exact nature of the potential energy surface. Our 2D Raman

spectroscopy approach differs in this respect intrinsically from other 2D techniques which detect coupling between modes directly as a cross peak, rather than a sum-/difference-frequency peak.[35,197]

2D Raman spectroscopy typically suffers from strong contaminating cascading signals (Figure 7.5c). Briefly, a Raman cascade can be generated by two third-order interactions in two different molecules where the emitted third-order signal from the first molecule (A) triggers a second third-order interaction in another molecule (B). This leads to an emitted signal field which appears at the same frequency as a fifth-order signal. Such third-order cascade processes are significantly more intense compared to the desired fifth-order signals which complicates their interpretation.[194,195] It was only recently that the problem of cascading signals in the ground electronic state was solved using a sophisticated pulse-shaping scheme.[197] Our 2D Raman technique, however, is less susceptible to cascading peaks, since only optically-allowed one-photon transitions are operating and the excited-state concentrations are low. It has to be evaluated how other effects, such as polarisation beating, can lead to artefact cross peaks.[198]

Interpretation of the Excited-State 2D Raman Map for wt-GFP

This theoretical framework allows us to interpret the observed features in wt-GFP (Figure 7.4). The asymmetric lineshapes observed with an elongation along the actinic frequency axis point to a rapidly dephasing initially prepared structure. This is in line with the underlying ESPT changing the chromophore structure from the A^* to the I^* state, as also found in transient absorption spectroscopy (Figure 7.2a). Furthermore, absorption of a photon in this system leads to a $\pi^* \leftarrow \pi$ transition of the conjugated system, and primarily excites phenol-ring modes.[193,199] Taking into account the large variations in cross peaks observed earlier (± 25 cm^{-1}), we propose large anharmonicity constants in the initially excited phenol-ring modes, suggesting the possibility of a directional energy flow.

In particular the latter observation allows for mechanistic insight in the primary structural motions occurring after photoexcitation (Figure 7.6). Our results point towards cooperative vibrational motion of several phenol-ring modes to provide enough vibrational energy for the phenol C-O stretch required to detach the proton. Consequently, the phenol ring adopts a quinone-like ring structure as a result of the electronic excitation changing the π bonding situation of the conjugated system and in particular the phenol ring. We stress,

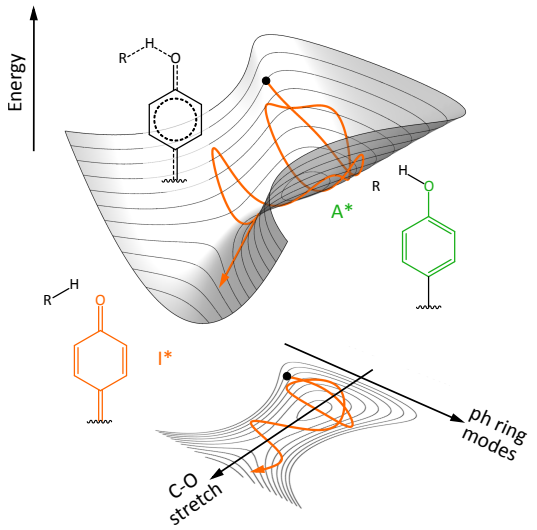

Figure 7.6: Proposed mechanism for the ESPT in wt-GFP after photoexcitation at 397 nm. The system is photoexcited into the FC region (black point) and subsequently evolves according to the underlying potential energy surface (orange trajectory). Initially, mainly phenol-ring modes are active in the A* state (green). Due to anharmonic coupling between phenol-ring modes and the C-O stretching mode, the C-O bond develops double-bond character (black) which results in the release of the proton and the formation of a quinone-like I* structure (orange).

however, that such an interpretation requires more theoretical and experimental studies to confirm this hypothesis. In particular an in-depth analysis of the observed intensity distribution in the 2D Raman map is likely to reveal a large amount of additional information for the initial steps after photoexcitation.

7.3 Conclusion

We have presented time-domain actinic-pump-probe impulsive vibrational spectroscopy (APP IVS) to reveal the structural characteristics of wt-GFP in the A* and I* states. In addition we monitored the underlying ESPT with structural sensitivity and revealed important marker modes for both states to be the phenol C-O stretching (I*) and phenol C-H rocking (A*) mode. By reducing the pulse duration of the actinic pump pulse we were able to extend our study to investigate the earliest structural movements after absorption of a photon and recorded a 2D excited-state Raman map. The observations suggest a cooperative effect between phenol-ring modes to direct excitation energy via anharmonic coupling to the phenol C-O stretching vibration. which in turn starts the ESPT.

Apart from the detailed mechanistic interpretation, we presented to our knowledge the first 2D Raman map on the excited electronic state recorded in the time domain. The data obtained are similar to the more recently developed frequency-domain 2D FSRS technique.[110,111] Both techniques, however, differ in the analysis and interpretation of the signals involved. At this stage, a thorough theoretical framework has to be developed to devise a more sophisticated route to extract the information content accessible with this new technique.

Methods

All experiments were carried out using an $OD_{397\,nm} = 9$ sample flowed through a 200 μm flowcell ($OD_{397\,nm}^{200\,\mu m} = 0.18$) at a laser repetition rate of 10 kHz. A peristaltic pump ensured sufficient sample replenishment during consecutive shots. The low time-resolution experiment (Figure 7.1b and 7.2) employed actinic (400 nm, 250 fs) and impulsive (800 nm, 9 fs) pulses of 80 and 320 nJ focussed to a diameter of 80 and 60 μm at the sample, while the probe was adjusted to a focus diameter of 41 μm. The pulse energies in the high time-resolution APP IVS experiment (Figure 7.3 and 7.4) were set to 150 and 160 nJ for the actinic and impulsive pump pulses with a focus diameter at the sample of 85 and 55 μm and a 34 μm probe diameter. In both experiments the probe was stepped in intervals of 5.4 fs.

Chapter 8

Excited-State Dynamics of all-*trans* Retinal Protonated Schiff Base in Methanol

All-*trans* n-butyl retinal protonated Schiff base (RPSB) samples studied in this work were provided by Giovanni Bassolino.

8.1 Introduction

Proton transfer across membranes is a crucial means for cells to convert energy in the form of a proton gradient into chemical energy. The purple membrane protein bacteriorhodopsin (bR), with its chromophore all-*trans* RPSB, realises proton transfer by absorbing light at 560 nm and initiating a photoisomerisation reaction to 13-*cis* RPSB.[113,200,201] Due to its high isomerisation quantum yield (0.64) and ultrafast dynamics (500 fs), bR has become a hallmark for efficient photochemistry.[129,202] In contrast to the protein environment, the chromophore all-*trans* RPSB in methanol solution shows a significantly blue-shifted absorption spectrum (445 nm), slower dynamics (5 ps) and a lower isomerisation quantum yield (0.1) with a different main photoproduct (11-*cis*).[149,203,204] Despite such drastic differences, the overall potential energy surfaces are similar, featuring an excited-state barrier along the isomerisation reaction coordinate (Figure 8.1).[98,141,205]

In bR, recent studies have proposed anharmonic coupling between Franck-Condon (FC) active modes and excited-state modes to yield a partially twisted 13-*cis* structure of the chromophore.[98] A series of time-resolved Raman spectra on the excited electronic state is, however, still missing due to experimen-

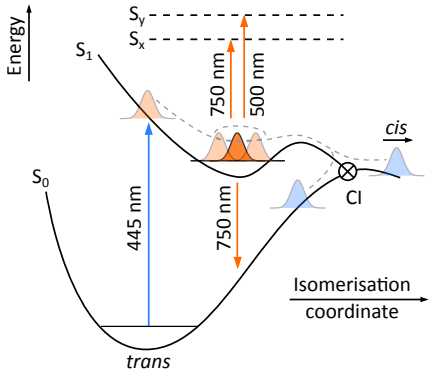

Figure 8.1: Photochemistry of all-*trans* RPSB in methanol. Potential energy surface illustrating the evolution of an excited-state population along the isomerisation coordinate via a conical intersection (CI). Populations are coloured according to their absorption properties: Orange - ∼750/500 nm, blue - ∼445 nm. Vertical arrows indicate the main electronic transitions at indicated wavelengths.

tal difficulties with the highly scattering protein. On the other hand, the chromophore in solution shows no such difficulties and is ideally suited to be investigated by techniques capable of extracting high-quality excited-state Raman spectra which can subsequently be related to bR. The excited-state structure for all-*trans* RPSB in solution has been proposed to be twisted around the C_{11}=C_{12} bond resulting from partial bond-length alternation of the backbone in combination with out-of-plane hydrogen motions.[206,207] Experimental insights confirm this picture, but only limited studies are available related to the conformational changes occurring directly after photoexcitation.[114,208,209] In particular competing ground-state signals are commonly preventing a complete interpretation.

To characterise the structural features of the excited electronic state, we apply background- and baseline-free pump-dump-probe and population-controlled impulsive vibrational spectroscopy (PDP IVS and PC-IVS) to all-*trans* RPSB in methanol solution.[65,85] We find that photoexcitation leads to a rapid formation of a twisted chromophore structure mediated along a number of low-frequency modes, and yields strong activity from hydrogen out-of-plane (HOOP) modes, as reported for bR,[98] in agreement with previous results.[114,209] By employing highly time-resolved PC-IVS (∼15-20 fs) we explore the initial structural changes occurring directly after photoexcitation (<1 ps) and provide for the first time a 2D Raman map pointing towards anharmonic coupling between HOOP modes and low-frequency modes. The results provide a picture about the energy flow in the system after photoexcitation until a relaxed excited-

state structure is reached, and give preliminary quantitative insights into the structural changes occurring after photoexcitation in the protein environment in bR.

8.2 Results and Discussion

8.2.1 Franck-Condon Raman Spectrum from PDP IVS

Photodynamics of all-*trans* RPSB at 520 nm

The transient absorption map of all-*trans* RPSB in methanol after photoexcitation at the red edge of the absorption spectrum with a pump pulse centred at 520 nm (9 fs) is shown in Figure 8.2a (top). The dominant spectral feature is a broad stimulated emission (SE) band centred at ∼750 nm which is superimposed by a weaker excited-state absorption (ESA, 750 nm) band leading to a double-hump spectral shape (Figure 8.1b). At bluer probe wavelengths, an additional ESA band appears at ∼500 nm. A global fitting routine with 2 exponential functions and an offset retrieves decay constants of 2 and 7 ps, in agreement with previous studies.[109,148,149]

Application of a dump pulse (800 nm, 200 fs) 100 fs after the pump pulse depletes ∼30% of the excited-state population via the $S_0 \leftarrow S_1$ transition and results in an overall drop in the SE intensity (Figure 8.2a, middle). Upon computation of the difference map (dump OFF-ON)[65] we recover a negative signal of similar shape to the transient absorption map, illustrating mainly the reduced S_1 population after interaction with the dump pulse. The corresponding temporal profile is characterised by a dump-pulse-limited rise followed by an exponential decay of ∼5 ps in agreement with the unperturbed transient absorption data. The spectral region around the ESA at 500 nm, however, appears significantly altered upon dumping. The most likely origin is the population of a vibrationally hot ground electronic state through the dump pulse, which induces a red-shifted bleach signal and consequently leads to a reduced ESA due to spectral overlap. Tuning the centre wavelength of the dump across the SE from 800-1200 nm did not impact the dynamics.

Characterisation of Excited-State Vibrational Coherences

The transient absorption maps exhibit pronounced oscillatory modulations throughout the probe window arising from the impulsive generation of vibra-

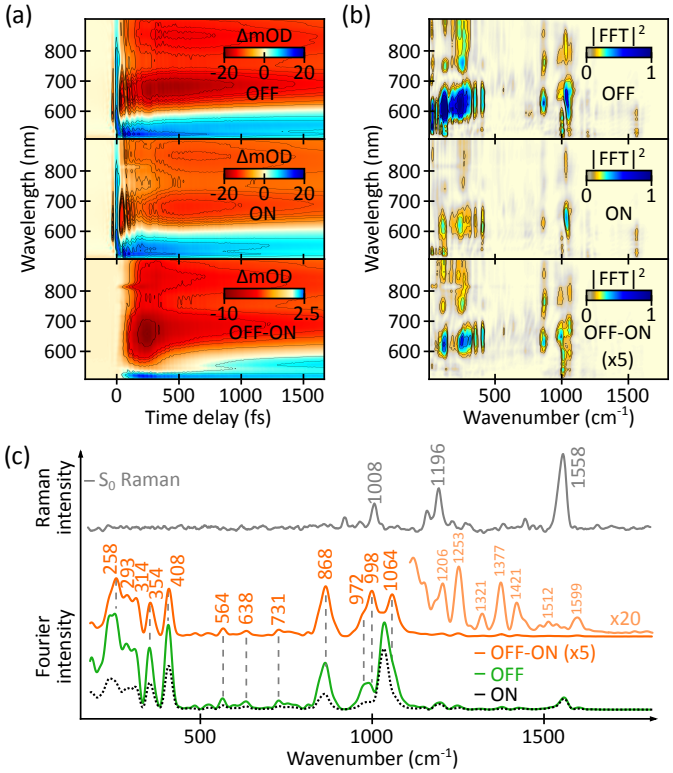

Figure 8.2: PDP IVS spectra of all-*trans* RPSB in methanol. (a) Transient absorption maps in the absence (OFF, top) and presence (ON, middle) of the dump pulse compared to the subtracted OFF-ON trace (bottom) showing the effect of an 800 nm (200 fs) dump pulse 150 fs after the impulsive excitation pulse (520 nm, 12 fs). (b) Fourier power maps of the respective experiments. We note the striking similarity between OFF and OFF-ON, suggesting efficient generation of excited-state VC. (c) Spectral average over the blue edge of the SE band (580-690 nm) compared to the ground-state Raman spectrum. The S_0 Raman spectrum was provided by Torsten Wende.

tional coherence (VC) by the short pump pulse.[47,48] We truncate the maps to cover time delays starting at +150 fs and subtract the slowly varying electronic dynamic by means of a global exponential fitting routine with an offset and two exponential functions. Fourier transformation of the residual VC reveals the wavelength-resolved Raman spectrum for each map (Figure 8.2b). The unperturbed Fourier power map (top) shows pronounced coherence activity in the low-frequency region (<500 cm^{-1}) as well as in the HOOP and methyl rocking region (800-1100 cm^{-1}). Each mode has a characteristic node at ∼700 nm, slightly blue-shifted compared to the SE maximum, suggesting that the observed modes correspond to the excited electronic state.[133] Towards bluer wavelengths, we observe an additional weaker mode at 1560 cm^{-1} which we assign to the ground electronic state due to the lack of a characteristic nodal

behaviour. The Fourier power map obtained under dumped conditions (middle) shows a similar pattern, but with reduced intensity in the assigned excited-state modes, as expected. The mode at 1560 cm^{-1}, however, appears unaffected and shows no residual intensity in the OFF-ON Fourier map (bottom), supporting assignment to S_0.

A spectral comparison over the blue edge of the SE band (580-690 nm, Figure 8.2c) highlights excited-state modes in the low-frequency region (<500 cm^{-1}), as well as in the HOOP and methyl rocking region (800-1100 cm^{-1}). Modes with less intensity can be found in the torsional region of the spectrum (500-700 cm^{-1}) and at higher frequencies (>1200 cm^{-1}). We assign all bands in the OFF-ON spectrum (orange) to the Raman spectrum of the first excited electronic state, due to the distinctly different appearance compared to the ground-state Raman spectrum, which is dominated by modes at 1008, 1196 and 1558 cm^{-1}, and to their wavelength dependence.

Discussion

The results provide initial information about the energy flow after photoexcitation, similar to previous observations in bR.[98] Optical excitation primarily excites methyl rocking (1008 cm^{-1}), C-C (1196 cm^{-1}) and C=C (1558 cm^{-1}) stretching motion in the FC region.[210] PDP IVS, on the other hand, records the VC of the bound and vibrationally hot excited-state plateau structure. The distinct shift from in-plane stretching modes to HOOP as well as methyl rocking modes and an increase in the torsional activity in the excited electronic state point towards a structural distortion occurring during vibrational relaxation. In particular the mode at 868 cm^{-1} is reminiscent of the C_{10}-H and C_{12}-H out-of-plane motions found in the highly twisted all-*trans* retinal chromophore in bathorhodopsin.[130] The excited-state plateau is thus most likely characterised by a twisted all-*trans* backbone structure along the C_{11}=C_{12} bond, explaining the predominant photoproduct 11-*cis*. The current results, however, do not allow to quantify the mechanism of energy transfer from initially excited FC-active to excited-state modes.

We remark that the Raman spectrum obtained by direct impulsive photoexcitation reports on the VC generated in the FC region via the $S_1 \leftarrow S_0$ transition which is detected in a bound electronic state after initial electronic and structural relaxation processes. The detected VC can therefore be affected by anharmonic couplings and conical intersections, which are known to alter the

appearance of the retrieved Raman spectrum.[95,98,106,114,211] We thus distinguish between a FC Raman spectrum (direct excitation) and an excited-state Raman spectrum which is obtained by generating VC directly on the excited electronic state, thus eliminating distortions arising from a dynamic evolution of the VC.

8.2.2 Excited-State Raman Spectrum from PC-IVS

Vibronic Photodynamics of all-*trans* RPSB at 400 nm

To characterise the excited-state Raman spectrum and its temporal evolution we employ PC-IVS. We use an actinic pump pulse centred at 400 nm (25 fs) to excite the system in combination with an impulsive pump pulse at 590 nm (11 fs) for VC generation and a 1030 nm (200 fs) dump pulse (Figure 8.3a).[65] In contrast to the PDP IVS study discussed above, the excitation pulse is centred at 400 nm, which provides the system with more initial energy in the FC region. The transient absorption map after photoexcitation at 400 nm (Figure 8.3a) is, however, overall similar to photoexcitation to that for 520 nm (Figure 8.2a), apart from differences in the relative intensity ratio between the SE and the ESA at 500 nm.[109] In addition, early time delays show a very broad ESA which rapidly cools to 500 nm within 200 fs. We point out that this cooling process is more pronounced in comparison to photoexcitation at 520 nm.

The extracted PC-IVS Fourier Raman spectra (averaged probe region from 580-690 nm, Figure 8.3b, green) at selected actinic-impulsive time delays show pronounced activity in the HOOP and methyl rocking region (800-1100 cm^{-1}), as observed in PDP IVS. The associated dynamics are equivalent to the transient absorption kinetics observed in this region with a time constant of $\sim$6 ps. Interestingly, the low-frequency region shows significant coherence activity only at the earliest time delays with a dynamic evolution comparable to the fast $<$200 fs component found in transient absorption (Figure 8.3a). This behaviour is in agreement with an internal heat sink composed of low-frequency modes to allow relaxation out of the FC region.[169] A more temporally refined study will be presented in the next section to address the role of these modes in the initial vibrational relaxation process in more detail.

Pump-Resonance Dependence in PC-IVS at ΔT = 400 fs

PC-IVS benefits from resonance enhancement, making it crucial to investigate the resonance dependence on the impulsive pump pulse in the extracted Raman

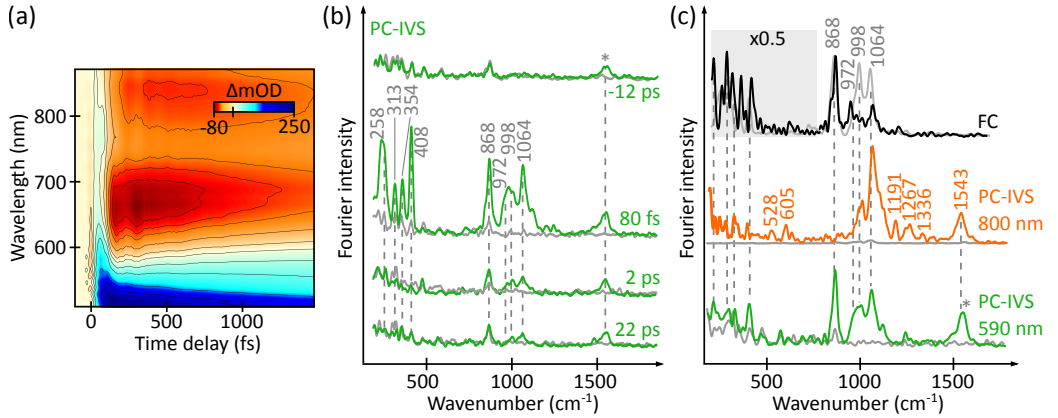

Figure 8.3: PC-IVS spectra of all-*trans* RPSB in methanol. (a) Transient absorption map after photoexcitation at 400 nm (25 fs). (b) PC-IVS spectra (green) and leakage (grey) obtained at various actinic-impulsive time delays (averaged from 580-690 nm). The actinic (25 fs) and impulsive (11 fs) pulses were centred at 400 nm and 590 nm and a dump pulse at 1030 nm (200 fs) was employed 150 fs after the impulsive excitation. Direct excitation by the impulsive pump pulse was adjusted to 8 mOD (<1%) to avoid impulsive excited-state VC generation. Pronounced leakage modes are marked by an asterisk (*). (b) Comparison of PC-IVS spectra at ΔT = 400 fs recorded with an impulsive pump pulse centred at 590 nm (green) and 800 nm (orange) with the FC Raman spectra obtained at 520 nm (12 fs, grey) and 400 nm (13 fs, black).

spectrum in order to obtain a complete picture of the structural features present on the excited electronic state. To this end, we carried out an additional PC-IVS experiment using an actinic pump at 400 nm (250 fs) in combination with an impulsive pump pulse centred at 800 nm (8 fs, Figure 8.3c, orange).[65] While the 800 nm PC-IVS Raman spectrum shows pronounced activity in the HOOP region, no mode is detected at 868 cm^{-1}. On the other hand, we observe new modes at 528, 605, 1191, 1267, 1336 and 1543 cm^{-1} which are not present in the 590 nm PC-IVS spectrum (Figure 8.3c, green). The latter (C=C stretching mode) is most likely also present in the 590 nm PC-IVS Raman spectrum, but masked by ground-state leakage arising from direct excitation by the impulsive pump.

The chosen probe region (580-690 nm) lies at the high-energy side of the SE, which partially overlaps with the ESA centred at 500 nm. Consequently, the probe pulse is sensitive to both transitions and reveals vibrational signatures associated with both transitions as long as VC is generated in all relevant modes. The differences in Raman spectra are thus most likely due to the different resonance conditions employed by the impulsive pump pulse. In the

case of the 800 nm PC-IVS experiment, we impulsively excite via the SE, while in the 590 nm PC-IVS experiment VC is generated via both, the SE and the ESA centred at 500 nm. A combination of both spectra hence reveals the complete set of normal modes of the excited electronic state, characterised by C=C stretch, torsional, HOOP and methyl rocking motions.

Discussion

A comparison of the PC-IVS derived Raman spectra to the FC Raman spectra (Figure 8.3c, grey/black) reveals that the frequency content in the high-frequency region (800-1100 cm^{-1}) of the spectrum is largely identical. Relative intensity differences arise most likely from the different electronic transition employed for VC generation. We can thus verify our earlier structural assignment of a twisted all-*trans* excited-state structure based on the appearance of the HOOP and methyl rocking modes in the region from 800-1100 cm^{-1}. The appearance of local torsional modes (528 and 605 cm^{-1}) in the PC-IVS Raman spectrum adds further support. Low-frequency modes are, however, significantly more intense in the FC Raman spectrum. This observation is in line with the rapid temporal decay found for low-frequency modes (Figure 8.3b), suggesting that low-frequency modes are strongly involved in the initial relaxation process out of the planar FC region to the twisted excited-state plateau structure. We furthermore identify a C=C stretching mode at 1543 cm^{-1} in the excited electronic state using PC-IVS, which is absent in the FC Raman spectra, most likely due to a fast dephasing time.[114] A possible origin is strong anharmonic coupling to other excited-state modes leading to a drastically reduced lifetime of the C=C stretching mode.[212] In this model, the initially excited C=C stretching mode provides the necessary energy for out-of-plane and low-frequency modes to rapidly form a twisted excited-state structure via bond-length alternation.[206]

8.2.3 Structural Dynamics directly after Excitation

Key Excited-State Raman Spectra

The fast decay dynamics of the low-frequency region calls for a more refined structural characterisation of the initial relaxation dynamics. We thus perform high time-resolution PC-IVS with an actinic pump pulse centred at 400 nm (13 fs) and otherwise equivalent pulse settings as employed in the 590 nm PC-IVS

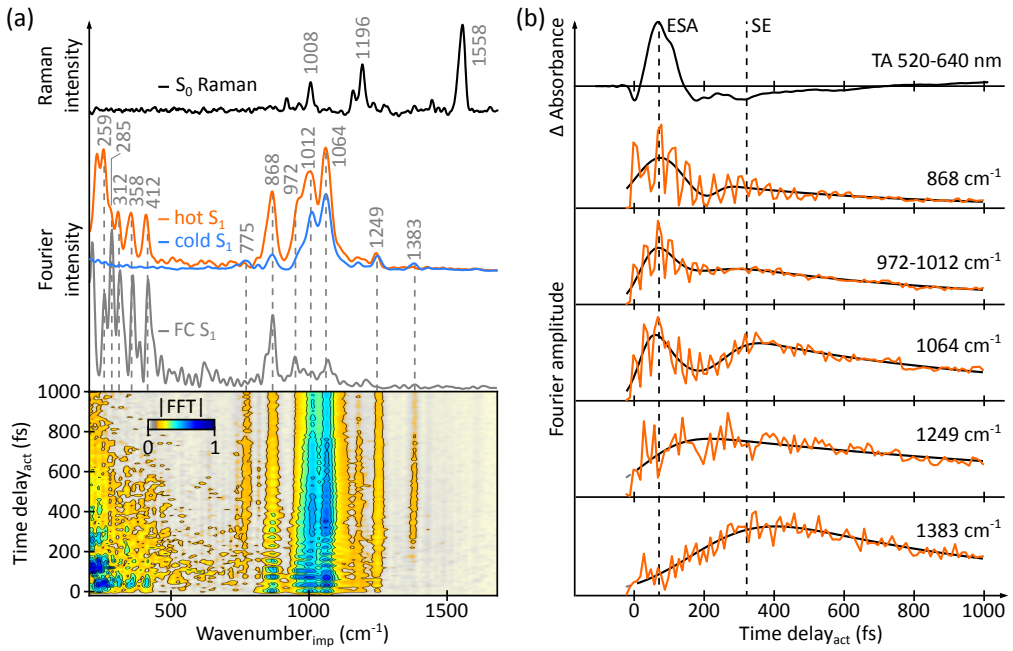

Figure 8.4: High time-resolution PC-IVS on all-*trans* RPSB in methanol. (a) Temporal evolution (bottom) of the excited-state Raman spectrum obtained by PC-IVS averaged over the blue side of the SE (580-690 nm) compared to the ground-state Raman spectrum (black) and the actinic direct excitation spectrum (FC spectrum, grey). Hot (orange) and cold (blue) excited-state Raman spectra are obtained by averaging early (0-100 fs) and late (900-1000 fs) time delays. (b) Temporal profiles of selected high-frequency modes (orange) showing clear oscillatory modulations and mode-specific dynamics. The observed dynamics (black) are related to the transient absorption signal (TA, black) averaged over the impulsive pump spectrum. Vertical dashed lines mark extreme points in the electronic resonance averaged over the pump pulse spectrum. Actinic pump - 400 nm (13 fs), impulsive pump - 590 nm (9 fs), dump - 1030 nm (200 fs).

experiment (Figure 8.4a, bottom). In analogy to our previous observations, we find pronounced activity in the HOOP, methyl rocking and low-frequency region. The low-frequency modes in particular decay extremely quickly within 1 ps. In contrast, high-frequency modes show overall well defined decay profiles, in line with our earlier observations (Figure 8.3b).

By averaging the first and last hundred femtoseconds of the time-resolved Raman map we obtain vibrationally hot and cold excited-state Raman spectra resembling the aforementioned dynamic evolution (Figure 8.4a, orange and blue spectrum). In particular low-frequency modes (<500 cm^{-1}) and the 868 cm^{-1} mode exhibit a drastic intensity reduction, in line with a structural modification along the backbone and the formation of a locally twisted C_{11}=C_{12} bond. Interestingly, the cold Raman spectrum shows the appearance of modes

at 775 and 1383 cm^{-1} which arise from a shifted resonance condition for the impulsive pump pulse from an initially pure ESA resonance to a mixture of SE and ESA resonances (see below, Figure 8.3a).

Comparing the PC-IVS spectrum to the corresponding FC Raman spectrum (grey) shows generally a good agreement in the low-frequency region with the hot excited-state Raman spectrum, while we find small relative intensity differences in the HOOP and methyl rocking region. This can be accounted for by the different relative time resolution for the FC Raman spectrum (∼25 fs due to group-velocity dispersion) which underestimates the intensity of high-frequency modes compared to the PC-IVS experiment (time resolution ∼10 fs). In addition, the spectrum is affected by differences in resonance conditions between the actinic and the impulsive pump pulse with respect to the generation of VC.[95,98]

Temporal Characteristics of Excited-State Modes

The temporal evolution of selected high-frequency modes (Figure 8.4b, green transients) is mode-specific, with initially rapidly decaying modes (868, 963-1012 cm^{-1}), and completely new modes growing in at a delayed time (1249, 1383 cm^{-1}), in addition to slowly decaying modes (1012, 1064 cm^{-1}). The overall decay is biphasic and can be explained by the resonance changes of the system with respect to the pump pulse (8.4b, black transient). A first maximum appears for early PC-IVS spectra giving rise to high Raman intensities, because of strong resonance enhancement by the initial ESA. The second maximum at ∼300 fs corresponds to the rise of the SE, which subsequently decays with the excited-state lifetime. The appearance and disappearance of modes is thus intimately connected to the resonance conditions for VC generation and reports on the formation of a relaxed excited-state structure marked by the SE, as most clearly seen at 1383 cm^{-1} where no ESA enhancement is observed. We remark that the VC generated by the impulsive pump pulse is always detected in the bound excited electronic state. The temporal evolution of the system is therefore resolved by the action of the impulsive pump pulse which translates into relative amplitude changes as a function of actinic-impulsive pump time delay.

Photoexcitation at 400 nm (absorption maximum 445 nm) places the photoexcited molecule in a vibrationally hot excited electronic state, equivalent to a temperature of ∼4000 K or an excess energy of ∼2700 cm^{-1}. The system

subsequently undergoes vibrational relaxation within ∼1 ps by dissipating the excess excitation energy into internal vibrational motion. This is achieved by participation of low-frequency modes which are in a very anharmonic potential in the FC region.[169] Consequently, efficient mode-to-mode vibrational coupling and energy transfer can occur between the modes to quickly relax the system to the potential energy minimum. The shorter lifetimes observed for low-frequency modes closer to 500 cm^{-1} illustrates that the energy is rapidly funnelled into lower low-frequency modes. The low-frequency modes thus act as an internal heat-sink which can dissipate the excess energy to the surroundings over a longer time period, thus explaining the exceptionally high coherence activity at early time delays. In addition, low-frequency modes additionally adjust the backbone structure during this relaxation as shown by the low-energy FC Raman spectrum where limited internal heat dissipation is required (Figure 8.2c).

High-frequency modes, on the other hand, are moderately anharmonic in the FC region. Consequently, their temporal evolution reports more clearly on the overall dynamic processes of the system out of the FC region. This evolution is encoded in the Raman intensities, and subject to changes in the resonance conditions with respect to the impulsive pump pulse. The change in intensities in the Raman spectrum can thus be directly correlated to the structural evolution of the system. For example, the rapid decay of the 868 cm^{-1} mode compared to the other HOOP modes suggests strong torsional activity along the C_{11}=C_{12} bond out of the FC region.

Discussion

These observations point to a mechanistic scenario in which the initially excited modes (1008, 1196 and 1558 cm^{-1}, see S_0 resonance Raman spectrum) rapidly internally distribute the excitation energy upon leaving the FC region into low-frequency modes, which themselves are coupled to local torsional and HOOP modes. Subsequently, the stationary plateau structure is formed within ∼300 fs, as evident by the second maximum in the mode-specific dynamics associated with the SE and thus the relaxed excited-state structure. Importantly, the 868 cm^{-1} mode is a crucial marker band for the degree of conformational twisting, as outlined previously. Using the spectral information presented in this work it should be possible to generate an accurate molecular movie of the formation of the excited-state plateau structure with the help of computational modelling.

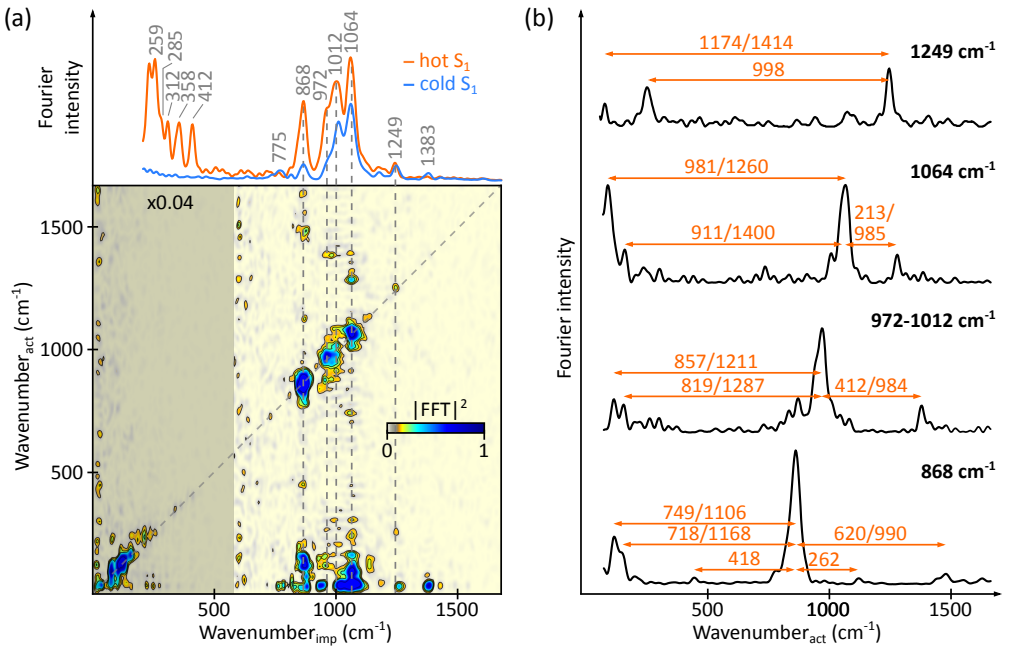

Figure 8.5: 2D PC-IVS on all-*trans* RPSB in methanol. (a) Fourier transformation of the oscillatory modulations along the actinic-impulsive pump time delay (Figure 8.4b) generates a two-dimensional excited-state IVS Raman map characterised by diagonal peaks and cross peaks connected vertically to the excited-state Raman spectrum (orange - hot, blue - cold). (b) Vertical cuts along the major high-frequency modes (bold, grey dashed vertical lines in (a)). Numbers denote frequency differences between the diagonal peak and the observed cross peaks. The first number indicates direct subtraction, while the second number accounts for Fourier wrapping effects due to an insufficient sampling frequency. Frequency differences >1650 cm^{-1} have been ignored due to the absence of spectral features in the excited-state Raman spectrum.

8.2.4 2D Excited-State Raman

Closer inspection of the mode-specific dynamics shown in Figure 8.4b shows strong oscillatory modulations which arise as a consequence of VC generated directly on the excited electronic state via the impulsive action of the actinic pump pulse. To extract the structural origins, we subtract the slowly varying spectral dynamics and Fourier transform the resulting oscillations to obtain a 2D Raman map (Figure 8.5a). As in wt-GFP (chapter 7), this map shows pronounced coherence activity around the diagonal of the map and vertical cross peaks, mainly located near 1000 cm^{-1}. Vertical cross peaks coincide with excited-state Raman frequencies and provide information about initial FC factors, mode-to-mode dipole moments and initial structural evolutions (chapter 7).

In analogy to the analysis carried out for wt-GFP, we compute difference frequencies to corresponding diagonal peaks for the most prominent excited-state modes (dashed, Figure 8.5a) to obtain information about potential coupling patterns (Figure 8.5b). The experiment was carried out with an actinic time step of 10 fs, leading to a Nyquist frequency of $\sim$1650 cm^{-1}. We hence calculated the difference frequencies with respect to the main diagonal peaks, taking Fourier wrapping due to undersampling into account (second number). We find a large variety of cross peaks predominantly centred around the HOOP and methyl rocking region (1000$\pm$200 cm^{-1}) as well as HOOP couplings to low-frequency modes (<500 cm^{-1}) present in the FC Raman spectrum. In particular the wealth of cross peaks observed for the 868 cm^{-1} HOOP mode (C_{10}-H and C_{12}-H) suggests a very active role in the relaxation process out of the FC region. A detailed analysis based on an improved theoretical model is required to conclusively reveal the exact direction of the vibrational energy flow after photoexcitation.

8.3 Conclusion

We provided time-domain Raman spectra of the excited electronic state of all-*trans* RPSB in methanol solution employing PDP IVS and PC-IVS. Our results demonstrate that low-frequency modes are activated directly out of the FC region, indicating pronounced structural changes along the backbone. High-frequency modes are predominantly active in the HOOP and methyl rocking region, and reveal an excited-state plateau which is characterised by a twisted all-*trans* configuration predominantly along the C_{11}=C_{12} bond. This observation is in agreement with recent findings employing degenerate four-wave mixing.[114,209] In addition, we demonstrated the excited-state structural changes occurring on the <200 fs time scale with high time-resolution PC-IVS. To the best of our knowledge, this is the first complete structural characterisation of the excited-state dynamics after photon absorption at 400 nm. Our results show that the main coordinate for the relaxation out of the FC region are the C_{10}-H and C_{12}-H out-of-plane motions, which must be anharmonically coupled to initially activated C=C stretch and low-frequency modes. Lastly, we presented the first 2D Raman map of the excited electronic state of all-*trans* RPSB indicating coupling between HOOP and low-frequency modes. Further theoretical modelling and a more refined theory of 2D excited-state

Raman spectroscopy, as employed here, will most likely provide information to completely understand the excited-state dynamics and potential energy surface properties in this and related systems.

Mechanistic Implications for bR

The insights obtained for all-*trans* RPSB strongly support the anharmonic coupling picture put forward for bR.[98] Importantly, the initial structural rearrangements in all-*trans* RPSB are complete within 300 fs based on the observed mode-specific dynamics, a time scale shorter than the excited-state lifetime of bR (500 fs). We therefore propose that the initial structural relaxation of the chromophore in bR follows the same key principles outlined for the chromophore in solution, namely initial photoexcitation of planar backbone stretching modes followed by anharmonic coupling to HOOP and methyl rocking motions around the C_{13}=C_{14} bond, supported by low-frequency modes to internally dissipate the excess energy. The role of the protein environment in this model is thus decoupled from any mechanistic influences. Instead, the protein is responsible mainly for the opsin shift (560 nm absorption maximum) to guarantee optimal solar-spectrum coverage and a reduction of the excited-state barrier along the isomerisation coordinate due to steric effects.[206] These results are in line with recent findings on visual rhodopsin.[213] A similar mechanism seems also likely for the primary isomerisation in channelrhodopsins.

Methods

All experiments were carried out at a repetition rate of 10 kHz employing a gravity-driven flow scheme based on an overflow reservoir and a membrane pump (KNF SIMDOS) which ensured complete replenishment of the sample between consecutive laser shots. The sample was prepared as described by Bassolino *et al*[149] and protonated directly before the experiment to avoid thermal degradation to yield an $OD_{445\,\mathrm{nm}}^{200\,\mu\mathrm{m}} = 2$ in a 200 μm flowcell. The PDP IVS experiment (Figure 8.2) employed 50 nJ of a 520 nm pump pulse (12 fs) and 80 nJ of an 800 nm dump pulse (200 fs) focused to 80 and 100 μm at the sample, with a probe focus of 50 μm. The pulse parameters for PC-IVS at 590 nm (Figure 8.1b and 8.3) were: actinic - 400 nm, 25 fs, 100 nJ, 65 μm focus, impulsive - 590 nm, 11 fs, 20 nJ, 50 μm focus, dump - 1030 nm, 200 fs, 150 nJ, 90 μm focus, probe - 30 μm focus. The pulse parameters for PC-IVS at 800

nm (Figure 8.3) were: actinic - 400 nm, 250 fs, 300 nJ, 80 μm focus, impulsive - 800 nm, 8 fs, 95 nJ, 68 μm focus, dump - 1030 nm, 200 fs, 230 nJ, 80 μm focus, probe - 56 μm focus. High time-resolution PC-IVS was carried out with the following parameters: actinic - 400 nm, 13 fs, 200 nJ, 80 μm focus, impulsive - 590 nm, 13 fs, 50 nJ, 70 μm focus, dump - 1030 nm, 200 fs, 200 nJ, 105 μm focus, probe - 31 μm focus.

We remark that in all experiments using a 590 nm impulsive pump pulse we assured a maximum of 0.5% direct excitation (DTT). A stepsize of 2.8 fs was used for experiments with impulsive pules centred at 590 nm while 3.5 fs was employed for 800 nm impulsive pump pulses.

Chapter 9

Summary and Outlook

9.1 Summary

The main aspect of this work was to develop and utilise a highly sensitive impulsive vibrational spectroscopy (IVS) setup capable of resolving vibrational signatures from excited electronic states. The developed system is unique in that it is based on a Yb:KGW laser source emitting at 1030 nm instead of the commonly employed Ti:Sapphire systems operating at 800 nm. Consequently, new optical designs were developed to accommodate the change in source wavelength, leading to the implementation of previously undocumented broadband non-collinear optical parametric amplifiers (NOPAs) with pulse durations below 10 fs. The designs were optimised to accommodate good long-term stability and mode quality for the use in highly sensitive IVS spectroscopy. The addition of a narrowband (200-300 fs) NOPA and a second-harmonic broadband NOPA at 400 nm (∼13 fs) extended the range of measurable systems greatly and allowed us to push the technique beyond a proof-of-principle stage.

Beyond optical designs, this work provided a variety of pulse sequences to isolate vibrational information from excited electronic states. The main objective behind these pulse schemes was to clearly distinguish between vibrational coherences of the target excited electronic state and other signals which complicate the interpretation of the retrieved Raman spectra. By introducing a subtraction routine or an additional population-control pulse, we were able to unambiguously extract baseline- and background free excited-state Raman spectra and to track structural evolution with high temporal precision. At the same time, we were able to obtain information about the energy flow mediated by vibrational modes from a two-dimensional Raman scheme which appears to be capable of resolving excited-state vibrational couplings and anharmonicities.

Overall, we have successfully applied our technique to a wide range of systems and demonstrated the capabilities and limitations of IVS. The systems explored with the setup were mainly chosen because of their unique photochemical properties. Rhodopsin, responsible for initiating the process of vision, was used as a model system to investigate how vibrational wavepackets behave upon crossing electronic states via a conical intersection (CI). We could show that wavepacket motion in tuning modes is unaffected by the CI, while wavepacket motion in coupling modes is significantly reduced. The results illustrated how vibrational coherences can be used to derive potential energy surface characteristics.

In addition, we investigated the effect of altering the hydrogen substitution pattern on retinal by isotopic labelling. By using our setup and external quantum yield measurements, it was possible to verify the long-held assumption about the importance of the hydrogen out-of-plane modes, in agreement with our previous study. The results further required a more complex phase-space description of ultrafast internal conversion processes, which occur on a shorter time scale than vibrational relaxation. Here, the exact interplay between modes in relation to the underpinning potential energy surface dictates the outcome of the reaction, rather than a simple branching ratio based on rate constants.

In collaboration with the groups of Ramona Schlesinger and Joachim Heberle (FU Berlin), we investigated the photodynamics of channelrhodopsin-1. We revealed a vibrationally coherent photoproduct formation, much like in rhodopsin, but occurring on a significantly longer time scale. By complementing IVS with low-temperature resonance Raman spectroscopy, we were able to characterise the structure of the rapidly (<1 ps) formed intermediate, P_1, to be in a twisted 13-*cis* conformation. This study exemplified the use of IVS towards a previously unknown system and demonstrated how IVS can be used to derive system characteristics with minimal prior knowledge.

We explored the possibility of recording a molecular movie by investigating the proton transfer reaction in the well-studied wt-GFP. We temporally resolved the formation of the fluorescent intermediate with structural accuracy. The analysis of FC Raman spectra, excited-state Raman spectra and 2D Raman spectra further allowed us to propose a complete mechanism including all vibrational couplings required for the proton transfer reaction.

Finally, all-*trans* retinal protonated Schiff base in methanol solution was subject to a complete excited-state characterisation using IVS. By combining a

variety of techniques we monitored the complete structural relaxation process from the initially excited Franck-Condon structure to the excited-state plateau. We identified vibrational couplings based on 2D Raman between hydrogen out-of-plane modes and low-frequency modes, confirming that IVS is a powerful tool which, in collaboration with theoretical modelling, is capable of providing excited-state molecular movies for a wide range of systems, including complex biological systems.

9.2 Outlook

The work outlined here is just a first step towards developing IVS into a universal tool capable of answering a wide range of questions (breakdown of the Born-Oppenheimer approximation, conical intersection structures, directional energy flow in complex systems, etc.). In particular, a thorough theoretical framework is required at this stage to confidently assign the observed signals correctly. In this regard it will be necessary to develop IVS to investigate smaller molecules, whose potential energy surfaces are more readily calculated. Despite the associated technical difficulties, we believe that this will also act as a solid benchmarking procedure for IVS to avoid ambiguous signal interpretations. The latter is of immense value for the interpretation of 2D excited-state Raman maps, as presented in this work. By studying smaller systems with known properties, it should be possible to devise a general routine to extract quantitative information, as often performed in other 2D techniques.

2D Raman spectroscopy, in general, is a very promising tool to reveal more information about vibrational couplings on excited electronic states. In this regard, it may be beneficial to extend our current 2D Raman technique into a four-pulse scheme with a long actinic pump pulse to only populate the excited electronic state, followed by an impulsive pump pulse to generate vibrational coherence directly on this state, which is subsequently probed by an IVS Raman sequence. This technique should be capable of revealing potential energy surfaces on vibrationally cold excited electronic states, which is currently inaccessible with our scheme. An alternative route is to develop an excited-state extension of a recently demonstrated 2D ground-state Raman technique based on sophisticated pulse shaping to obtain excited electronic state 2D Raman spectra.[197]

In addition, it would be very interesting to combine an impulsive pump with a broadband IR probe rather than an electronic probe, provided sufficient bandwidth can be provided. Ultrafast (<20 fs) transient IR spectroscopy could become a very sensitive technique to complement Raman spectroscopy.[214,215] This approach would also allow detection of mode-couplings between Raman- and IR-active modes in excited electronic states, which might be a valuable route to study system-bath interactions on the femtosecond time scale. The technique could also be readily extended to a multi-dimensional analogue capable of providing otherwise inaccessible coupling information.

Besides an improvement of the technique to isolate excited-state features and their interpretation, we believe that IVS also has great potential for spectrochemical imaging. Here it is important to rapidly acquire the vibrational signatures found in cells to avoid radiation damage, which cannot be achieved by spontaneous or even stimulated Raman scattering. Current techniques primarily focus on the C-H stretching region $\sim$3000 cm^{-1}, but chemical selectivity is drastically increased in the fingerprint region <1600 cm^{-1}.[216] Broadband CARS methods in the frequency-domain[217] have recently advanced to cover these regions in tissues, but are plagued by lineshape distortions and non-resonant background. Time-domain techniques, on the other hand, can produce baseline-free Raman spectra which avoids the complications in current state-of-the-art Raman microscopy.[84]

References

[1] A. J. Bard and M. A. Fox, *Acc. Chem. Res.*, 1995, **28**, 141–5.

[2] T. Brixner, J. Stenger, H. M. Vaswani, M. Cho, R. E. Blankenship and G. R. Fleming, *Nature*, 2005, **434**, 625–8.

[3] G. S. Engel, T. R. Calhoun, E. L. Read, T.-K. Ahn, T. Mančal, Y.-C. Cheng, R. E. Blankenship and G. R. Fleming, *Nature*, 2007, **446**, 782–6.

[4] H. Lee, Y.-C. Cheng and G. R. Fleming, *Science*, 2007, **316**, 1462–5.

[5] E. Romero, R. Augulis, V. I. Novoderezhkin, M. Ferretti, J. Thieme, D. Zigmantas and R. van Grondelle, *Nat. Phys.*, 2014, **10**, 676–82.

[6] M. Suga, F. Akita, K. Hirata, G. Ueno, H. Murakami, Y. Nakajima, T. Shimizu, K. Yamashita, M. Yamamoto, H. Ago and J.-R. Shen, *Nature*, 2014, **517**, 99–103.

[7] R. W. Schoenlein, L. A. Peteanu, R. A. Mathies and C. V. Shank, *Science*, 1991, **254**, 412–5.

[8] Q. Wang, R. W. Schoenlein, L. A. Peteanu, R. A. Mathies and C. V. Shank, *Science*, 1994, **266**, 422–4.

[9] K. Palczewski, T. Kumasaka, T. Hori, C. A. Behnke, H. Motoshima, B. A. Fox, I. Le Trong, D. C. Teller, T. Okada, R. E. Stenkamp, M. Yamamoto and M. Miyano, *Science*, 2000, **289**, 739–45.

[10] D. Polli, P. Altoè, O. Weingart, K. M. Spillane, C. Manzoni, D. Brida, G. Tomasello, G. Orlandi, P. Kukura, R. A. Mathies, M. Garavelli and G. Cerullo, *Nature*, 2010, **467**, 440–3.

[11] R. N. Van Gelder and K. Kaur, *Curr. Biol.*, 2015, **25**, R713–5.

[12] A. Warshel, *Nature*, 1976, **260**, 679–83.

[13] M. Prigge, F. Schneider, S. P. Tsunoda, C. Shilyansky, J. Wietek, K. Deisseroth and P. Hegemann, *J. Biol. Chem.*, 2012, **287**, 31804–12.

[14] S. Y. Hou, E. G. Govorunova, M. Ntefidou, C. E. Lane, E. N. Spudich, O. A. Sineshchekov and J. L. Spudich, *Photochem. Photobiol.*, 2012, **88**, 119–28.

[15] M. I. Stockman, M. F. Kling, U. Kleineberg and F. Krausz, *Nat. Photonics*, 2007, **1**, 539–44.

[16] K. F. MacDonald, Z. L. Samson, M. I. Stockman and N. I. Zheludev, *Nat. Photonics*, 2008, **3**, 55–8.

[17] G. A. Wurtz, R. Pollard, W. Hendren, G. P. Wiederrecht, D. J. Gosztola, V. A. Podolskiy and A. V. Zayats, *Nat. Nanotechnol.*, 2011, **6**, 107–11.

[18] L. Lagnado and D. Baylor, *Neuron*, 1992, **8**, 995–1002.

[19] A. Mokhtari, P. Cong, J. L. Herek and A. H. Zewail, *Nature*, 1990, **348**, 225–7.

[20] M. Cho, *Nature*, 2006, **444**, 431–2.

[21] A. H. Zewail, *Science*, 2010, **328**, 187–93.

[22] J. A. Weinstein and N. T. Hunt, *Nat. Chem.*, 2012, **4**, 157–8.

[23] M. Gao, C. Lu, H. Jean-Ruel, L. C. Liu, A. Marx, K. Onda, S. Koshihara, Y. Nakano, X. Shao, T. Hiramatsu, G. Saito, H. Yamochi, R. R. Cooney, G. Moriena, G. Sciaini and R. J. D. Miller, *Nature*, 2013, **496**, 343–6.

[24] P. Kukura, H. Ewers, C. Müller, A. Renn, A. Helenius and V. Sandoghdar, *Nat. Methods*, 2009, **6**, 923–7.

[25] J. Ortega-Arroyo and P. Kukura, *Phys. Chem. Chem. Phys.*, 2012, **14**, 15625–36.

[26] B.-C. Chen, W. R. Legant, K. Wang, L. Shao, D. E. Milkie, M. W. Davidson, C. Janetopoulos, X. S. Wu, J. A. Hammer, Z. Liu, B. P. English, Y. Mimori-Kiyosue, D. P. Romero, A. T. Ritter, J. Lippincott-Schwartz, L. Fritz-Laylin, R. D. Mullins, D. M. Mitchell, J. N. Bembenek, A.-C. Reymann, R. Bohme, S. W. Grill, J. T. Wang, G. Seydoux, U. S. Tulu, D. P. Kiehart and E. Betzig, *Science*, 2014, **346**, 1257998.

[27] R. Berera, R. van Grondelle and J. T. M. Kennis, *Photosynth. Res.*, 2009, **101**, 105–18.

[28] A. J. Musser, M. Liebel, C. Schnedermann, T. Wende, T. B. Kehoe, A. Rao and P. Kukura, *Nat. Phys.*, 2015, **11**, 352–7.

[29] M. Cho, H. M. Vaswani, T. Brixner, J. Stenger and G. R. Fleming, *J. Phys. Chem. B*, 2005, **109**, 10542–56.

[30] P. F. Tekavec, J. A. Myers, K. L. M. Lewis and J. P. Ogilvie, *Opt. Lett.*, 2009, **34**, 1390–2.

[31] E. Harel, A. F. Fidler and G. S. Engel, *J. Phys. Chem. A*, 2011, **115**, 3787–96.

[32] A. L. Stelling, K. L. Ronayne, J. Nappa, P. J. Tonge and S. R. Meech, *J. Am. Chem. Soc.*, 2007, **129**, 15556–64.

[33] G. M. Roberts, H. J. B. Marroux, M. P. Grubb, M. N. R. Ashfold and A. J. Orr-Ewing, *J. Phys. Chem. A*, 2014, **118**, 11211–25.

[34] D. Murdock, S. J. Harris, J. Luke, M. P. Grubb, A. J. Orr-Ewing and M. N. R. Ashfold, *Phys. Chem. Chem. Phys.*, 2014, **16**, 21271–9.

[35] P. Hamm and M. T. Zanni, *Concepts and Methods of 2D Infrared Spectroscopy*, Cambridge University Press, 2011.

[36] F. Ding and M. T. Zanni, *Chem. Phys.*, 2007, **341**, 95–105.

[37] P. Mukherjee, I. Kass, I. T. Arkin and M. T. Zanni, *Proc. Natl. Acad. Sci.*, 2006, **103**, 3528–33.

[38] S. Woutersen, Y. Mu, G. Stock and P. Hamm, *Chem. Phys.*, 2001, **266**, 137–47.

[39] M. Khalil, N. Demirdöven and A. Tokmakoff, *J. Phys. Chem. A*, 2003, **107**, 5258–79.

[40] S. E. J. Bell, *Analyst*, 1996, **121**, 107R–20R.

[41] P. G. Bradley, N. Kress, B. A. Hornberger, R. F. Dallinger and W. H. Woodruff, *J. Am. Chem. Soc.*, 1981, **103**, 7441–6.

[42] H. Hamaguchi and T. L. Gustafson, *Annu. Rev. Phys. Chem.*, 1994, **45**, 593–622.

[43] M. Schmitt, G. Knopp, A. Materny and W. Kiefer, *Chem. Phys. Lett.*, 1997, **270**, 9–15.

[44] P. Kukura, D. W. McCamant and R. A. Mathies, *Annu. Rev. Phys. Chem.*, 2007, **58**, 461–88.

[45] B. Mallick, A. Lakhsmanna and S. Umapathy, *J. Raman Spectrosc.*, 2011, **42**, 1883–90.

[46] L. Zhu, W. Liu and C. Fang, *Appl. Phys. Lett.*, 2014, **105**, 041106.

[47] S. Ruhman, B. Kohler, A. G. Joly and K. A. Nelson, *IEEE J. Quantum Electron.*, 1988, **24**, 470–81.

[48] S. Ruhman, A. G. Joly and K. A. Nelson, *IEEE J. Quantum Electron.*, 1988, **24**, 460–9.

[49] S. Fujiyoshi, S. Takeuchi and T. Tahara, *J. Phys. Chem. A*, 2003, **107**, 494–500.

[50] M. Son, K. H. Park, M.-C. Yoon, P. Kim and D. Kim, *J. Phys. Chem. A*, 2015, **119**, 6275–82.

[51] A. M. Weiner, *Ultrafast Optics*, John Wiley & Sons, Inc., 2009.

[52] R. W. Boyd, *Nonlinear Optics*, Academic Press, 2008.

[53] C. Rullière, *Femtosecond laser pulses : principles and experiments*, Springer, 2005.

[54] S. Mukamel, *Principles of Nonlinear Optical Spectroscopy*, Oxford University Press, 1999.

[55] P. Hamm, *Principles of Nonlinear Optical Spectroscopy: A Practical Approach or: Mukamel for Dummies*, 2005.

[56] M. Bass, P. A. Franken, J. F. Ward and G. Weinreich, *Phys. Rev. Lett.*, 1962, **9**, 446–8.

[57] P. A. Franken, A. E. Hill, C. W. Peters and G. Weinreich, *Phys. Rev. Lett.*, 1961, **7**, 118–9.

[58] A. Savage and R. C. Miller, *Appl. Opt.*, 1962, **1**, 661–4.

[59] M. Bass, P. A. Franken, A. E. Hill, C. W. Peters and G. Weinreich, *Phys. Rev. Lett.*, 1962, **8**, 18.

[60] G. Cerullo and S. De Silvestri, *Rev. Sci. Instrum.*, 2003, **74**, 1.

[61] A. L. Gaeta, *Phys. Rev. Lett.*, 2000, **84**, 3582–5.

[62] A. Couairon and A. Mysyrowicz, *Phys. Rep.*, 2007, **441**, 47–189.

[63] L. Berge, S. Skupin, R. Nuter, J. Kasparian and J. P. Wolf, *Rep. Prog. Phys.*, 2007, **70**, 1633–713.

[64] M. Liebel, C. Schnedermann and P. Kukura, *Opt. Lett.*, 2014, **39**, 4112–5.

[65] T. Wende, M. Liebel, C. Schnedermann, R. J. Pethick and P. Kukura, *J. Phys. Chem. A*, 2014, **118**, 9976–84.

[66] M. Liebel, C. Schnedermann, T. Wende and P. Kukura, *J. Phys. Chem. A*, 2015, **119**, 9506–17.

[67] M. Bradler and E. Riedle, *J. Opt. Soc. Am. B*, 2014, **31**, 1465–75.

[68] A. Calendron, H. Çankaya, G. Cirmi and F. X. Kärtner, *Opt. Express*, 2015, **23**, 13866–79.

[69] M. Bradler, P. Baum and E. Riedle, *Appl. Phys. B Lasers Opt.*, 2009, **97**, 561–74.

[70] R. Alfano and S. Shapiro, *Phys. Rev. Lett.*, 1970, **24**, 592–4.

[71] M. Bellini and T. W. Hänsch, *Opt. Lett.*, 2000, **25**, 1049–51.

[72] T. Wilhelm, J. Piel and E. Riedle, *Opt. Lett.*, 1997, **22**, 1494–6.

[73] J. Piel, M. Beutter and E. Riedle, *Opt. Lett.*, 2000, **25**, 180–2.

[74] T. Kobayashi and A. Baltuska, *Meas. Sci. Technol.*, 2002, **13**, 1671–82.

[75] P. Baum, S. Lochbrunner and E. Riedle, *Opt. Lett.*, 2004, **29**, 1686–8.

[76] M. Bradler and E. Riedle, *Opt. Lett.*, 2014, **39**, 2588–91.

[77] R. Trebino, K. W. DeLong, D. N. Fittinghoff, J. N. Sweetser, M. A. Krumbugel, B. A. Richman and D. J. Kane, *Rev. Sci. Instrum.*, 1997, **68**, 3277–95.

[78] P. Bowlan, P. Gabolde, A. Shreenath, K. McGresham, R. Trebino and S. Akturk, *Opt. Express*, 2006, **14**, 11892–900.

[79] G. Stibenz and G. Steinmeyer, *Opt. Express*, 2005, **13**, 2617–26.

[80] A. J. Musser, M. Al-Hashimi, M. Maiuri, D. Brida, M. Heeney, G. Cerullo, R. H. Friend and J. Clark, *J. Am. Chem. Soc.*, 2013, **135**, 12747–54.

[81] K. E. H. Anderson, S. L. Sewall, R. R. Cooney and P. Kambhampati, *Rev. Sci. Instrum.*, 2007, **78**, 073101.

[82] S. A. Kovalenko, A. L. Dobryakov, J. Ruthmann and N. P. Ernsting, *Phys. Rev. A*, 1999, **59**, 2369–84.

[83] W. T. Pollard, *Annu. Rev. Phys. Chem.*, 1992, **43**, 497–523.

[84] T. Ideguchi, S. Holzner, B. Bernhardt, G. Guelachvili, N. Picqué and T. W. Hänsch, *Nature*, 2013, **502**, 355–8.

[85] M. Liebel and P. Kukura, *J. Phys. Chem. Lett.*, 2013, **4**, 1358–64.

[86] M. Czerny and A. F. Turner, *Zeitschrift für Phys.*, 1930, **61**, 792–7.

[87] U. Megerle, I. Pugliesi, C. Schriever, C. F. Sailer and E. Riedle, *Appl. Phys. B*, 2009, **96**, 215–31.

[88] M. Liebel, *Ph.D. thesis*, University of Oxford, 2014.

[89] M. V. Lebedev, O. V. Misochko, T. Dekorsy and N. Georgiev, *J. Exp. Theor. Phys.*, 2005, **100**, 272–82.

[90] J. Kaiser and R. Schafer, *IEEE Trans. Acoust.*, 1980, **28**, 105–7.

[91] R. W. Wood and D. H. Rank, *Phys. Rev.*, 1935, **48**, 63–5.

[92] H. Nyquist, *Trans. Am. Inst. Electr. Eng.*, 1928, **47**, 617–44.

[93] D. Polli, L. Lüer and G. Cerullo, *Rev. Sci. Instrum.*, 2007, **78**, 103108.

[94] A. L. Dobryakov and N. P. Ernsting, *J. Chem. Phys.*, 2008, **129**, 184504.

[95] C. Schnedermann, M. Liebel and P. Kukura, *J. Am. Chem. Soc.*, 2015, **137**, 2886–91.

[96] D. Polli, D. Brida, S. Mukamel, G. Lanzani and G. Cerullo, *Phys. Rev. A*, 2010, **82**, 053809.

[97] A. E. Johnson and A. B. Myers, *J. Chem. Phys.*, 1996, **104**, 2497–507.

[98] M. Liebel, C. Schnedermann, G. Bassolino, G. Taylor, A. Watts and P. Kukura, *Phys. Rev. Lett.*, 2014, **112**, 238301.

[99] M. Liebel, C. Schnedermann and P. Kukura, *Phys. Rev. Lett.*, 2014, **112**, 198302.

[100] E. J. Heller, *Acc. Chem. Res.*, 1981, **14**, 368–75.

[101] P. Kukura, D. W. McCamant, P. H. Davis and R. A. Mathies, *Chem. Phys. Lett.*, 2003, **382**, 81–6.

[102] W. A. Yee, R. H. O'Neil, J. W. Lewis, J. Z. Zhang and D. S. Kliger, *J. Phys. Chem. A*, 1999, **103**, 2388–93.

[103] I. H. M. van Stokkum, D. S. Larsen and R. van Grondelle, *Biochim. Biophys. Acta - Bioenerg.*, 2004, **1657**, 82–104.

[104] J. M. Beechem, M. l. Ameloot and L. Brand, *Instrum. Sci. Technol.*, 1985, **14**, 379–402.

[105] A. Kühl and W. Domcke, *J. Chem. Phys.*, 2002, **116**, 263–74.

[106] D. Egorova and W. Domcke, *J. Photochem. Photobiol. A Chem.*, 2004, **166**, 19–31.

[107] A. L. Dobryakov, I. Ioffe, A. A. Granovsky, N. P. Ernsting and S. A. Kovalenko, *J. Chem. Phys.*, 2012, **137**, 244505.

[108] A. Weigel and N. P. Ernsting, *J. Phys. Chem. B*, 2010, **114**, 7879–93.

[109] O. Bismuth, N. Friedman, M. Sheves and S. Ruhman, *Chem. Phys.*, 2007, **341**, 267–75.

[110] D. P. Hoffman, S. R. Ellis and R. A. Mathies, *J. Phys. Chem. A*, 2014, **118**, 4955–65.

[111] D. T. Valley, D. P. Hoffman and R. A. Mathies, *Phys. Chem. Chem. Phys.*, 2015, **17**, 9231–40.

[112] S. Takeuchi, S. Ruhman, T. Tsuneda, M. Chiba, T. Taketsugu and T. Tahara, *Science*, 2008, **322**, 1073–7.

[113] A. Wand, I. Gdor, J. Zhu, M. Sheves and S. Ruhman, *Annu. Rev. Phys. Chem.*, 2013, **64**, 437–58.

[114] J. P. Kraack, T. Buckup and M. Motzkus, *J. Phys. Chem. Lett.*, 2013, **4**, 383–7.

[115] W. Domcke and D. R. Yarkony, *Annu. Rev. Phys. Chem.*, 2012, **63**, 325–52.

[116] S. Hahn and G. Stock, *J. Phys. Chem. B*, 2000, **104**, 1146–9.

[117] B. Lasorne, G. A. Worth and M. A. Robb, *Wiley Interdiscip. Rev. Comput. Mol. Sci.*, 2011, **1**, 460–75.

[118] I. V. Rostov, R. D. Amos, R. Kobayashi, G. Scalmani and M. J. Frisch, *J. Phys. Chem. B*, 2010, **114**, 5547–55.

[119] A. M. Virshup, C. Punwong, T. V. Pogorelov, B. A. Lindquist, C. Ko and T. J. Martínez, *J. Phys. Chem. B*, 2009, **113**, 3280–91.

[120] J. Léonard, I. Schapiro, J. Briand, S. Fusi, R. R. Paccani, M. Olivucci and S. Haacke, *Chem. Eur. J.*, 2012, **18**, 15296–304.

[121] G. Wald, *Science*, 1968, **162**, 230–9.

[122] I. Schapiro, M. N. Ryazantsev, L. M. Frutos, N. Ferré, R. Lindh and M. Olivucci, *J. Am. Chem. Soc.*, 2011, **133**, 3354–64.

[123] O. Weingart and M. Garavelli, *J. Chem. Phys.*, 2012, **137**, 22A523.

[124] J. Briand, O. Bräm, J. Réhault, J. Léonard, A. Cannizzo, M. Chergui, V. Zanirato, M. Olivucci, J. Helbing and S. Haacke, *Phys. Chem. Chem. Phys.*, 2010, **12**, 3178–87.

[125] L. M. Frutos, T. Andruniów, F. Santoro, N. Ferré and M. Olivucci, *Proc. Natl. Acad. Sci. USA*, 2007, **104**, 7764–9.

[126] I. Schapiro, O. Weingart and V. Buss, *J. Am. Chem. Soc.*, 2009, **131**, 16–7.

[127] A. Strambi, P. B. Coto, L. M. Frutos, N. Ferré and M. Olivucci, *J. Am. Chem. Soc.*, 2008, **130**, 3382–8.

[128] O. Weingart, *Chem. Phys.*, 2008, **349**, 348–55.

[129] R. A. Mathies, C. Brito Cruz, W. T. Pollard and C. V. Shank, *Science*, 1988, **240**, 777–9.

[130] S. W. Lin, M. Groesbeek, I. van der Hoef, P. Verdegem, J. Lugtenburg and R. A. Mathies, *J. Phys. Chem. B*, 1998, **102**, 2787–806.

[131] P. Kukura, D. W. McCamant, S. Yoon, D. B. Wandschneider and R. A. Mathies, *Science*, 2005, **310**, 1006–9.

[132] I. Palings, J. A. Pardoen, E. van den Berg, C. Winkel, J. Lugtenburg and R. A. Mathies, *Biochemistry*, 1987, **26**, 2544–56.

[133] W. T. Pollard, S. L. Dexheimer, Q. Wang, L. A. Peteanu, C. V. Shank and R. A. Mathies, *J. Phys. Chem.*, 1992, **96**, 6147–58.

[134] S. L. Dexheimer, Q. Wang, L. A. Peteanu, W. T. Pollard, R. A. Mathies and C. V. Shank, *Chem. Phys. Lett.*, 1992, **188**, 61–6.

[135] O. Weingart, P. Altoè, M. Stenta, A. Bottoni, G. Orlandi and M. Garavelli, *Phys. Chem. Chem. Phys.*, 2011, **13**, 3645–8.

[136] S. Gozem, F. Melaccio, R. Lindh, A. I. Krylov, A. A. Granovsky, C. Angeli and M. Olivucci, *J. Chem. Theory Comput.*, 2013, **9**, 4495–506.

[137] G. R. Loppnow and R. A. Mathies, *Biophys. J*, 1988, **54**, 35–43.

[138] D. W. McCamant, *J. Phys. Chem. B*, 2011, **115**, 9299–305.

[139] W. J. de Grip, F. J. Daemen and S. L. Bonting, *Methods Enzymol.*, 1980, **67**, 301–20.

[140] J. E. Kim, M. J. Tauber and R. A. Mathies, *Biochemistry*, 2001, **40**, 13774–8.

[141] R. S. Becker and K. Freedman, *J. Am. Chem. Soc.*, 1985, **107**, 1477–85.

[142] R. R. Birge and L. M. Hubbard, *J. Am. Chem. Soc.*, 1980, **102**, 2195–205.

[143] R. S. H. Liu and L. U. Colmenares, *Proc. Natl. Acad. Sci.*, 2003, **100**, 14639–44.

[144] O. Weingart, *J. Am. Chem. Soc.*, 2007, **129**, 10618–9.

[145] G. G. Kochendoerfer, P. J. Verdegem, I. van der Hoef, J. Lugtenburg and R. A. Mathies, *Biochemistry*, 1996, **35**, 16230–40.

[146] G. Eyring, B. Curry, A. Broek, J. Lugtenburg and R. A. Mathies, *Biochemistry*, 1982, **21**, 384–93.

[147] H. Kandori, Y. Shichida and T. Yoshizawa, *Biochemistry*, 2001, **66**, 1197–209.

[148] T. Sovdat, G. Bassolino, M. Liebel, C. Schnedermann, S. P. Fletcher and P. Kukura, *J. Am. Chem. Soc.*, 2012, **134**, 8318–20.

[149] G. Bassolino, T. Sovdat, M. Liebel, C. Schnedermann, B. Odell, T. D. W. Claridge, P. Kukura and S. P. Fletcher, *J. Am. Chem. Soc.*, 2014, **136**, 2650–8.

[150] D. C. Todd and G. R. Fleming, *J. Chem. Phys.*, 1993, **98**, 269–79.

[151] A. Jablonski, *Nature*, 1933, **131**, 839–40.

[152] R. S. Liu and A. E. Asato, *Proc. Natl. Acad. Sci. U. S. A.*, 1985, **82**, 259–63.

[153] P. Hegemann, *Annu. Rev. Plant Biol.*, 2008, **59**, 167–89.

[154] P. Hegemann and G. Nagel, *EMBO Mol. Med.*, 2013, **5**, 173–6.

[155] V. A. Lórenz-Fonfría and J. Heberle, *Biochim. Biophys. Acta - Bioenerg.*, 2014, **1837**, 626–42.

[156] L. Fenno, O. Yizhar and K. Deisseroth, *Annu. Rev. Neurosci.*, 2011, **34**, 389–412.

[157] M. K. Verhoefen, C. Bamann, R. Blöcher, U. Förster, E. Bamberg and J. Wachtveitl, *ChemPhysChem*, 2010, **11**, 3113–22.

[158] V. A. Lórenz-Fonfría, B.-J. Schultz, T. Resler, R. Schlesinger, C. Bamann, E. Bamberg and J. Heberle, *J. Am. Chem. Soc.*, 2015, **137**, 1850–61.

[159] V. Muders, S. Kerruth, V. A. Lórenz-Fonfría, C. Bamann, J. Heberle and R. Schlesinger, *FEBS Lett.*, 2014, **588**, 2301–6.

[160] O. P. Ernst, D. T. Lodowski, M. Elstner, P. Hegemann, L. S. Brown and H. Kandori, *Chem. Rev.*, 2014, **114**, 126–63.

[161] J. I. Ogren, A. Yi, S. Mamaev, H. Li, J. L. Spudich and K. J. Rothschild, *J. Biol. Chem.*, 2015, **290**, 12719–30.

[162] J. I. Ogren, A. Yi, S. Mamaev, H. Li, J. Lugtenburg, W. J. de Grip, J. L. Spudich and K. J. Rothschild, *Biochemistry*, 2015, **54**, 377–88.

[163] O. A. Sineshchekov, E. G. Govorunova, J. Wang, H. Li and J. L. Spudich, *Biophys. J.*, 2013, **104**, 807–17.

[164] V. A. Lórenz-Fonfría, V. Muders, R. Schlesinger and J. Heberle, *J. Chem. Phys.*, 2014, **141**, 22D507.

[165] T. Stensitzki, V. Muders, R. Schlesinger, J. Heberle and K. Heyne, *Front. Mol. Biosci.*, 2015, **2**, 41.

[166] M. Braiman and R. A. Mathies, *Proc. Natl. Acad. Sci. U. S. A.*, 1982, **79**, 403–7.

[167] S. O. Smith, J. A. Pardoen, J. Lugtenburg and R. A. Mathies, *J. Phys. Chem.*, 1987, **91**, 804–19.

[168] A. Andreeva, I. Apostolova and M. Velitchkova, *Spectrochim. Acta Part A Mol. Biomol. Spectrosc.*, 2011, **78**, 1261–5.

[169] W. Fuß, *Chem. Phys.*, 2013, **425**, 96–103.

[170] L. Seidner and W. Domcke, *Chem. Phys.*, 1994, **186**, 27–40.

[171] I. Radu, C. Bamann, M. Nack, G. Nagel, E. Bamberg and J. Heberle, *J. Am. Chem. Soc.*, 2009, **131**, 7313–9.

[172] M. Nack, I. Radu, C. Bamann, E. Bamberg and J. Heberle, *FEBS Lett.*, 2009, **583**, 3676–80.

[173] S. R. Meech, *Chem. Soc. Rev.*, 2009, **38**, 2922–34.

[174] R. Y. Tsien, *Annu. Rev. Biochem.*, 1998, **67**, 509–44.

[175] K. D. Niswender, S. M. Blackman, L. Rohde, M. A. Magnuson and D. W. Piston, *J. Microsc.*, 1995, **180**, 109–16.

[176] M. Orm, A. B. Cubitt, K. Kallio, L. A. Gross, R. Y. Tsien and S. J. Remington, *Science*, 1996, **273**, 1392–5.

[177] S. P. Laptenok, A. Lukacs, A. Gil, R. Brust, I. V. Sazanovich, G. M. Greetham, P. J. Tonge and S. R. Meech, *Angew. Chemie Int. Ed.*, 2015, **54**, 9303–7.

[178] M. Chattoraj, B. A. King, G. U. Bublitz and S. G. Boxer, *Proc. Natl. Acad. Sci. U. S. A.*, 1996, **93**, 8362–7.

[179] K. Brejc, T. K. Sixma, P. A. Kitts, S. R. Kain, R. Y. Tsien, M. Ormö and S. J. Remington, *Proc. Natl. Acad. Sci. U. S. A.*, 1997, **94**, 2306–11.

[180] J. J. van Thor, K. L. Ronayne, M. Towrie and J. T. Sage, *Biophys. J.*, 2008, **95**, 1902–12.

[181] O. Vendrell, R. Gelabert, M. Moreno and J. M. Lluch, *J. Am. Chem. Soc.*, 2006, **128**, 3564–74.

[182] O. Vendrell, R. Gelabert, M. Moreno and J. M. Lluch, *J. Chem. Theory Comput.*, 2008, **4**, 1138–50.

[183] D. Stoner-Ma, A. A. Jaye, P. Matousek, M. Towrie, S. R. Meech and P. J. Tonge, *J. Am. Chem. Soc.*, 2005, **127**, 2864–5.

[184] D. Stoner-Ma, E. H. Melief, J. Nappa, K. L. Ronayne, P. J. Tonge and S. R. Meech, *J. Phys. Chem. B*, 2006, **110**, 22009–18.

[185] M. di Donato, L. J. G. W. van Wilderen, I. H. M. van Stokkum, T. C. Stuart, J. T. M. Kennis, K. J. Hellingwerf, R. van Grondelle and M. L. Groot, *Phys. Chem. Chem. Phys.*, 2011, **13**, 16295–305.

[186] C. Fang, R. R. Frontiera, R. Tran and R. A. Mathies, *Nature*, 2009, **462**, 200–4.

[187] H. Lossau, A. Kummer, R. Heinecke, F. Pöllinger-Dammer, C. Kompa, G. Bieser, T. Jonsson, C. M. Silva, M. M. Yang, D. C. Youvan and M. E. Michel-Beyerle, *Chem. Phys.*, 1996, **213**, 1–16.

[188] C.-C. Hsieh, P.-T. Chou, C.-W. Shih, W.-T. Chuang, M.-W. Chung, J. Lee and T. Joo, *J. Am. Chem. Soc.*, 2011, **133**, 2932–43.

[189] J. J. van Thor, G. Zanetti, K. L. Ronayne and M. Towrie, *J. Phys. Chem. B*, 2005, **109**, 16099–108.

[190] V. Tozzini and R. Nifosì, *J. Phys. Chem. B*, 2001, **105**, 5797–803.

[191] X. He, A. F. Bell and P. J. Tonge, *J. Phys. Chem. B*, 2002, **106**, 6056–66.

[192] J. Allen, *IEEE Trans. Acoust.*, 1977, **25**, 235–8.

[193] V. Tozzini, A. R. Bizzarri, V. Pellegrini, R. Nifosì, P. Giannozzi, A. Iuliano, S. Cannistraro and F. Beltram, *Chem. Phys.*, 2003, **287**, 33–42.

[194] R. D. Mehlenbacher, B. Lyons, K. C. Wilson, Y. Du and D. W. McCamant, *J. Chem. Phys.*, 2009, **131**, 244512.

[195] K. C. Wilson, B. Lyons, R. D. Mehlenbacher, R. Sabatini and D. W. McCamant, *J. Chem. Phys.*, 2009, **131**, 214502.

[196] A. Tokmakoff, M. Lang, D. Larsen, G. R. Fleming, V. Chernyak and S. Mukamel, *Phys. Rev. Lett.*, 1997, **79**, 2702–5.

[197] H. Frostig, T. Bayer, N. Dudovich, Y. C. Eldar and Y. Silberberg, *Nat. Photonics*, 2015, **9**, 339–43.

[198] J. P. Kraack, M. Motzkus and T. Buckup, *J. Chem. Phys.*, 2011, **135**, 224505.

[199] P. Schellenberg, E. Johnson, A. P. Esposito, P. J. Reid and W. W. Parson, *J. Phys. Chem. B*, 2001, **105**, 5316–22.

[200] R. Lozier, R. Bogomolni and W. Stoeckenius, *Biophys. J.*, 1975, **15**, 955–62.

[201] R. A. Mathies, S. W. Lin, J. B. Ames and W. T. Pollard, *Annu. Rev. Biophys. Biophys. Chem.*, 1991, **20**, 491–518.

[202] J. Tittor and D. Oesterhelt, *FEBS Lett.*, 1990, **263**, 269–73.

[203] K. A. Freedman and R. S. Becker, *J. Am. Chem. Soc.*, 1986, **108**, 1245–51.

[204] P. Hamm, M. Zurek, T. Röschinger, H. Patzelt, D. Oesterhelt and W. Zinth, *Chem. Phys. Lett.*, 1996, **263**, 613–21.

[205] H. Kandori and H. Sasabe, *Chem. Phys. Lett.*, 1993, **216**, 126–72.

[206] X. Li, L. W. Chung and K. Morokuma, *J. Chem. Theory Comput.*, 2011, **7**, 2694–8.

[207] S. Sekharan, O. Weingart and V. Buss, *Biophys. J.*, 2006, **91**, L07–9.

[208] P. Hamm, M. Zurek, T. Röschinger, H. Patzelt, D. Oesterhelt and W. Zinth, *Chem. Phys. Lett.*, 1997, **268**, 180–6.

[209] J. P. Kraack, T. Buckup and M. Motzkus, *Phys. Chem. Chem. Phys.*, 2011, **13**, 21402–10.

[210] S. O. Smith, A. B. Myers, R. A. Mathies, J. A. Pardoen, C. Winkel, E. M. van den Berg and J. Lugtenburg, *Biophys. J.*, 1985, **47**, 653–64.

[211] T. Polívka, S. Kaligotla, P. Chábera and H. A. Frank, *Phys. Chem. Chem. Phys.*, 2011, **13**, 10787–96.

[212] T. Buckup and M. Motzkus, *Annu. Rev. Phys. Chem.*, 2014, **65**, 39–57.

[213] G. Bassolino, T. Sovdat, A. S. Duarte, J. M. Lim, C. Schnedermann, M. Liebel, B. Odell, T. D. W. Claridge, S. P. Fletcher and P. Kukura, *J. Am. Chem. Soc.*, 2015, **-**, 150916112330003.

[214] B. P. Fingerhut, K. E. Dorfman and S. Mukamel, *J. Phys. Chem. Lett.*, 2013, **4**, 1933–42.

[215] B. P. Fingerhut, K. E. Dorfman and S. Mukamel, *J. Chem. Theory Comput.*, 2014, **10**, 1172–88.

[216] C. H. Camp Jr and M. T. Cicerone, *Nat. Photonics*, 2015, **9**, 295–305.

[217] C. H. Camp Jr, Y. Lee, J. M. Heddleston, C. M. Hartshorn, A. R. H. Walker, J. N. Rich, J. D. Lathia and M. T. Cicerone, *Nat. Photonics*, 2014, **8**, 627–34.